University of Alberta

Fabrication and Characterization of Ultra-flat Thin-film Material Surfaces for Nanoscale Research and Device Applications

by

Jason John Blackstock ©

A thesis submitted to the Faculty of Graduate Studies and Research in partial fulfilment
of the requirements for the degree of
Doctor of Philosophy

Department of Physics

Edmonton, Alberta
Fall 2005

Library and
Archives Canada

Published Heritage
Branch

395 Wellington Street
Ottawa ON K1A 0N4
Canada

Bibliothèque et
Archives Canada

Direction du
Patrimoine de l'édition

395, rue Wellington
Ottawa ON K1A 0N4
Canada

0-494-08615-7

Your file Votre référence
ISBN:
Our file Notre reterence
ISBN:

NOTICE:
The author has granted a non-exclusive license allowing Library and Archives Canada to reproduce, publish, archive, preserve, conserve, communicate to the public by telecommunication or on the Internet, loan, distribute and sell theses worldwide, for commercial or non-commercial purposes, in microform, paper, electronic and/or any other formats.

The author retains copyright ownership and moral rights in this thesis. Neither the thesis nor substantial extracts from it may be printed or otherwise reproduced without the author's permission.

AVIS:
L'auteur a accordé une licence non exclusive permettant à la Bibliothèque et Archives Canada de reproduire, publier, archiver, sauvegarder, conserver, transmettre au public par télécommunication ou par l'Internet, prêter, distribuer et vendre des thèses partout dans le monde, à des fins commerciales ou autres, sur support microforme, papier, électronique et/ou autres formats.

L'auteur conserve la propriété du droit d'auteur et des droits moraux qui protège cette thèse. Ni la thèse ni des extraits substantiels de celle-ci ne doivent être imprimés ou autrement reproduits sans son autorisation.

In compliance with the Canadian Privacy Act some supporting forms may have been removed from this thesis.

While these forms may be included in the document page count, their removal does not represent any loss of content from the thesis.

Conformément à la loi canadienne sur la protection de la vie privée, quelques formulaires secondaires ont été enlevés de cette thèse.

Bien que ces formulaires aient inclus dans la pagination, il n'y aura aucun contenu manquant.

Canada

"Man's mind, once stretched by a new idea, never regains its original dimensions."

-- Oliver Wendell Holmes

This thesis is dedicated to:

Robert (Bob) Wesley Blackstock, my late uncle.

A cast-iron teddy-bear, whose life was an example of the
virtues of dedication and perseverance in everything he pursued…
and most of all, in the way he looked after the people he loved.

And

John William Blackstock, my father.

My mentor, my compass and my best friend, from whom I have
learned the secret to a full and happy life:

Try many new things, to find those you like.
Repeat those you like, to determine what you love.
Practise what you love, to discover your life's passions.
Pursue your life's passions, each and everyday…
and always keep trying many new things.

Thesis Abstract

To fully enable the generation of device applications from nanoscience research, a range of thin-film material surfaces, well-characterized and uniform at the nanoscale, must be made available. This thesis focuses on developing fabrication techniques for producing a range of ultra-flat metal, metal-oxide and organic thin-film material surfaces, and on characterizing select thin-film surfaces of particular promise for nanoscale research and device applications. In specific, ultra-flat platinum, platinum-oxide and organic thin-film surfaces are fabricated and characterized using a variety of experimental techniques. Analysis of the results provides detailed scientific understandings of the formation and nanoscale properties of these thin-film surfaces.

The ultra-flat template-stripped (TS) Pt surfaces are produced and characterized using expanded template-stripping procedures, and *in-situ* ultrahigh-vacuum (UHV) template-stripping techniques are developed to allow the first detailed UHV scanning-tunnelling-microscopy (STM) atomic-scale characterization of a TS surface (specifically TS-Pt). The UHV-STM data demonstrate that, under appropriate production conditions, the average structure of a TS Pt surface is well-defined at the atomic scale — similar, in fact, to single-crystal Pt surfaces, though significantly less costly and time-consuming to produce. Advanced template-stripping procedures, incorporating a molecular releasing-layer on the templating-surface, are also developed (later in the thesis) and used to demonstrate micro-patterned ultra-flat Pt structures which are co-planar with an insulating matrix.

Modification of the ultra-flat Pt surfaces via the self-assembly thin-film organic monolayers (alkanethiols) and oxygen-plasma treatment is also explored. Examination of the organic self-assembled monolayers (SAMs) on ultra-flat metal (particularly Pt) thin-film substrates demonstrates that substrate smoothness is an important factor governing the uniformity of the SAM surfaces. The experimental data presented elucidate the nanoscale chemical properties and physical structure of the self-assembled organic thin-film surfaces, and further reveal important differences between the monolayers on different metal surfaces.

Detailed characterization of the oxygen-plasma treated Pt surfaces elucidates the nanoscale physical, chemical and electrical properties of the Pt-oxide ultra-thin-film formed on the Pt thin-film surface by the plasma treatment. The data also reveal that the oxygen-plasma results in a rapid initial formation of the Pt-oxide ultra-thin-film, followed by a steady-state regime of concurrent Pt-oxide etching and re-formation.

Lastly, a novel method for directly fabricating ultra-flat, high-purity carbon thin-film surfaces is demonstrated using direct carbon evaporation onto ultra-flat silicon substrates. Experimental characterization elucidates the nanoscale physical structure and chemical properties of the organic thin-film surfaces, and nano-patterning of the thin-film surfaces is also presented.

In the thesis conclusions, a variety of nanoscale research and device applications for the studied thin-film surfaces are considered. Both presently ongoing and potential future applications are discussed, along with avenues for further research into ultra-flat thin-film fabrication characterization.

Acknowledgements

For their endless patience, encouragement and support throughout my entire educational career — and even before — there are no words to express my gratitude, or my love, for my family.

I am deeply appreciative to my PhD supervisors, Mark R. Freeman and Jack A. Tuszynski, and my supervisor at HP, Duncan R. Stewart, for the time and energy they have invested in helping me mature, both as a scientist and as a person. I would also like to thank John-Bruce D. Green for his guidance and contributions towards my supervision, particularly in the field of chemistry. In addition, particular thanks go to Mark Roseman for providing his ear, his encouragement and his experience during the first half of my PhD. The contributions of three summer/co-op students who worked under my supervision on the research in this thesis — Daniel Salamon, Timmy Le and Michael Cook — are also gratefully acknowledged.

At the UofA Department of Physics, numerous behind-the-scenes staff were essential to the success of this work. Enormous thanks are extended to Gilbert Lachat and the rest of the Physics Machine Shop staff for their time, skill and ingenuity. Their work provided many of the nuts and bolts of several experimental apparatuses employed in the research herein… and the sharing of nostalgic stories from far away travels also broke the monotony of many days (and occasionally weeks) without successful experiments. Thanks also go to the technicians Greg Popowich and Don Mullin for their constant maintenance of and assistance with the evaporation systems in Physics. The rest of the support staff in Physics — from Yolande Peske in the storeroom to the always friendly staff in the general office (and many others) — are thanked for all the unnoticed work that keeps the department running.

In the UofA Department of Chemistry, thanks go to Joel A. Haber and Mark T. McDermott, along with their students, Nathan J. Gerein and Solomon Ssenyange, for sharing their expertise and collaborating on several projects. Thanks are also extended to the Green Research Group for continuously allowing access to lab space, equipment and resources.

Further afield within the UofA, considerable work for this thesis was conducted in the UofA Nanofab, and thanks go to all the staff of the Nanofab (particularly Stephanie Bozic and Keith Franklin) for their guidance and assistance throughout. The SEM images for this research were acquired at the Earth and Atmospheric Science SEM user facility, primarily by Dong-Chan Lee and George Braybrook. The XPS and TOF-SIMS data presented in this research was acquired at *Alberta Center for Surface Engineering and Science* (ACSES) run by Dimitre Karpuzov. Particular thanks go to both Dong-Chan and Dimitre for the many hours and late nights spent collecting data.

The entire team of researchers in the QSR division of HP labs, under the leadership of R. Stanley Williams, deserve incredible thanks for their numerous conversations, collaborations and contributions to the work in this thesis. Particular thanks go to Duncan R. Stewart, Zhiyong Li, Gun-young Jung, Doug Ohlberg, Regina Ragan, Sehun Kim, Brian Larade, Pam Long, Margie Flores and the entire staff of the HP Labs Model Shop headed by Gil Perusa. For their gracious hosting, collaboration and training with cAFM techniques, thanks are also extended to C. Daniel Frisbee and his students, Jeremy Beebe and Vince Engelkes, at the University of Minnesota.

Finally, I would like to thank the CIAR Nanoelectronics Program — participation in this program within weeks of starting my PhD provided the inspiration behind this doctoral research. Special thanks go to Martin Moskovits, the former Nanoelectronics Program Director, and Chaviva Hosek, the CIAR President, for extending to me many exceptional opportunities to participate in CIAR.

Financial support of this PhD through NSERC and iCORE scholarships is gratefully acknowledged.

Table of Contents

Chapter 1: Introduction **1**
- 1.0 Research Motivation and Objectives 1
- 1.2 Thesis Structure 4
- 1.3 Thesis Content and Scientific Contributions 5
- 1.4 Related Publications 13
- References 19

Chapter 2: Template-stripped Ultra-flat Metal Surfaces **22**
- 2.0 Introduction 22
- 2.1 Template-stripping Techniques 26
  - 2.1.1 Template-stripping from Ultra-flat Silicon Wafers 26
  - 2.1.2 Template-stripping using Cold-welding 27
  - 2.1.3 Template-stripping in Ultra-high Vacuum 32
- 2.2 Experimental Characterization of Template-stripped Metal Surfaces .. 36
  - 2.2.1 Characterization of TS Pt and TS Au 36
  - 2.2.2 UHV-STM of TS Pt 48
- References 60

Chapter 3: Alkanethiol SAMs on Ultra-flat Metal Surfaces **62**
- 3.0 Introduction 62
- 3.1 Experimental Characterization of SAMs 64
  - 3.1.1 Ellipsometry 65
  - 3.1.2 RAIRS 67
  - 3.1.3 Contact Angle Measurements 78
- 3.2 Discussion 82
- References 93

Chapter 4: Plasma Produced Ultra-thin Pt-oxide Surfaces **96**
- 4.0 Introduction 96
- 4.1 Physical Characterization 99
  - 4.1.1 Ultra-thin Pt Wire Electrical Resistance Measurements 99
  - 4.1.2 X-ray Photoelectron Spectroscopy 107
  - 4.1.3 Argon Plasma Treatment 116
  - 4.1.4 Oxide Formation Kinetics 117
- 4.2 Electrical Characterization 119
- References 129

Chapter 5: Template-stripping from Releasing-layers 132
5.0 Introduction 132
5.1 Fluoroalkylsilane SAMs on Silicon-oxide 134
5.1.1 Self-assembly of Fluoroalkylsilane Releasing-layers 134
5.1.2 Template-stripping Aluminium from Releasing-Layers 143
5.2 Template-stripping Pt and Au from Releasing-layers 145
5.3 Patterned Template-Stripping 151
References 161

Chapter 6: Ultra-flat Carbon Surfaces 162
6.0 Introduction 162
6.1 Fabrication of Ultra-flat Carbon Films on Si 164
6.2 Properties of Ultra-flat Carbon Surfaces 167
6.2.1 Physical Characterization 167
6.2.2 Electrochemical Characterization 171
6.2.3 Discussion 174
6.3 Nanoscale Patterning of ECFs 176
References 179

Chapter 7: Conclusions 181
7.0 Future Research and Applications 181
References 187

List of Tables

Chapter 2

Table 2-1 Refractive Indices for Pt Surfaces 42

Chapter 3

Table 3-1 Roughness of Metal Surfaces 64
Table 3-2 Thickness per Methylene Group for Alkanethiol Monolayers...... 66
Table 3-3 Alkanethiol Tilt Angles on Pt and Au 70
Table 3-4 RAIRS Peak Widths for Alkanethiol Monolayers on Pt and Au .. 72
Table 3-5 Contact Angles on Alkanethiol Monolayers on Au....................... 80
Table 3-6 Contact Angle Hysteresis for Alkanethiol Monolayers on Au...... 80
Table 3-7 Metal Properties and Alkanethiol Overlayer Packing Structures.. 87
Table 3-8 Area versus Title Angle for Alkanethiol Molecules...................... 87

Chapter 4

Table 4-1 Thickness of Ultra-thin Pt Wires..100
Table 4-2 Density and Swelling Ration of Pt Oxides......................................105
Table 4-3 Pt Oxide Thicknesses from XPS Measurements..........................109
Table 4-4 Pt Oxide Thicknesses from XPS Measurements..........................110
Table 4-5 Pt Oxide Chemical Species Assignments from XPS...................113

Chapter 5

Table 5-1 WCA for Fluorinated SAMs 136
Table 5-2 WCA and Ellipsometry Thickness for Fluorinated SAMs 138
Table 5-3 AFM Measured Roughness of Fluorinated SAMs 141
Table 5-4 WCA after Template-Stripping from Releasing Layers 146

Chapter 6

Table 6-1 Electrochemical Results from E-beam Carbon Films 173
Table 6-2 Comparison of Electrochemical Results for Carbon Electrodes..174

List of Figures

Chapter 2

Figure 2-1 Schematic of the Cold-Welded Template-Stripping Procedure... 28
Figure 2-2 Contact Angle Data and Optical Micrographs of CW-TS Pt....... 30
Figure 2-3 Schematic of the UHV Template-Stripping Procedure................ 33
Figure 2-4 Photographs of the UHV Template-Stripping Procedure............ 34
Figure 2-5 AFM and STM Images of TS Pt and Au.. 37
Figure 2-6 Roughness of TS Pt and Au Surfaces.. 38
Figure 2-7 AFM Images of 'aged' TS Pt and Au.. 40
Figure 2-8 Contact Angle of Pt Surfaces... 44
Figure 2-9 AR-XPS of TS Pt.. 45
Figure 2-10 XRD of TS Pt.. 47
Figure 2-11 $(500nm)^2$ UHV-STM Images of TS Pt.................................. 50
Figure 2-12 $(100nm)^2$ UHV-STM Images of TS Pt.................................. 51
Figure 2-13 $(1\mu m)^2$ UHV-STM Images of SC and TS Pt........................ 54
Figure 2-14 $(50nm)^2$ UHV-STM Images of SC and TS Pt........................ 55
Figure 2-15 $(100nm)^2$ UHV-STM Image of TS Pt...................................... 57
Figure 2-16 $(3nm)^2$ UHV-STM Images of SC and TS Pt............................ 58

Chapter 3

Figure 3-1 Ellipsometric Thickness of Alkanethiol SAMs............................ 66
Figure 3-2 RAIR Spectra of Alkanethiol SAMs on Pt and Au...................... 68
Figure 3-3 Single Chain Model of Alkanethiol SAMs.................................. 70
Figure 3-4 RAIR Spectra of Alkanethiol SAMs on Pt.................................. 73
Figure 3-5 RAIR Spectra of Alkanethiol SAMs on Au................................ 73
Figure 3-6 RAIRS Peak Ratio for Alkanethiol SAMs on Pt and Au............ 74
Figure 3-7 RAIRS Peak Position for Alkanethiol SAMs on Pt and Au........ 76
Figure 3-8 Water Contact Angles for Alkanethiol SAMs on Pt 79
Figure 3-9 Schematic Models of Alkanethiol SAMs on Pt........................... 83
Figure 3-10 RAIR Spectra of Alkanethiol SAMs on Pt and Ag..................... 85

Chapter 4

Figure 4-1 Schematic Illustration of Angle Evaporation Technique............100
Figure 4-2 Pt Resistivity versus Thickness for Ultra-thin Pt Wires.............103
Figure 4-3 Pt Ultra-thin Wire resistance versus Oxygen Plasma Time........104
Figure 4-4 Model of Pt to Pt-Oxide Conversion..105
Figure 4-5 X-ray Photoelectron Spectra of Pt-Oxide..................................108
Figure 4-6 Quantitative Fitting to XPS Spectra of Pt-Oxide........................109
Figure 4-7 XP Spectra versus Plasma time for Pt-Oxide Samples...............111
Figure 4-8 XPS Attenuation with Electron Take-off Angle for Pt-Oxide....112
Figure 4-9 Model of Ultra-thin Pt-Oxide Stratified Structure......................116
Figure 4-10 cAFM *I-V* Data from Metallic Pt..120
Figure 4-11 cAFM *I-V* Data from Pt-Oxide...121
Figure 4-12 cAFM *I-V* Data from Pt-Oxide showing Oxide Breakdown......122
Figure 4-13 STM Images of Pt-Oxide...125
Figure 4-14 Successive STM Images showing Pt-Oxide Breakdown............127

Chapter 5

Figure 5-1 Fluorinated Alkane Chains 135
Figure 5-2 Gas-Phase Self-Assembly Chamber for Chlorosilanes 139
Figure 5-3 AFM Images of Fluorinated SAMs 141
Figure 5-4 X-ray Photoelectron Spectrum of a Fluorinated SAM 147
Figure 5-5 X-ray Photoelectron Spectra of Fluorinated SAMs 148
Figure 5-6 X-ray Photoelectron Spectra of Fluorinated SAMs 150
Figure 5-7 Optical Micrographs of Patterned Template-Stripped Features..153
Figure 5-8 AFM Topography Images of pTS Features 154
Figure 5-9 TOF-SIMS Images of Patterned Template-Stripped Features....155
Figure 5-10 AFM Topography Images of pTS Features 158
Figure 5-11 AFM Images of Patterned pTS Features 160

Chapter 6

Figure 6-1 Surface Roughness of E-beam Carbon Films 168
Figure 6-2 AFM Images of E-beam Carbon Films 169
Figure 6-3 Raman Spectra from E-beam Carbon Films 171
Figure 6-4 SEM of E-beam Carbon Nanowires 178

Notation, Acronyms and Abbreviations

Acronyms

AFM	atomic force microscopy
AR-XPS	angle-resolved x-ray photoelectron spectroscopy
cAFM	conductive atomic force microscopy
CW-TS	cold-welded template-stripped
e-beam	electron-beam
EBL	electron-beam lithography
FTIR	Fourier transform infrared spectroscopy
HP	Hewlett-Packard
LB	Langmuir-Blodgett
LEED	low-energy electron diffraction
LN	liquid nitrogen
nTP	nanotransfer printing
pTS	patterned-template-stripped
PV roughness	peak-to-valley roughness
QSR	Quantum Science Research group (at HP Labs)
RAIRS	reflection-adsorption infrared specfroscopy
RL	releasing layer
RMS roughness	root-mean-square
SAMs	self-assembled monolayers
STM	scanning tunnelling microscopy
TS	template-stripped
TOF-SIMS	time-of-flight scattered-ion-mass-spectroscopy
UHV	ultrahigh vacuum
UV	ultraviolet
v/v	volume-to-volume ratio
WCA	water contact angle
XRD	x-ray diffraction

Chemical Abbreviations

Al	Aluminium	F	Fluorine	Pd	Palladium
Ag	Silver	H	Hydrogen	Pt	Platinum
Au	Gold	Hg	Mercury	S	Sulphur
Cl	Chlorine	Na	Sodium	Si	Silicon
Cu	Copper	O	Oxygen	Ti	Titanium
Cr	Chrome	P	Phosphorous		

C#SH (ie. C6SH, C8SH, *et cetera*…)	$CH_3(CH_2)_{n-1}SH$
C# (ie. C6, C8, C10, *et cetera*…)	$CH_3(CH_2)_{n-1}SH$
F17-T	$CF_3(CF_2)_7(CH_2)_2SiCl_3$
F17	$CF_3(CF_2)_7(CH_2)_2Si(CH_2)_2Cl$
F7	$CF_3(CF_2)_2(CH_2)_2Si(CH_2)_2Cl$

Chapter 1: Introduction

1.0 Research Motivation and Objectives

As nanoscience research begins to generate a wide range of device applications — including chemical and biological sensors, and nanoscale electronic devices — the production of thin-film material surfaces with well-characterized nano- and atomic-scale properties is of mounting scientific and technological interest. This interest stems from the fact that the behaviours of nearly all such devices are governed by atomic and molecular scale interactions at the heterointerfaces created when thin layers of material are grown or deposited on select surfaces. As a result, the level to which the fundamental nature of such interactions can be understood by a scientist — and therefore utilized to design technologically useful devices — is directly reliant upon how well the scientist understands the structure of the surfaces at length scales at which the interactions occur.

What has made the understanding of surfaces possible at the nano- and atomic-scales — and thereby enabled nanoscience research in general — is the broad assortment of experimental techniques for characterizing the chemical and physical properties of materials that were developed throughout the 20th century.[1] Techniques based on bombarding samples with various forms of radiation (electromagnetic or particulate) and measuring the resultant scattered or generated radiation from the samples date back to the early parts of the 1900s, and have been continually expanding in diversity and utility since. Such spectroscopic and diffraction methods were the first detailed techniques employed for respectively studying the composition and reciprocal-space structure of surfaces over a wide range of length scales. The advent of scanning probe microscopies and spectroscopies in the 1980s further accelerated the expansion of surface science research, allowing detailed quantitative information to be obtained on the real-space structure and composition of material surfaces at length scales down to and even below the dimensions of single atoms.

The majority of the surface science research conducted to date has focused on the surfaces of bulk single-crystal substrates, owing to their uniformity and simplicity relative to the generally more complex surfaces of polycrystalline and thin-film materials. The surfaces a range of bulk single-crystal materials — including metals, semi-conductors and even organic bulk single-crystal materials — have been examined over the past decades, and much is understood regarding their structure and properties. For example, the surfaces of bulk single-crystal silicon — the workhorse material of the electronics industry for the past 50 years — are likely the most studied material surfaces, owing to their critical role in the growth of high quality interfaces inside common electronic devices.

The understanding of various bulk single-crystal surfaces has, in fact, resulted in these surfaces becoming popular for fundamental nanoscience research applications. Returning to silicon as an example, the detailed atomic-scale knowledge of the physical and chemical surface properties of bulk single-crystal silicon surfaces has enabled the understanding and development of processes for controllably self-assembling molecular scale nanowires and other nanostructures on silicon surfaces, out of materials ranging from other semiconductors,[2-5] to metals,[6-8] to even organic molecules.[9-11] (The references provided here are only select examples taken from the vast array of scientific literature on similar topics.) This knowledge has even paved the way for studying the breakdown reaction dynamics of individual molecules on silicon surfaces;[12, 13] these particular investigations have provided some of the most detailed information on single molecule reactions to date.

Despite the advantages of using well-understood bulk single-crystal surfaces for such fundamental nanoscience research, however, bulk single-crystal substrates are not generally suitable for most nanoscience device applications. Beyond the prohibitively high costs associated with single-crystal substrates and fabrication procedures (generally involving working in ultra-high vacuum {UHV} environments), the incorporation and patterning of bulk single-crystal materials into nanoscale device geometries is extremely difficult.

Conventional device fabrication is rather carried out using thin-film materials, which can be integrated and patterned at the nanoscale with relative ease, and whose preparation is cost-effective. The challenge that arises with the use of thin-films for nanoscale research and device applications lies, in general, with the greater complexity of the thin-film surfaces relative to bulk single-crystal surfaces. Typical thin-film deposition procedures produce polycrystalline thin-film surfaces, which normally demonstrate significant topographic roughness on the nanoscale and highly variable atomic-scale texture. For devices where the relevant interactions occur at the atomic and molecular scale, the non-uniform surface structure of conventional thin-film material surfaces can create significant issues for both understanding device behaviour and establishing device reproducibility.

To fully realize the potential of nanoscience research to generate device applications — and thus enable the commercial potential of nano*technology* — simple and cost-effective techniques need to be developed for generating uniform and well-characterized thin-film material surfaces. The research presented in this thesis therefore centres around the fabrication and detailed characterization of novel ultra-flat thin-film material surfaces. The main objectives for the research herein were defined as follows:

1. To develop techniques for fabricating ultra-flat thin-film material surfaces of promise for nanoscale research and device applications.
2. To characterize the nanoscale physical and chemical properties of specifically selected thin-film surfaces, chosen because of both their potential utility and the lack of previous detailed examination.
3. To consider future applications in which the determined nanoscale properties of the studied thin-film surfaces could be advantageously employed.

In selecting the particular thin-film surfaces for fabrication and characterization, one attribute of the materials and fabrication processes was also considered: compatibility with conventional silicon electronics technology. For device applications where novel thin-film material surfaces could be most valuable — specifically, sensors and nanoscale electronics — the ability to integrate the thin-film surfaces with conventional silicon electronics dramatically enhances the surfaces' potential utility.

Based on the above objectives and this criterion, this thesis presents the fabrication and characterization of thin-film Pt, Pt-oxide and organic material surfaces that are ultra-flat on the nanoscale. As discussed throughout the thesis, each of these thin-film surfaces fabricated and studied present distinct nanoscale physical and chemical surface properties that are desirable for a variety of nanoscience research and device applications. Furthermore, this selection incorporates representative thin-film surfaces from several material classes — including metals, metal-oxides and organics — demonstrating the potential versatility of the fabrication processes.

1.1 Thesis Structure

This thesis is structured into five experimental chapters (Chapters 2 through 6). Each chapter examines a specific process for fabricating ultra-flat thin-film surfaces, and includes the detailed characterization of at least one surface of particular interest. The order in which the research is presented is determined by the fact that several of the fabrication procedures explored and developed in later chapters make use of techniques and/or results from earlier chapters.

The layout of each chapter generally follows the sequence of the objectives listed in the previous section. The start of every chapter provides general background on the ultra-flat thin-film surface fabrication technique and particular surfaces explored therein, along with the impetus underlying the selection of both for study. The surface production or modification processes are then presented, in conjunction with any experimental data relating to process development. The experimental characterization of the select thin-film surfaces follows next, along with the experimental characterization of other related surfaces incorporated for comparison where appropriate.

Finally, Chapter 7 concludes the thesis by considering avenues for further research, and applications for both the fabrication techniques and the ultra-flat thin-film surfaces examined throughout the thesis.

1.2 Thesis Content and Scientific Contributions

The first experimental chapter of this thesis (Chapter 2) focuses on the production of ultra-flat noble metal thin-film surfaces using a fabrication technique known as *template-stripping*.[14-16] In brief, a metal thin-film is first deposited by physical vapour deposition (PVD)[17] onto a templating-surface to which it does not strongly adhere. This is followed by the exposed face of the film being attached to a solid support, which is then used to lift-off or 'strip' the film from the template. This process is designed to result in the uncovered template-stripped (TS) thin-film metal surface having approximately the same physical topography of the original template.

Chapter 2 begins with a description of three template-stripping procedures, developed in this research in order to expand the utility of the template-stripping methodology. The first procedure presented is an adaptation of the original template-stripping process. The process employs commercially available, ultra-flat silicon wafers as the templating surfaces, in order to generate TS metal surfaces with similarly ultra-flat surfaces. The nanoscale smoothness of the produced TS surfaces has substantial advantages over metal films generated with conventional PVD procedures, which generally result in metal surfaces with significant topographic roughness on the nanoscale.

The second template-stripping procedure developed in Chapter 2 expands upon the first, employing a metal-metal cold-welding process[18-20] to attach the TS metal film to the solid support. Standard template-stripping procedures employ epoxies to attach the TS metal film to the solid support. Due to the incompatibility of the epoxies with many environments, however, the utility of the TS samples is limited. Replacing the epoxies with this cold-welding process creates TS samples which are compatible with any environment in which the metals themselves are stable. The third procedure developed provides for template-stripping of samples inside an ultra-high-vacuum (UHV) chamber. As exposure of clean metal surfaces to ambient laboratory conditions results in rapid contamination with adsorbates, this procedure enables the preparation of uncontaminated TS surfaces in a UHV environment for study with a variety of UHV-based surface science techniques. These later two template-stripping processes appreciably increase the range of environments in which TS samples can be used.

The later half of Chapter 2 focuses on characterizing the nanoscale physical and chemical properties of TS platinum surfaces produced using this range of template-stripping procedures. Platinum was selected as the material surface for detailed study, both because this research was the first demonstration of ultra-flat platinum via template-stripping, and because Pt has advantages over the other noble metal TS films previously examined. Most importantly, Pt is easily compatible with silicon semiconductor technologies, whereas other more commonly studied noble metals (such as Au) are not. In addition, the modification of Pt surfaces using the fabrication techniques explored in Chapters 3 and 4 has not been previously explored in depth, even though the new material surfaces generated demonstrate considerable potential for utility. Therefore, a detailed understanding of TS Pt surfaces provides a strong foundation for these later studies. TS Au surfaces are also fabricated with the same processes and characterized along side the TS Pt for comparison.

The characterization of the TS Pt and TS Au surfaces in Chapter 2 incorporates a variety of techniques, including: water contact angle measurements; X-ray photoelectron spectroscopy (XPS); X-ray diffraction (XRD); atomic force microscopy (AFM); and scanning tunnelling microscopy (STM). The cumulative data from these techniques provide the most comprehensive study of noble metal TS surfaces to date. Significant contributions from this work to the scientific understanding of the nanoscale structure and formation of noble metal TS surfaces include:

- The AFM and ambient condition STM data acquired on the TS Pt and Au surfaces demonstrate that the intrinsic hardness of the deposited metal governs the capacity of the TS metal surface to replicate the ultra-flatness of the templating surface; the hardness of Pt is revealed to be advantageous for achieving the smoothest surface at the nanoscale, as well as for resistance to physical aging after stripping.

- The XPS, water contact angle data and UHV-STM concurrently show that the TS metal surfaces are free from observable surface contamination by either adsorbates or remnant templating surface material immediately after stripping.[21]
- UHV-STM (supported by XRD) conclusively demonstrates — for the first time to the best knowledge of the author — the expected <111> crystalline texture of an ultra-flat noble metal TS surface (specifically TS Pt).
- The influence of a primary fabrication parameter — the pre-stripping annealing of a TS film while still in contact with the template — on the nanoscale structure of the TS Pt surface is also elucidated using UHV-STM. The data provide an understanding of both how the nanoscale physical structure of the TS Pt evolves during the annealing process, and reveals limits at which the TS surface evolution leads to undesirable surface features.

The research presented in Chapter 3 uses the foundation established by Chapter 2 to investigate a second material surface fabrication technique: the modification of noble metal surfaces using self-assembled monolayers (SAMs) to generate new material surface properties. The modification of a variety of surfaces with monolayers of organic molecules that chemically self-assemble onto the given surface, has been explored for two decades as a method of engineering the macroscopic and nanoscale properties of surfaces (for reviews, see refs.[22-26]). However, despite the anthology of previous research literature, many important questions still remain regarding the influence of basic variables — for instance, the nanoscale topography of the substrate surface — on the structure of SAMs and their resultant surface properties. Furthermore, the parameter space of monolayer-substrate combinations of potential interest has only been fractionally explored.

Chapter 3 focuses specifically on the formation and characterization of alkanethiol SAMs, both on the ultra-flat TS noble metal surfaces examined in Chapter 2, and on rougher surfaces of the same noble metals produced using conventional PVD processes. Alkanethiol SAMs were selected for examination because of the considerable volume of previous research conducted on them,[22-24, 26] which facilitates the interpretation of experimental data. A variety of experimental techniques were employed in the investigation of the SAMs, including: ellipsometry; X-ray photoelectron spectroscopy (XPS); receding and advancing water contact angle measurements; and reflection-adsorption infrared spectroscopy (RAIRS).

Besides investigating the outstanding issue of the influence of nanoscale surface roughness on the SAM structure (which is ideally enabled by the TS surfaces from Chapter 2), Chapter 3 also includes the detailed investigation of alkanethiol SAMs on Pt. Despite the advantages of dealing with Pt relative to more commonly employed noble metal surfaces — particularly for applications of SAMs in integrated nanoscale (molecular) electronics or sensors[27-36] — previous studies[37-41] of SAMs on metallic Pt have been very limited. The research in Chapter 3 includes the following major contributions to the scientific understanding of self-assembled monolayers:

- A detailed description of the monolayer packing structure on Pt is generated, showing an alkane chain orientation tilted on average at ~12° to 15° from the Pt surface normal, and a $\sqrt{3} \times \sqrt{3}$ overlayer relation of the alkanethiol molecules to the Pt atoms of the underlying <111> oriented ultra-flat surfaces.
- Comparison of SAMs on the ultra-flat and rough surfaces reveals a significant dependence of monolayer packing structure on the roughness of Pt surfaces. A much less substantial dependence in the case of SAMs on Au is observed, and the difference on the two surfaces is correlated to the intrinsic hardness of the metals.

- Further investigation of differences between SAMs on ultra-flat and rough Au surfaces demonstrates that the use of ultra-flat Au surfaces do produce more homogeneous SAM surfaces.

The research in Chapter 3 also represents one significant nanoscience application of the TS surfaces developed and characterized in Chapter 2.

Similar to the previous chapter, Chapter 4 considers another material surface modification technique that can build on the template-stripping work of Chapter 2. The exposure of metal surfaces to plasma treatments has found application in microelectronics device fabrication as a convenient technique for cleaning away thin layers of adsorbed organic contaminants (for example, resist residues after patterning).[42-45] To date, however, the understanding of the interaction of the plasma irradiation with different metal surfaces has been limited, particularly for chemically reactive plasmas such as oxygen (O_2) plasma. Continuing with the focus on platinum, Chapter 4 examines the O_2 plasma treatment of Pt surfaces. This combination — Pt with O_2 plasma — is of particular experimental interest because two previous literature studies[38, 46] have reported that, in addition to removing organic contaminants, the O_2 plasma also generates a nanoscale layer of platinum-oxide on a metallic Pt surface. Platinum-oxide is an attractive material because of its potential utility as a semi-conductor and/or insulator in nanoelectronic devices, along with its potential value in sensors and as catalysts.[47-52] The conventional method of producing platinum-oxide by reactive sputtering, however, has been thus far unsuccessful at producing platinum-oxide thin-films on metallic substrates (such as metallic Pt or Au);[51] especially for electronics applications, this is a significant shortcoming.

Chapter 4 comprises a detailed experimental investigation of O_2 plasma produced platinum-oxide and the plasma induced platinum-oxide formation process. The characterization techniques employed for this empirical study include: angle-resolved X-ray photoelectron spectroscopy (AR-XPS); ultra-thin film resistivity measurements; conductive atomic force microscopy (cAFM); and scanning tunnelling microscopy (STM). Interpreting the data from this compilation of techniques provides several important contributions to the scientific understanding of the plasma-produced platinum-oxide material surface properties and formation:

- AR-XPS reveals that the platinum-oxide ultra-thin film is composed of two platinum-oxygen compounds, arranged in a vertically stratified structure, with the oxide 'bulk' (just above the underlying metallic Pt substrate) being primarily of PtO_2 — likely with PtO defects — and the exposed oxide surface being $Pt(OH)_{y\approx 2}$ terminated after exposure to ambient conditions.
- AR-XPS and ultra-thin film resistivity measurements combined, demonstrate that the O_2 plasma treatment rapidly ($t \ll 1$min) generates the platinum-oxide ultra-thin film (~2.5nm), and subsequently etches the film at a constant rate (~1.7Å/sec), while continually forming new oxide to maintain a constant ultra-thin film thickness.
- cAFM data from plasma-produced platinum-oxide on TS Pt surfaces reveals the oxide to have semi-conducting properties with a bandgap of approximately ~1.2V, while STM data show inhomogeneities in the lateral nanoscale electrical characteristics of the oxide film. Both techniques confirm the limited stability of the platinum-oxide, revealing electrical decomposition/breakdown of oxide film under a range of bias conditions.

Chapter 5 returns to consider further advancements of the template-stripping technique itself. The chapter focuses on developing a method for expanding the range of surfaces generated by template-stripping alone, by engineering the surface properties of the *templating* surfaces to be inert to more reactive PVD materials. Motivated by the demonstration in Chapter 3 of SAMs on ultra-flat surfaces producing highly uniform surface properties, Chapter 5 explores the use of SAMs on ultra-flat silicon-oxide templating surfaces as a means for further reducing the adhesion of deposited materials to the templating surface. Based on the very low reactivity of the fluorinated-carbon, it was hypothesized that a self-assembled monolayer of fluoroalkylsilane molecules on ultra-flat silicon-oxide could produce an ultra-flat surface with lower adhesion to a wider range of materials.

The first half of Chapter 5 explores the self-assembly of different length mono- and tri-chlorosilane fluoroalkylsilane molecules on the ultra-flat silicon-oxide surfaces, which are characterized using ellipsometry, water contact angle and AFM. The hypothesis of lower adhesion is tested by depositing a thin film of aluminium — which adheres strongly to clean silicon-oxide due to its reactivity — onto the best quality SAMs and testing the adhesion of the film to the surface. The vapour phase deposition of tricholorosilane molecules in vacuum onto ultra-flat silicon-oxide is demonstrated to result in very low adhesion of the aluminium film, allowing the template-stripping aluminium. These results represent the first demonstration of the use of a *releasing-layer* to engineer surfaces for template-stripping, as well as the first demonstration of the template-stripping of aluminium films.

To facilitate comparisons to the data from Chapter 2, an examination of Pt and Au surfaces template-stripped from releasing-layer coated silicon-oxide surfaces are examined. However, combined water contact angle and XPS demonstrate that Pt deposited onto the releasing layer at room-temperature completely destroys the releasing layer; conversely, the room temperature deposition of Au is shown to only disturb, but not destroy, the releasing-layer. Further examination, combined with insight from literature, reveals that during the deposition of the platinum, the Pt atoms are likely catalyzing the breakdown of the releasing layer molecules. This result establishes an important limitation of the developed releasing-layer template-stripping process.

The final portion of Chapter 5 develops a technique for employing the releasing-layer concept to generate micron-scale patterned features of TS Pt surrounded by an insulating material matrix. The generated patterned template-stripped (pTS) Pt — the first demonstrated to date — are characterized by AFM and revealed to be correspond well to the large-area TS Pt surfaces studied in Chapter 2. For device applications, the patterned TS features have greater potential for utility that the large-area TS surfaces demonstrated previously.

The last experimental chapter of this thesis, Chapter 6, returns to consider the formation of ultra-flat organic surfaces. The concept of exploring the formation of ultra-flat amorphous (or poly-graphitic) carbon via template-stripping from the silicon-oxide surfaces was initially considered. However, early experimentation revealed that the electron-beam (e-beam) evaporation of carbon onto ultra-flat silicon wafers with the native oxide removed, produced well-adhered carbon films that retained the ultra-flat properties of the underlying silicon; thus making the study of template-stripping evaporated carbon films redundant.

Chapter 6 presents the processes for fabricating large-area e-beam deposited carbon films on the bare silicon surfaces, along with characterization of the films using atomic force microscopy (AFM), Raman spectroscopy and film resistivity measurements. The electrochemical characterization of the films conducted by the McDermott Group (Chemistry Department, UofA) in a collaborative research effort is also succinctly incorporated. The data collected provides scientific understanding of several aspects of these novel ultra-flat organic substrates:

- AFM reveals that, after an initial film seeding stage, the nanoscale surface roughness of the freshly evaporated ECF surfaces increases gradually with carbon film thickness (while still remaining exceptionally smooth up to 200nm carbon thickness).
- Raman spectroscopy establishes that freshly deposited ECFs have an amorphous carbon structure.
- Post deposition pyrolysis of the ECFs at 1000°C is shown to result in the formation of graphitic structure inside the film, which is correlated with an increase in the nanoscale roughness of the surfaces.

The fabrication of nanoscale e-beam evaporated carbon features using conventional electron-beam lithography is demonstrated at the end of Chapter 6. Amorphous carbon features down to 50nm are demonstrated, showing the potential utility of the evaporated carbon process for nanoscale device applications.

This complete research presented in this thesis has contributed significant progress to our understanding of both the fabrication processes for generating novel ultra-flat thin-film surfaces and the nanoscale properties of select surfaces. Several of the specific contributions outlined above have been presented to the scientific community through a series of peer-reviewed publications, which are summarized in the following section. Through personal correspondence, the author has been made aware that several research groups are utilizing several techniques and results presented in these publications and in presentations at scientific conferences.

1.3 Related Publications

A significant portion of the research presented in this thesis has been presented in six scientific peer-review articles, which have been accepted for publication or published in scientific journals. Two manuscripts, presently in preparation for submission to peer-reviewed journals, cover another portion of the research herein. Much of the data, and some of the text, presented in the body of this thesis can be found in these publications. A brief synopsis of each publication and manuscript is provided below, in the order in which the research appears in this thesis. Along with each synopsis, the contributions of the author of this thesis to each publication is explicitly described.

* Denotes corresponding author(s).

- Template-Stripping Using Cold-Welding Jason J Blackstock*, Zhiyong Li and Gun-young Jung *Journal of Vacuum Science and Technology A: Vacuum, Surfaces and Films* 22, 602-605 (2004). The method for fabricating ultra-flat template-stripped (TS) metal surfaces on standard silicon/silicon-oxide wafers by means of gold cold-welding is presented (included in Chapter 2 of this thesis). Cold-welded template-stripped (CWTS) Pt surfaces are demonstrated as an example, and characterized using AFM. The cold-welding adhesion process is shown to decrease in effectiveness as function of time exposed to ambient laboratory conditions after removal from vacuum and prior to pressurized cold-welding. Contact angle measurements demonstrate this to be caused by the gradual increase in surface contamination of the evaporated gold layers prior to their being joined by cold-welding. The bulk of the experimental work and manuscript preparation for this publication was conducted by JJB. ZL and GJ aided in the conceptual development of the cold-welding template-stripping process; GL had previously built the hydrostatic pressure chamber utilized in the procedure.

- Ultra-flat Platinum Surfaces from Template-Stripping of Sputter Deposited Films Jason J Blackstock*, Zhiyong Li, Mark R Freeman and Duncan R Stewart *Surface Science*, **546**, 87-96 (2003). The study of the ultra-flat TS Pt is reported, along with comparisons to TS Au and regularly PVD prepared Pt and Au surfaces (included in Chapter 2 of this thesis). The observed optical constants, as well as X-ray crystallography data, demonstrate that macroscopic properties of the sputtered TS platinum films are similar to previously studied evaporated platinum films.[53] Scanning probe microscopy of the surfaces shows that TS Pt exhibits ~1Å RMS roughness over $1\mu m^2$, demonstrating higher fidelity to the templating ultra-flat silicon-oxide than TS gold. The TS platinum surface also shows high physical stability in ambient laboratory conditions over the period of a week, whereas considerable topographical aging is observed in the case of the TS gold surface. The bulk of the experimental work and manuscript writing for this peer-reviewed publication was conducted by JJB.
- Atomic Surface Structure of UHV Prepared Template-Stripped Platinum and Single Crystal Platinum(111) Regina Ragan*,[†], Doug Ohlberg[†], Jason J Blackstock*,[†], Sehun Kim and R Stanley Williams *Journal of Physical Chemistry B*, **108**, 20187-20192 (2004). ([†]These three authors contributed equally to this work.) The technique for template-stripping ultra-flat noble metal surfaces *in-situ* under ultrahigh vacuum is presented, along with UHV-STM characterization of TS Pt surfaces and single crystal Pt(111) surfaces (included in Chapter 2 of this thesis). The UHV-STM data clearly demonstrate that under the preparation conditions examined in the paper, TS Pt surfaces are predominantly <111> textured (while still polycrystalline), with a surface

roughness equivalent to or better than a single crystal Pt(111) surface. The contribution of JJB to this work included sample handling design with DO, all TS sample fabrication, STM data analysis and image processing with RR, and writing of the first draft of the manuscript along with subsequent editing. The UHV-STM imaging itself was conducted by RR, DO and SK.

- Optimization of in-vacuo template-stripped Pt surfaces via UHV STM Doug Ohlberg*, Jason J Blackstock*, Regina Ragan, Sehun Kim and R Stanley Williams *Applied Physics A*, accepted for publication in October, 2004. Several TS Pt surfaces, prepared using a range of post-deposition annealing times and template-stripping in UHV, are examined using UHV-STM (included in Chapter 2 of this thesis). The post-deposition annealing treatments are shown to result in the emergence and continuous growth of large smooth crystallites. Issues with crystallite orientation relative to the TS surface and artefacts arising as a result of the epoxy used in the template-stripping process are presented and discussed in relation to optimizing the template-stripping procedure. The contribution of JJB to this work included designing the experiment with DO, complete TS sample fabrication, STM data analysis and image processing with RR and DO, and significant contributions to the preparation of the manuscript. The UHV-STM imaging itself was conducted by RR, DO and SK.
- Alkanethiol Self-Assembled Monolayers on Ultra-flat Pt Jason J Blackstock*, Zhiyong Li, Duncan R Stewart, Kelvin Isaacson, Daniel Y Kwok, Mark R Freeman and John-Bruce D Green *Manuscript in preparation for submission to the Journal of the American Chemical Society.* The characterization of a series of n-alkanethiol SAMs formed on Pt surfaces is presented, prepared by both template-stripping and conventional sputtering (included in Chapter 3 of this thesis). Ellipsometry, water contact angle and RAIRS data are shown to demonstrate significant differences between the structures of the monolayers formed on the two Pt substrates. In particular, the roughness of the Pt surface is shown to be a major factor influencing monolayer structure, with SAMs on the ultra-flat template-stripped (TS) Pt

surfaces demonstrating more consistent methyl termination, molecular chain orientation and crystalline packing throughout the alkane length series. The characterization of n-alkanethiol SAMs on ultra-flat TS Au surfaces and conventionally sputtered Au and Ag films is included for comparison, and results on other metals from literature are considered. Comparison between different metal surfaces demonstrate notable differences, revealing the refractory nature of Pt has a significant influence on the formation and structure of the n-alkanethiol SAMs. Aside from the data presented for monolayers on conventionally sputter-deposited platinum surfaces — which was collected by ZL and presented in a previous publication[41] — all the experimental data collection and analysis, as well as the manuscript preparation, were conducted primarily by JJB.

- A Contact Angle Study of Alkanethiol Monolayers on Ultra-flat Au Substrates Kelvin Isaacson, Jason J Blackstock, Mark R Freeman and Daniel Y Kwok* *Manuscript in preparation for submission to Langmuir.* The contact angle characterization of octadecanethiol and dodecanethiol SAMs on Au substrates produced via template-stripping, conventional evaporation and flame-annealing of evaporated Au surfaces is reported (included in Chapter 3 of this thesis). The data presented reveal that SAMs on ultra-flat TS Au exhibit contact angles and contact angle hysteresis consistent with expectations for a tightly-packed methyl surface with few defects. Comparatively, similar SAMs on the other Au surfaces are shown to have less consistent contact angles and greater contact angle hysteresis, revealing a higher density of defects. The contact angle data for this publication were collected by KI; JJB contributed the characterization of the TS surfaces. The manuscript preparation was led by KI, with significant contributions from JJB.
- Plasma Produced Ultra-thin Platinum Oxide Films for Nanoelectronics: Physical Characterization Jason J Blackstock*, Duncan R Stewart and Zhiyong Li *Applied Physics A*, accepted for publication in October, 2004. The detailed experimental characterization of ultra-thin platinum oxide films formed on metallic Pt surfaces using O_2 plasma treatment is presented (included in

Chapter 4 of this thesis). A monotonic consumption of the metallic Pt by the O_2 plasma is demonstrated by electrical resistance measurements of micron-wide, ultra-thin metallic Pt wires for the range of O_2 plasma exposure times explored. Conversely, angle resolved X-ray photoelectron spectroscopy (AR-XPS) of the plasma-treated Pt reveals that the oxide layer formed on the Pt surface maintains a constant thickness over these exposure times. In combination, these data show that the O_2 plasma treatment of Pt simultaneously forms and etches an ultra-thin platinum oxide layer on the Pt surface. AR-XPS data reveal the oxide layer to be composed of two different platinum-oxygen compounds, which are segregated into a stratified structure with the oxide 'bulk' being composed of PtO_2 (likely with PtO defects) and the exposed oxide surface being $Pt(OH)_{y\approx 2}$ terminated after exposure to ambient conditions. The experimental work and manuscript preparation for this publication were all primarily conducted by JJB.

- Characterization of Ultra-Flat Carbon Film Electrodes Prepared by Electron-Beam Evaporation Jason J Blackstock, Abbas A. Rostami, Aletha M. Nowak, Richard L. McCreery, Mark R. Freeman and Mark T. McDermott* *Analytical Chemistry*, **76**, 2544-2552 (2004). The fabrication and characterization of the e-beam deposited carbon films (ECFs) are presented (included in Chapter 6 of this thesis). AFM is used to show that the freshly evaporated ECF surfaces maintain the ultra-flat properties of the underlying silicon wafer, while Raman spectroscopy establishes the amorphous structure of the carbon. Pyroloysis at 1000°C is shown to transform the carbon to a poly-crystalline structure, while also resulting in an increase in the nanoscale surface roughness. The electrochemical behaviour of the electrodes is studied and shown to resemble glassy carbon, with measured heterogeneous electron transfer rate constants among the highest measured for thin carbon films. For this publication, JJB developed the ultra-flat carbon film fabrication technique, conducted the physical characterization (with the exception of the Raman spectroscopy conducted by AMN & RLM at Ohio State) and prepared the original manuscript. The electrochemical characterization was conducted by AAR and MTM.

References

(1) For an extensive list of experimental material characterization techniques see: Section 12 (pages 12-1 to 12-6) of the 85th Edition of the CRC Handbook of Chemistry and Physics, Ed. David R. Lide, CRC Press LLC (2004).

(2) Kamins, T. I.; Williams, R. S.; Basile, D. P. *Nanotechnology* **1999**, *10*, 117-121.

(3) Henstrom, W. L.; Liu, C.-P.; Gibson, J. M.; Kamins, T. I.; Williams, R. S. *Applied Physics Letters* **2000**, *77*, 1623-1625.

(4) Kamins, T. I.; Nauka, K.; Williams, R. S. *Applied Physics A* **2001**, *73*, 1-9.

(5) Huang, C. J.; Yu, J. Z.; Wang, Q. M. *Progress in Natural Science* **2004**, *14*, 338-3395.

(6) Preinesberger, C.; Vandre, S.; Kalka, T.; Dahne-Prietsch, M. *Journal of Physics D* **1998**, *31*, L43-L45.

(7) Chen, Y.; Ohlberg, D. A. A.; Medeiros-Ribeiro, G.; Chang, Y. A.; Williams, R. S. *Applied Physics Letters* **2000**, *76*, 4004-4006.

(8) Nogami, J.; Liu, B. Z.; Katkov, M. V.; Ohbuchi, C.; Birge, N. O. *Physical Review B* **2001**, *63*, 233305.

(9) Lopinski, G. P.; Wayner, D. D. M.; Wolkow, R. A. *Nature* **2000**, *406*, 48-51.

(10) Cicero, R. L.; Chidsey, C. E. D.; Lopinski, G. P.; Wayner, D. D. M.; Wolkow, R. A. *Langmuir* **2002**, *18*, 305-307.

(11) Wayner, D. D. M.; Wolkow, R. A. *Journal of the Chemical Society, Perkins Transactions* **2002**, *2*, 22-34.

(12) Lu, P. H.; Polanyi, J. C.; Rogers, D. *Journal of Chemical Physics* **1999**, *111*, 9905-9907.

(13) Lu, P. H.; Polanyi, J. C.; Rogers, D. *Journal of Chemical Physics* **2000**, *112*, 11005-11010.

(14) Hegner, M.; Wagner, P.; Semenza, G. *Surface Science* **1993**, *291*, 39-46.

(15) Wagner, P.; Hegner, M.; Guntherodt, H. J.; Smemnza, G. *Langmuir* **1995**, *11*, 3867-3875.

(16) Wagner, P.; Zaugg, F.; Kernen, P.; Hegner, M.; Semenza, G. *Journal of Vaccum Science & Technology B* **1996**.

(17) Examples of conventional physical vapour deposition process include thermal evaporation, electron-beam evaporation, sputtering and laser-ablation.

(18) Ferguson, G. S.; Chaudhury, M. K.; Sigal, G. B.; Whitesides, G. M. *Science* **1991**, *253*, 776-778.

(19) Kim, C.; Burrows, P. E.; Forrest, S. R. *Science* **2000**, *288*, 831-833.

(20) Zaumseil, J.; Meitl, M. A.; Hsu, J. W. P.; Acharya, B. R.; Baldwin, K. W.; Loo, Y.-L.; Rogers, J. A. *Nano Letters* **2003**, *3*, 1223-1227.

(21) Material being transfer from the templating surface to the TS metal surface during stripping is an issue of concern for template-stripping techniques. In particular, template-stripping process which involve mica

are often observed to transfer smalls pieces of mica from to the TS surface during stripping.

(22) Ulman, A. *Chem Rev* **1996**, *96*, 1533-1554.

(23) Schreiber, F. *Progress in Surface Science* **2000**, *65*, 151-256.

(24) Schwartz, D. K. *Annual Review of Physical Chemistry* **2001**, *52*, 107-137.

(25) Filler, M. A.; Bent, S. F. *Progress in Surface Science* **2003**, *73*, 1-56.

(26) Smith, R. K.; Lewis, P. A.; Weiss, P. S. *Progress in Surface Science* **2004**, *75*, 1-68.

(27) Wink, T.; van Zuilen, S. J.; Bult, A.; van Bennekom, W. P. *Analyst* **1997**, *122*, 43R-50R.

(28) Chen, J.; Reed, M. A.; Rawlett, A. M.; Tour, J. M. *Science* **1999**, *286*, 1550-1552.

(29) Chen, J.; Wang, W.; Reed, M. A.; Rawlett, A. M.; Price, D. W.; Tour, J. M. *Applied Physics Letters* **2000**, *77*, 1224-1226.

(30) Gooding, J. J.; Pugliano, L.; Hibbert, D. B.; Erokhin, P. *Electrochemistry Communications* **2000**, *2*, 217-221.

(31) Luo, Y.; Collier, C. P.; Jeppesen, J. O.; Nielsen, K. A.; Delonno, E.; Ho, G.; Perkins, J.; Tseng, H.-R.; Yamamoto, T.; Stoddart, J. F.; Heath, H. R. *ChemPhysChem* **2002**, *3*, 519-525.

(32) Chen, Y.; Jung, G.-Y.; Ohlberg, D. A. A.; Li, X.; Stewart, D. R.; Jeppesen, J. O.; Nielsen, K. A.; Stoddart, J. F.; Williams, R. S. *Nanotechnology* **2003**, *14*, 462-468.

(33) Chen, Y.; Ohlberg, D. A. A.; Li, X. M.; Stewart, D. R.; Williams, R. S.; Jeppesen, J. O.; Nielsen, K. A.; Stoddart, J. F.; Olynick, D. L.; Anderson, E. *Applied Physics Letters* **2003**, *82*, 1610-1612.

(34) Wang, W.; Lee, T.; Kamdar, M.; Reed, M. A.; Stewart, M. P.; Hwang, J.-J.; Tour, J. M. *Supperlattices and Microstructures* **2003**, *33*, 217-226.

(35) Wang, W.; Lee, T.; Reed, M. A. *Physical Review B* **2003**, *68*, #035416.

(36) Aslam, M.; Chaki, N. K.; Sharma, J.; Vijayamohanan, K. *Current Applied Physics* **2003**, *3*, 115-127.

(37) Stern, D. A.; Wellner, E.; Salaita, G. N.; Laguren-Davidson, L.; Lu, F.; Batina, N.; Frank, D. G.; Zapien, D. C.; Walton, N.; Hubbard, A. T. *Journal of the American Chemical Society* **1988**, *110*, 4885-4893.

(38) Hickman, J. J.; Laibinis, P. E.; Auerbach, D. I.; Zou, C.; Gardner, T. J.; Whitesides, G. M.; Wrighton, M. S. *Langmuir* **1992**, *8*, 357-359.

(39) Lang, P.; Mekhalif, Z.; Rat, B.; Garnier, F. *Journal of Electroanalytical Chemistry* **1993**, *441*, 83-93.

(40) Katsuaki, S.; Sato, Y.; Yagi, I.; Uosaki, K. *Bulletin of the Chemical Society of Japan* **1994**, *67*, 863-865.

(41) Li, Z.; Chang, S.-C.; Williams, R. S. *Langmuir* **2003**, *19*, 6744-6749.

(42) Petasch, W.; Kegel, B.; Schmid, H.; Lendenmann, K.; Keller, H. U. *Surface and Coatings Technology* **1997**, *97*, 176-181.

(43) Kegel, B.; Schmid, H. *Surface and Coatings Technology* **1999**, *112*, 63-66.

(44) Krüger, P.; Knes, R.; Friedrich, J. *Surface and Coatings Technology* **1999**, *112*, 240-244.

(45) Mozetic, M. *Journal of Microelectronics: Electronic Components and Materials* **2003**, *33*, 222-227.
(46) Li, Z.; Beck, P.; Ohlberg, D. A. A.; Stewart, D. R.; Williams, R. S. *Surface Science* **2003**, *529*, 410-418.
(47) Aita, C. R. *Journal of Applied Physics* **1985**, *58*, 3169-3173.
(48) McBride, J. R.; Graham, G. W.; Peters, C. R.; Weber, W. H. *Journal of Applied Physics* **1991**, *69*, 1596-1604.
(49) Neff, H.; Henkel, S.; Hartmannsgruber, E.; Steinbeiss, E.; Michalke, W.; Steenbeck, K.; Schmidt, H. G. *Journal of Applied Physics* **1996**, *79*, 7672-7675.
(50) Abe, Y.; Yanagisawa, H.; Sasaki, K. *Japanese Journal of Applied Physics* **1998**, *37*, 4482-4486.
(51) Maya, L.; Riester, L.; Thundat, T.; Yust, C. S. *Journal of Applied Physics* **1998**, *84*, 6382-6386.
(52) Abe, Y.; Kawamura, M.; Sasaki, K. *Japanese Journal of Applied Physics* **1999**, *38*, 2092-2096.
(53) Tompkins, H. G.; Tasic, S.; Baker, J.; Convey, D. *Surface and Interface Analysis* **2000**, *29*, 179-187.

Chapter 2: Template-stripped Ultra-flat Metal Surfaces

2.0 Introduction

The fabrication of ultra-flat thin-film metal surfaces via *template-stripping* was first developed roughly a decade ago.[3-5] This development was conducted with the specific objective of producing surfaces on which adsorbed species of molecules could be examined using scanning tunnelling microscopy (STM); conventional physical vapour deposition (PVD) procedures generally produce metal surfaces with considerable roughness on the nanoscale, which convolutes the imaging of adsorbates on the metal surface with the surface topography. While single-crystal metal substrates do provide an ideal alternative in some ways, the associated costs and rigorous preparation procedures severely curtail the use of single-crystal substrates.

The original template-stripping procedure utilized mica as the templating surface, and involved three main steps. First, the mica was freshly cleaved to reveal a large area, ultra-flat surface (ideally, a single atomic plane) and loaded into a vacuum evaporation chamber, where a thin gold film was deposited on the mica. After the film was deposited, the gold-coated mica was removed from the chamber and a solid support was attached to the exposed surface of the Au film using epoxy. Finally, the epoxied solid support was used to lift the Au film away from the mica (due to the low adhesion of Au to mica surfaces), while also providing support to maintain rigidity the gold film.

In the first publication on template-stripped surfaces, Hegner *et al.*[3] demonstrated TS Au surfaces with sub-nanometer roughness over tens of square microns. Such surfaces have been usefully employed for research ranging from the study of adsorbed molecules[4, 6-10] and biomolecules,[5, 11] to the study of the Casmir force between parallel plates.[12] Furthermore, the templating surfaces employed have been expanded to include silicon-oxide,[6, 13] and been shown to work for generating ultra-flat silver.[13]

This range of previous research involving TS surfaces has revealed several uses of the ultra-flat metal surfaces. The full potential of ultra-flat TS metal surfaces, however, could be made much greater with further research. Easily produced and cost-effective ultra-flat thin-film metal surfaces, with well-defined atomic- and nano-scale properties, would be an asset in nanoscience applications, such as sensors, nanoscale electronics and the fundamental study of atomic and molecular interactions with well-defined metal surfaces. In order to realize this potential, progress is required in both expanding the versatility of template-stripping fabrication procedures, and enhancing our scientific understanding of the nanoscale properties of the generated ultra-flat TS metal surfaces. These two areas of research respectively provide the focus for the two sections of this chapter.

Section 2.1 presents three template-stripping techniques developed in this research. The previous demonstration of the template-stripping of Au from silicon-oxide[6, 13] inspired the examination of silicon wafers with a native oxide coating for use as the templates. Prime-polished, ultra-flat silicon wafers appear an ideal templating substrate, both because of their widespread availability, and because of the ease of storing, handling and cleaning them prior to use.

The first fabrication technique presented in subsection 2.1.1 is a basic template-stripping procedure, based strongly on the process of Hegner *et al.*[3] described above. The main adaptation to the procedure described above is the utilization of commercially available silicon wafers in place of mica. Additionally, TS films were successfully prepared using either evaporation or sputtering, and thus both techniques are presented. The remaining two procedures in Section 2.1 focus on expanding the range of environmental conditions in which template-stripped samples can be employed. First, a technique based on replacing the epoxy with metal-metal cold-welding process is presented in subsection 2.1.2, generating TS samples which are compatible with any environment in which the metal materials themselves (and the inert support) are stable. Second, a procedure for template-stripping inside an ultra-high-vacuum (UHV) chamber is described in subsection 2.1.3, which allows the preparation of uncontaminated TS surfaces in a UHV environment for study with a variety of UHV-based surface science techniques.

In Section 2.2, TS Pt and TS Au surfaces fabricated with these procedures are subject to nanoscale physical and chemical characterization. As discussed in Chapter 1, platinum was selected because: the characteristics of Pt are compatible with silicon electronics, make it ideal for a variety of applications, including nanoelectronics and sensors; and TS Pt has not previously been demonstrated. The study of Pt in this chapter provides a foundation for research in subsequent chapters examining techniques for generating novel organic and metal-oxide material surfaces by modifying platinum surfaces. As such, the experimental focus is primarily on the study of TS platinum surfaces, with TS Au surfaces examined concurrently to facilitate comparisons to the previous template-stripping literature discussed above.

The basic characterization of the TS Pt and TS Au surfaces is presented in subsection 2.2.1, including ambient condition AFM and STM, optical reflectivity measurements, water contact angle measurements, XPS and XRD. The ambient condition scanning probe microscopies (SPM) demonstrate that the template-stripping of the Pt and Au films from the ultra-flat silicon-oxide do generate ultra-flat noble metal surfaces. In addition, comparing ambient condition AFM and STM data from the TS Pt and TS Au surfaces reveals that the intrinsic hardness of the platinum relative to the gold is advantageous for achieving the smoothest surface at the nanoscale, as well as for resistance to aging after stripping. Secondly, the optical reflectivity measurements, water contact angle data and XPS results all demonstrate that, immediately after stripping, the TS metal surfaces are free from observable surface contamination by adsorbates, oxides or silicides. Finally, the XRD data reveal that both TS metal films are predominantly <111> oriented in the bulk structure. This is suggestive that the surfaces are likely <111> textured, however further investigation was undertaken to confirm this fact.

In subsection 2.2.2, the UHV template-stripping technique described in 2.1.3 is employed to prepare TS Pt samples for more rigorous nano- and atomic-scale investigation with UHV-STM. This investigation first elucidates the influence of annealing the TS Pt samples while in contact with the templating-surface (pre-stripping annealing). The acquired data provide an understanding of the evolution of the nanoscale physical structure of the TS Pt during the annealing process, and establishes the limits of the annealing process. Furthermore, the UHV-STM data conclusively demonstrate a <111> crystalline texture for the TS Pt surface.

2.1 Template-stripping Techniques

2.1.1 Template-stripping from Ultra-flat Silicon Wafers

As silicon-oxide has been shown to have a low adhesion to noble metal surfaces such as gold,[6, 13] commercially available ultra-flat Si <100> prime wafers with a native thermal oxide layer (typically: 4", P-type; Boron doped; 1-20 Ω·cm; Silicon Valley Microelectronics, CA) were selected as an ideal templating surface. The wafers were first cleaned in piranha solution (a 1:3 by volume mixture of 30% hydrogen peroxide and concentrated sulphuric acid) for fifteen minutes, removing any organic contamination that could be transferred to the deposited metal and/or disrupt the smoothness of the templating surface. Ellipsometric measurements showed that the piranha cleaning procedure also increased the thickness of the oxide layer from ~10Å to ~15Å. The presence of this ultra-thin silicon oxide was found necessary to prevent metal-silicon bonding at the template surface.

Once removed from the piranha, wafers were rinsed thoroughly with de-ionized water, dried under a stream of dry nitrogen , and placed immediately into the PVD chamber. Either sputtering or evaporation was used to deposit the Pt (99.99%) or Au (99.99%) films onto the silicon-oxide template. In the case of sputtering, Pt or Au were sputtered at calibrated rates of 5 and 8 nm/min respectively, with 7 mTorr of argon, to total thicknesses of 100nm or greater. For evaporation, Pt or Au (both 99.99%) were evaporated using an e-beam evaporation system, once the PVD chamber base pressure reached $\leq 10^{-6}$ torr. The evaporation rate was incrementally increased over the period of the evaporation, starting at 0.1Å/sec for the first 50Å, 0.5Å/sec for the next 100Å, and finally 1.0Å/sec for the remainder of the 100 nm thick film. This incremental evaporation process was chosen in order to minimize the heat present at the metal//Si-oxide interface and thus reduce the potential for metal-silicide formation.[14]

After the substrates were removed from the chambers, square pieces of glass or silicon (roughly 1 cm^2) were attached to the exposed side of the Pt or Au surface using EPO-TEK 377 (a two part epoxy that contains no solvent and is resistant to many organic solvents, such as the alcohols typically used in the deposition of molecular monolayers; Epoxy Technologies, MA).[3] The epoxy was cured by placing the wafers in an oven at 150 °C for 2 hours. Once cured, the wafers were placed on the shelf until samples were required. From a single 4" Si wafer, as many as twenty to thirty 1 cm^2 samples could be easily obtained.

To 'strip' a fresh sample from the wafer, a razor blade and metal tweezers were used. First, a sharp razor blade was run around the edge of the sample to separate the sample from excess epoxy on the surface. Then, the point of the tweezers was gently pushed under one corner of a sample and used to pry the sample up. Samples stripped easily without need for chemically assisted stripping, as has been previously required when using mica as the templating surface.[4] The characterization of TS Pt and Au surfaces generated using this process is presented in Section 2.2.

2.1.2 Template-stripping using Cold-welding

One of the main drawbacks of the template-stripping method presented in 2.1.1 (like most conventional template-stripping procedures) is the use of the epoxy. Epoxy adhesives have limited stability in a variety of environments (including many solvents), posing severe limitations on the subsequent sample treatment and applications that the ultra-flat substrates can endure. While ceramic adhesives, offering greater environmental compatibility, have been previously used in place of epoxies,[6] the range of compatibility is still limited, and fabrication procedures involving them are complex. Additionally, procedures involving either epoxies or ceramic adhesives appear to be extremely difficult to convert into a mass-production process.

Samori *et al.*[7] previously presented an adhesive-free template-stripping method based on an electroplating process. Their technique was very successful at creating ultra-flat, completely solvent and UHV compatible TS samples supported on a 200μm sheet of conductive electroplated nickel. While this preparation procedure is potentially useful, the conductivity of the Ni support makes it an unsuitable substrate for the sensor and electronic applications

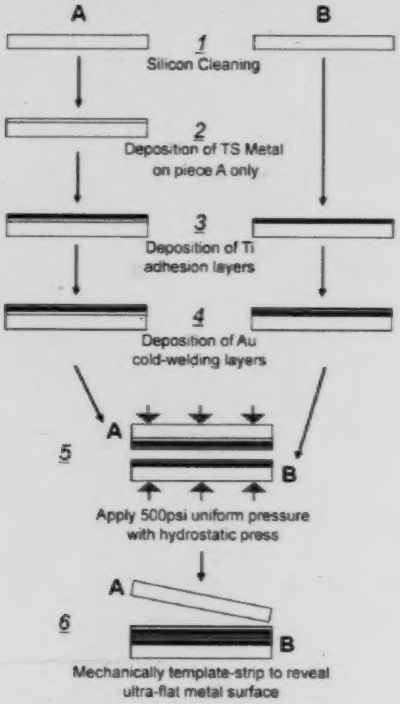
A
B
1
Silicon Cleaning
2
Deposition of TS Metal on piece A only
3
Deposition of Ti adhesion layers
4
Deposition of Au cold-welding layers
5
A
B
Apply 500psi uniform pressure with hydrostatic press
6
A
B
Mechanically template-strip to reveal ultra-flat metal surface

Figure 2-1 Schematic illustration of the cold-welded template-stripping procedure. Expanded detail of each step is provided in the text of the paper.

mentioned above. Additionally, the procedure appears difficult to incorporate into the fabrication of a complex and integrated design hierarchy that is necessary for useful devices.

The procedure presented here employs a cold-welded gold-gold bond[15-17] in place of adhesives or electroplating. This allows the TS metal surfaces to be fabricated directly on standard silicon wafers. The author gratefully acknowledges the contributions of Zhiyong Li and Gun-young Jung to the development of this technique.

The procedure for producing cold-welded template-stripped (CW-TS) samples of ultra-flat metal surfaces is graphically illustrated in Figure 2-1, and the illustrated steps are described in the following text. The metal depositions described in the following steps were carried out using the same procedures described in 2.1.1.

1 Two pieces (**A** & **B**) of silicon <100> prime wafers (P-type; Boron doped; 1-20 $\Omega\cdot\mathrm{cm}$) with native oxide, either $(1\ \mathrm{cm})^2$ or $(1\ \mathrm{inch})^2$, were cleaned in piranha solution (a 1:3 by volume mixture of 30% hydrogen peroxide and concentrated sulphuric acid) for fifteen minutes to remove any organic contamination, and the wafers were rinsed thoroughly with de-ionized water, blown-dry with nitrogen, then immediately loaded into the vacuum deposition chamber. *2* 1000Å of the Pt (99.99%) was then deposited onto only silicon piece **A**. *3* 250Å of titanium (99.99%) was then simultaneously deposited onto both pieces (**A** & **B**) of silicon to act as an adhesion layer and diffusion barrier between the TS Pt and the cold-welding gold layer on **A**. *4* The cold-welding gold layers (~1000Å; 99.99%) were then deposited onto both silicon pieces simultaneously. *5* The two pieces were removed from vacuum and exposed to ambient conditions in a class 100 cleanroom while being transferred to a custom-built hydrostatic press.[18] After various exposure times to laboratory conditions (see below), the two pieces were gently placed with Au films facing each other and touching in the hydrostatic press, and 500psi of pressure was applied normal to the interface between the two pieces for 5 minutes or longer. *6* Once removed from the press, the CW-TS sample 'sandwiches' were mechanically stripped by placing sharp tweezers or a razor blade between one corner of the two silicon pieces and gently applying leverage; the pieces separate easily and in a single step.

Experimentation with this methodology demonstrated that exposure of the samples to ambient laboratory conditions between steps *4* and *5* (prior to cold-welding) gradually reduced the effectiveness of the technique. This decrease in effectiveness was experimentally correlated with the surface contamination of the freshly deposited Au surfaces used for the cold-welding process, using the water contact angle measurements presented in Figure 2-2. As perfectly clean gold is known to be extremely hydrophilic,[19] freshly deposited gold films just removed from the vacuum deposition chamber are expected to demonstrate a very low contact angle. After only 1 minute of exposure to laboratory conditions however, the observed contact angle on fresh gold samples was already greater than 20°, indicating some level of contamination. By ten minutes the contact angle had

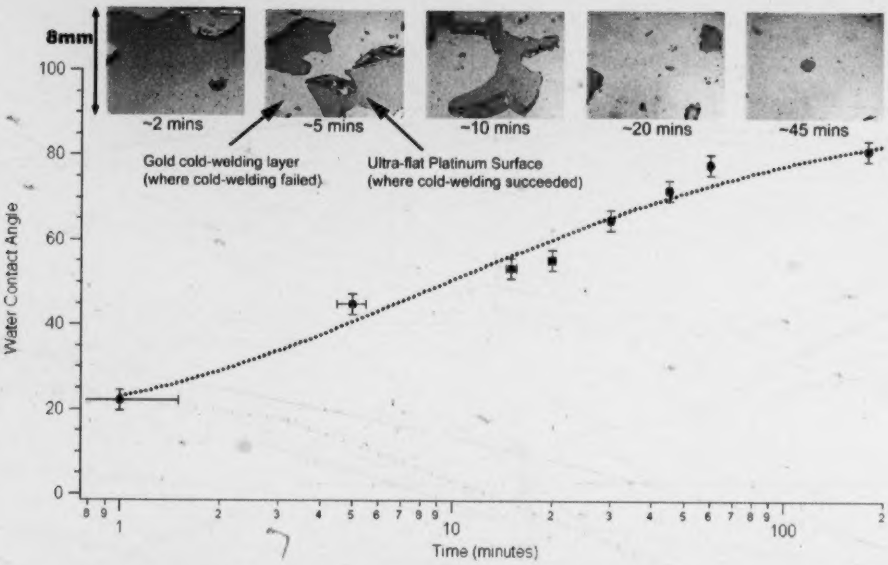

Figure 2-2 Optical pictures of cold-weld produced platinum samples and contact angle of water on gold cold-welding layers, both as a function of exposure time to laboratory conditions. Approximate exposure times are labelled under each optical image, where the dark grey is the ultra-flat TS Pt surface and the light grey is the exposed gold bonding layer underlying the platinum in areas where cold-welding failed (labelled in Figure). The dashed line is a fit to $y = y_{\infty} - y_A * \exp[-t/\tau]$, which describes a first order surface adsorption process.

risen above 50°, and after one hour the saturation value of ~80° was reached. This demonstrates that the adsorption rate of surface contaminants in laboratory conditions onto the clean gold surfaces is quite high, and that some level of contamination is unavoidable, even for short time exposures.

Also shown in Figure 2-2 are representative optical pictures of ~1cm^2 CW-TS Pt samples after stripping (silicon piece **B** in Figure 2-1) that were cold-welded after various exposure times to laboratory conditions (approximate exposure times are given under each picture). The darker areas of the pictures are the stripped ultra-flat platinum surface where the underlying gold layers successfully cold-welded, while the lighter areas are the exposed gold layer on **B** where cold-welding was unsuccessful (labelled in Figure 2-2). On places in the sandwiches where cold-welding was unsuccessful, the Pt-Ti-Au metal layers remained on **A**, though they were easily removed using tape or wiping with cloth, demonstrating that the adhesion to the underlying silicon surface was still very weak. For samples cold-welded within a few minutes of being removed from vacuum, the majority of the metal-layers were transferred. The correlation between the surface contamination and the reduction in cold-welding efficiency is clearly displayed by Figure 2-2.

Despite the contamination issue, the areas of defect free ultra-flat TS platinum produced at minimal atmospheric exposure times are easily large enough for nearly all surface experimental techniques to be conducted. An ideal extension of the template-stripping procedure outlined in this section would be the execution of the cold-welding step in-vacuum using freshly deposited gold films so that contamination is kept to an absolute minimum. An in-vacuum cold-welding system capable of achieving pressures well in excess of those applied in this work has previously been demonstrated inside a physical vapour deposition chamber.[20] Based on previous studies of cold-welding in-vacuum,[21-24] higher cold-welding pressures applied without breaking vacuum after metal film deposition should achieve ideal bonding.

Such a process would allow the easy, and potentially automated, fabrication of ultra-flat metal surfaces, that could be stripped either in-vacuum (for in-vacuum studies of the surface or processes such as SAM formation on the surface) or in laboratory settings up to several months later. In addition, for active devices such as chemically functionalized sensors,[25, 26] the silicon underlying the final ultra-flat metal surface (piece **B**) could incorporate the integrated circuitry required to drive all active device functions. Such circuitry could be fabricated on the silicon prior to carrying out the cold-welded template-stripping procedure. Microcontact-printing techniques based on cold-welding have also been used to fabricate complex microelectronic architectures[16] and multi-layer nanostructures[17] that could be utilized to build advanced integrated device designs incorporating TS surfaces.

The characterization of CW-TS Pt surfaces produced using short exposure to ambient conditions prior to cold-welding revealed no observable differences in surface properties from the TS Pt surfaces generated using the procedure in 2.1.1.

2.1.3 Template-stripping in Ultra-high Vacuum

In the previous section, the contamination of clean Au surfaces upon exposure to ambient conditions was demonstrated. Later in this chapter (2.2.1), similar data are presented on template-stripping films, showing that while un-stripped TS surfaces appear to be contaminant free, even minor exposure to ambient conditions results in observable surface contamination. For surface characterization techniques that study atomic scale defects, chemical composition and atomic periodicity of surfaces (such as STM), even minor surface contamination can obscure surface structure and complicate analysis. As such, characterizations of this type must be performed in UHV environments, on uncontaminated samples.

In many cases, a sample can be loaded into a UHV system from the ambient laboratory environment completely coated with accumulated surface adsorbates and contaminants, and then baked or annealed in order to remove contaminants from the sample holder and substrate surface. Sputter-cleaning with an Ar ion beam is also often used to produce a completely clean surface. However, in the case of TS samples, such annealing and sputtering steps would destroy the original templated surface structure of interest.

The procedure presented here comprises a TS sample geometry and *in-situ* stripping method developed to allow TS surfaces to remain protected by the templating surface until after the sample has been loaded into the UHV system. Once in UHV, the TS surfaces can be annealed while still sealed to their templates. This process both bakes away contaminants from the sample holder that could later migrate to the TS surfaces, and causes evolution in the structure of the TS surfaces while still in contact with the templating surface. After annealing, the samples can be stripped in UHV, revealing uncontaminated TS surfaces for further analysis with surface specific UHV techniques. The author gratefully acknowledges that this process was developed in collaboration with Doug Ohlberg at HP Labs.

The developed procedure is depicted schematically in Figure 2-3. Each TS sample 'sandwich' for UHV study was prepared from two rectangular pieces of

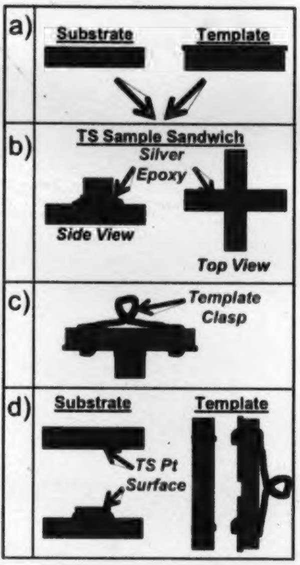

Figure 2-3 Schematic of the in-situ template-stripping procedure used to prepare TS-Pt samples in a UHV environment: (a) Si(001) substrate and Pt film (blue) on SiOx/Si(001) template; (b) TS sandwich structure; (c) template clasp that is used for removal of Si template in UHV; (d) illustration of removal of Pt thin film from Si template and transfer to Si substrate.

silicon, approximately 3mm by 12mm, as shown in Figure 2-3 (a) and (b). Prior to any processing, the Si rectangles were cleaved from larger Si wafers and cleaned in piranha solution (1:3 by volume mixture of 30% hydrogen peroxide and concentrated sulphuric acid) for fifteen minutes. The substrate (the Si surfaces to which the TS Pt film is to be transferred) was cleaved from a highly doped prime Si(001) wafer (N/Arsenic, ≤0.004Ωcm). As with the previous procedures, the templates used in this procedure are p-type Si(001) substrates (P/Boron, 1-20Ωcm).

Immediately following the piranha clean of the Si substrate, the rectangular piece was coated on all sides with layers of Al and Pt (150Å and 200Å, respectively) at a deposition rate of 1Å/sec using an e-beam evaporator in vacuum with a pressure of $\leq 10^{-6}$ torr. The entire Si substrate was encased with Al and Pt overlayers to provide good electrical conduction through the substrates (later used to allow UHV-STM of the TS surface). Immediately after piranha cleaning the Si(001) template, Pt was deposited onto the Si(001) ultra-flat surface in vacuum

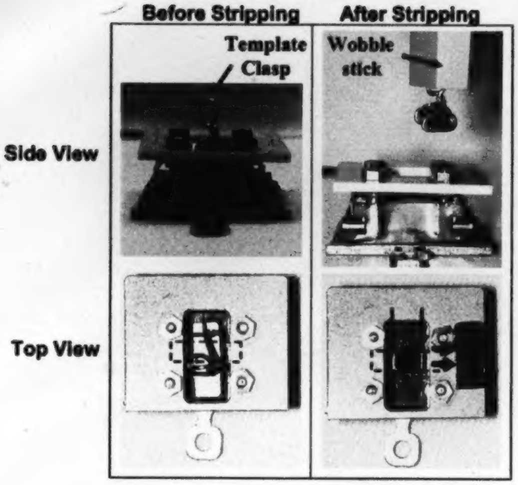

Figure 2-4 Photographs of the *in-situ* UHV template-stripping procedure, both before (Left) and after (Right) stripping, demonstrated on a sample outside of the UHV system.

with a pressure of ≤ 10^{-6} torr. The evaporation rate was incrementally increased over the period of the evaporation, starting at 0.1Å/sec for the first 50Å, 0.5Å/sec for the next 100Å, and finally 1.0Å/sec for the remainder of the 120 nm thick film. This incremental evaporation process was chosen in order to minimize the heat present at the metal/silicon-oxide interface and thus reduce the potential for metal-silicide formation.

Following metal deposition, the rectangular face of the substrate and template were attached to one another with a UHV compatible silver epoxy (Epo-Tek H 21D) to make a TS sample sandwich, shown in steps (a) and (b) of Figure 2-3. The rectangular faces were joined with their long axes orthogonal to one another. In addition to serving as an adhesive, the silver epoxy also provided a low resistance path for electrons through the TS surface to ground during subsequent STM experiments. The joined sandwich was subjected to a brief heat treatment at 180°C for 10 minutes in an oven to cure the silver epoxy, thus completing the fabrication of the TS sample sandwiches.

Prior to loading the samples into the UHV chamber, wires were wrapped around the ends of the Si template and spot-welded to a small wire loop that projects away from the center of the back side of the Si template, forming a clasp as shown in Figure 2-3(c). Next, the TS sandwich was mounted in a sample holder with the Si substrate mounted face up in the sample holder, constraining the metal clasp on the downward-facing template to extend away from the face of the sample holder.

For the experiments presented in this thesis, the sample holder was loaded into an UHV Omicron STM/AFM system with a base pressure of $\leq 10^{-10}$ Torr. Baking of the sample holder and TS sandwich was then carried out in UHV (prior to stripping from the template) at a temperature of 125°C. The time of this anneal was varied in order to examine the evolution of the TS Pt surface structure during the annealing. To carry out the process of *in-situ* template-stripping, a wobble stick is used to grab the wire clasp on the Si template. With the Si substrate held rigidly in place by the sample holder, the wobble stick is given a gentle pull. Due to the poor adhesion of Pt to the oxide layer of the piranha-cleaned Si template, the Pt cleaves easily from the SiO_x surface in the UHV environment and remains attached to the Si substrate via the silver epoxy. As shown in Figure 2-3(d), the fresh template-stripped Pt surface is exposed face up in the sample holder. For clarity, a demonstration of the mechanical stripping process with the wobble stick outside of the UHV chamber is shown in Figure 2-4.

In subsection 2.2.2, TS Pt samples prepared *in-situ* using this process are characterized using UHV-STM, providing the most detailed information to date on the physical structure of a freshly prepared TS metal surface. Beyond the UHV characterization conducted in this thesis, this technique provides the foundation for a variety of studies, including the modification of TS surfaces in UHV, and the examination of the surfaces using UHV surface science techniques.

2.2 Experimental Characterization of Template-stripped Metal Surfaces

2.2.1 Characterization of TS Pt and TS Au

This subsection concentrates on the characterization of TS Pt prepared using the process presented in subsection 2.1.1, with similarly prepared TS Au surfaces characterization alongside for comparison. While all the data presented herein were collected on films prepared using the sputter deposition of the metal films, the data is also generally representative of TS films prepared using evaporation (and the CW-TS process of subsection 2.1.2); the minor differences observed between the TS surfaces were not germane to the central findings presented below. The data presented herein have been reproduced several times using different deposition chambers in different laboratories.

The characterization of the TS surfaces undertaken with the objective of answering specific questions regarding the TS surfaces:

- How well does the nanoscale smoothness of the silicon-oxide template transfer to the TS metal surfaces?
- Are the TS Pt or TS Au surfaces contaminated *prior* to stripping with either with oxide or silica transferred from the silicon-oxide templating surface, or with adsorbed organic contaminants?
- In what crystallographic orientation do the TS metal films grow on the silicon-oxide templating surface?

The following is divided into segments covering the various experimental techniques employed to address these questions. These techniques include AFM and ambient-condition STM, optical reflectivity measurements, water contact angle measurements, XPS and XRD,.

Ambient-Condition Atomic Force and Scanning Tunnelling Microscopies

As the main purpose of template-stripping surfaces from ultra-flat silicon-oxide surfaces is to produce TS surfaces which are similarly ultra-flat, the TS surfaces were first investigated using ambient condition scanning probe microscopies (SPM). Atomic force microscopy (AFM) was carried out in contact mode under ambient conditions using commercial Si_3N_4 cantilevers

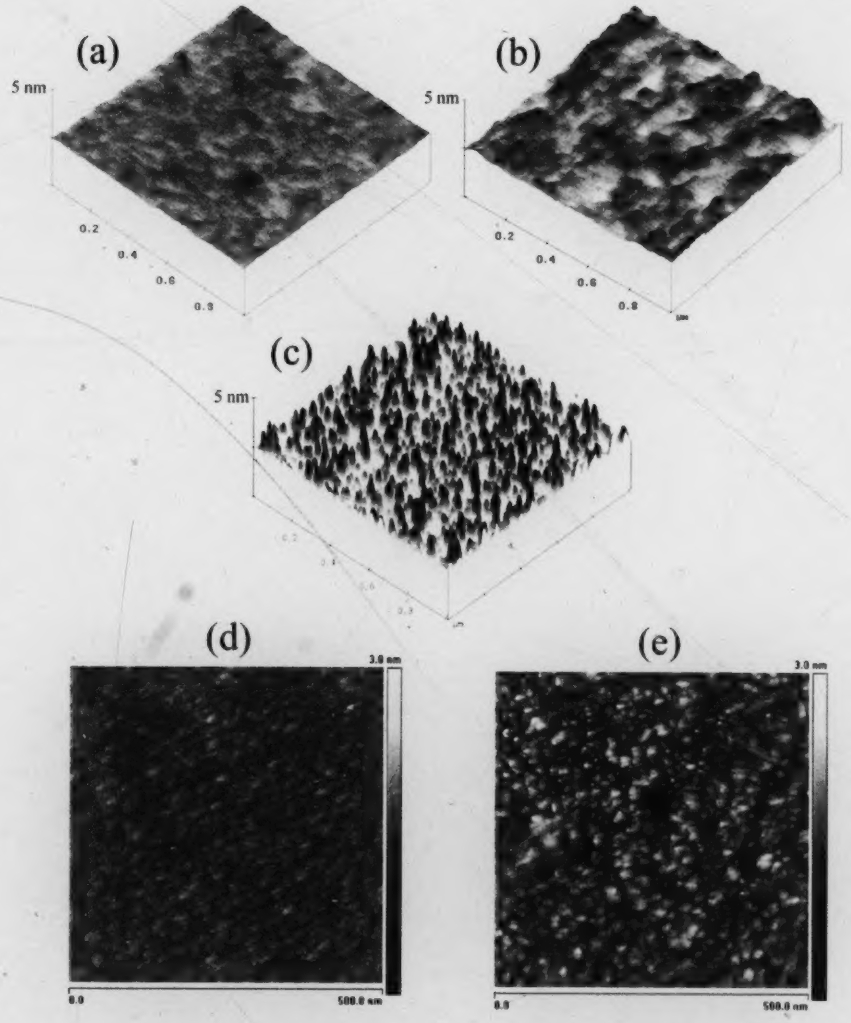

Figure 2-5 Scanning Probe Microscopy (SPM): (a), (b), (c) show AFM images (profile view – 5 nm vertical scale) of TS Pt, TS Au and as-deposited platinum surfaces respectively; (d), (e) show STM images (plan view – 3 nm vertical scale) of TS Pt and Au respectively. All images of TS surfaces were taken immediately upon stripping from the templating silicon; images of the as-deposited platinum were taken shortly after removal from the sputtering vacuum chamber.

(ThermoMicroscope; 0.05-0.5 N/m; radius of curvature ≤ 20nm) and Digital Instruments Multi-mode and Dimension 3000 microscopes. Scanning tunneling microscopy (STM) was carried out on a Digital Instruments Multi-mode microscope using platinum-iridium tips (ThermoMicroscope). Samples of TS Pt

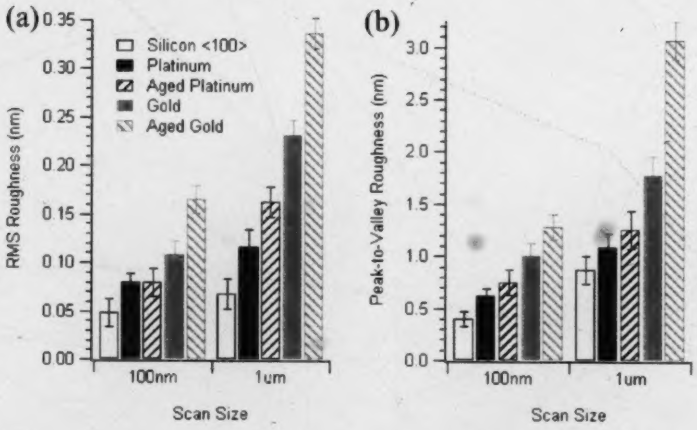

Figure 2-6 (a) Root-Mean-Square (RMS) and (b) Peak-to-Valley (PV) roughness values measured by AFM for 100 nm and 1 μm scan sizes. The surfaces characterized were: piranha cleaned Si <100>; freshly-stripped TS Pt and TS Au; and aged TS Pt and TS Au which were exposed to ambient lab conditions for ~1 week. See legend for labels. Roughness values obtained from STM images are in good agreement with the displayed AFM values.

and Au were stripped immediately prior to loading into the microscope for examination, and all data were collected within 1 hour of the initial stripping. In addition to TS Pt and TS Au films, conventionally sputtered Pt films were also examined in order to provide a basis for comparison; these films were imaged with 1 hour of removal from the sputtering chamber.

Figure 2-5 (a) through (c), respectively, show representative AFM images taken of TS Pt, TS Au and conventionally sputtered Pt films. The successful generation of TS metal surfaces with nanoscale smoothness using the silicon-oxide templates and the procedure described in 2.1.1 is visually apparent in images (a) and (b). Comparing the TS surfaces to the conventionally sputtered film in image (c) demonstrates the advantage of the template-stripping process relative to conventional PVD processes for generating surfaces with uniform nanoscale properties.

In order to quantify the analysis of the surface roughness, the root-mean-square (RMS) roughness and peak-to-valley (PV) roughness values were calculated from the AFM imaging of the surfaces. Several scans, taken at random locations across at least two different samples, were taken with either 0.1 μm or 1 μm scan fields, and the embedded functions of the Digital Instruments software were used to determine the sample roughness of each scan (a first order flattening followed by the roughness calculations). The independent values were then averaged and the standard deviation taken as an estimate of the error on the values quoted below. These roughness values are presented graphically in Figure 2-6. The roughness values obtained from AFM scans of the piranha cleaned silicon-oxide templating surface are also shown as a benchmark for comparison. The 1μm scan RMS and PV roughness values for the conventionally sputtered platinum shown in Figure 2-5 (c) were 0.551 nm and 4.114 nm respectively — both off the scale of their respective plots in Figure 2-6.

The statistical quantification of the surface roughness revealed that the ultra-flatness of the templating silicon-oxide surfaces are transferred with different degrees of efficiency to the TS Pt and TS Au surfaces immediately after stripping. The data in Figure 2-6 demonstrate that TS Pt has better fidelity to the ultra-flatness of the templating silicon-oxide surface than the TS Au. This is also observable in Figure 2-5, as the TS Pt in (a) is notably smoother than the TS Au in (b). Furthermore, this observation is also corroborated by the ambient condition STM data in Figure 2-5 (d) and (e), respectively showing STM images of TS Pt and TS Au. Both a visual inspection and the toughness values calculated from these images are in good agreement with the AFM results, confirming that the TS Pt maintains higher fidelity to the ultra-flatness of the templating silicon-oxide surface.

A second AFM examination of TS metal surfaces was also carried out after samples were allowed to age in ambient laboratory conditions for 1 week after stripping. AFM images of the aged samples are shown in Figure 2-7, and roughness values are also presented in Figure 2-6 (see figure legend). Looking first at the platinum surface, virtually no qualitative change is observable between Figure 2-5 and Figure 2-7, and the roughness values in Figure 2-6 show only a marginal increase in roughness of the aged TS Pt with respect to the fresh TS Pt.

In contrast, significant qualitative changes are observable between the fresh TS Au shown in Figure 2-5 and the aged TS Au in Figure 2-7. Aging has generated considerable surface roughness, including sharper features.

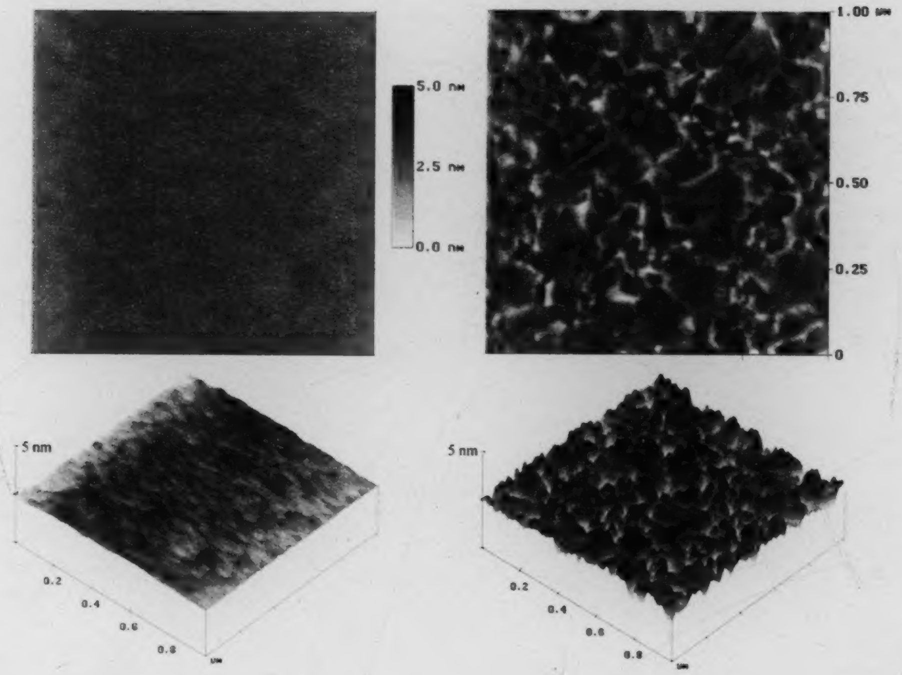

(a) (b)

Figure 2-7 AFM images (plan and profile view) of (a) TS Pt and (b) TS Au surfaces exposed to ambient laboratory conditions for ~1 week after stripping. The vertical scale on all the images is 5nm, as shown by the scale bars.

Quantitatively these changes appear in the RMS and PV values of Figure 2-6. Both measures have increased significantly, particularly at the 1 µm scale where the PV value nearly doubles. This is in agreement with the plan view of the aged TS Au in Figure 2-7, where the aging has induced large height variations at length scales around 100 nm. For scan sizes around 100nm the roughness does not increase as substantially as less features are observed on this length scale.

Both the greater roughness (lower fidelity to the ultra-flatness silicon of the silicon-oxide template) and the significant aging of the TS Au relative to the TS Pt can be understood by considering the intrinsic hardness of the two metals. As Au-Au atomic bonds are weaker than the Pt-Pt bonds — evidenced by the lower melting point of gold (Au:1064°C, Pt:1768°C) — gold will be more malleable at ambient temperatures. As a result, stresses induced in the TS films during the stripping procedure can be expected to cause more distortion in the gold films than in the platinum, producing the observed higher roughness values.

In addition, the weaker Au-Au bonds also allow for greater mobility of Au atoms along the surface at room temperature. Previous STM studies have demonstrated that at room temperature, freshly-prepared atomically flat gold <111> surfaces are mobile enough that they undergo almost continuous reconstruction.[27] Figure 2-7 demonstrates that similar reconstruction of the TS Au surface has occurred over the 1 week period of exposure to ambient conditions. In contrast, the platinum surfaces show almost no change over the same period, due to the much lower mobility of the Pt atoms.

In concert, these SPM data evidence the importance of intrinsic metal hardness for both achieving the highest fidelity of the TS surface to the ultra-flatness of the templating surface and maintaining the ultra-flat surface over time.

Optical Reflectivity Measurements

While the ultra-flatness of the TS metal surfaces is the paramount objective of the template-stripping process, the utility of these surfaces is also highly dependent on other factors, such as their chemical purity immediately after striping. Previous research has demonstrated that template-stripping Au from mica substrates often transfers mica contaminants to the TS Au surface that must be removed by chemical treatment.[4] Concern existed that the reactivity of Pt could lead to a reaction between the Pt and silicon-oxide, resulting in the transfer of oxygen to the Pt surface and forming a thin Pt-oxide layer on the TS surface.

In a recent paper on platinum surfaces, Li *et al.*(2003)[2] demonstrated that the formation of a platinum-oxide layer on platinum surfaces causes a significant decrease in both the refractive index (*n*) and extinction coefficient (*k*). The measuring of the optical constants of the TS films was considered a first order experiment to look for obvious formation of a platinum oxide layer on the TS Pt surface.

Optical reflectivity measurements were made using a Gaertner ellipsometer (Gaertner Scientific Corporation, Skokie, Il), operating at an incident angle of 70° with three different wavelengths (543.5 nm, 632.8 nm and 832.2 nm). A simple model built into the equipment software was used to obtain the refractive index (*n*) and extinction coefficient (*k*) of the platinum samples, where the thickness of the films (≥1000Å) was more than sufficient to assume the ellipsometer was observing only the films and not the underlying substrates; an estimate of the penetration depth (*d*) calculated from the equation $d=\lambda /(4\pi k)$ using measured values of *k* yields depths in the vicinity of only 100Å. Five TS Pt samples, measured at multiple locations on each sample, were examined for the optical constant measurements.

Table 2-1 provides the optical constants measured at three different wavelengths for both TS Pt and fresh metallic Pt surfaces (prepared using conventional sputtering). The excellent agreement between the optical constants of the two surfaces demonstrates that no significant platinum oxide formation transfer is taking place at the interface between the TS platinum surface and the template.

Platinum Surfaces	**543.5 nm**		**632.8 nm**		**832.2 nm**	
	N	***K***	***N***	***K***	***n***	***K***
Fresh Metallic Pt	**1.90**	**4.37**	**2.17**	**4.96**	**3.10**	**6.45**
Template-Stripped Pt	**1.88**	**4.36**	**2.19**	**5.07**	**3.19**	**6.64**

Table 2-1 Refractive index (n) and extinction coefficient (k) measured at three wavelengths for TS Pt and freshly prepared metallic Pt surfaces.

Water Contact Angle Measurements

Beyond the transfer of oxide, a more basic contamination concern is the presence of organic contaminants. While piranha cleaning of the silicon-oxide templating surface prior to the metal deposition was employed to remove organics from the template, the possibility was considered that organic contaminants could migrate between the silicon-oxide template and the TS metal surfaces after deposition. As a test of this possibility, the contact angle of a water droplet on freshly stripped TS surfaces was measured. The water drop contact angle is a measure of the surface hydrophilicity, and previous experiments on clean platinum[28] and gold[19] have both demonstrated a hydrophilic nature (very low water contact angle, ≤ 20°). Within only minutes of exposure to ambient laboratory conditions, however, both metal surfaces are known to become increasingly hydrophobic (water contact angle ≥30°)[19, 28] due to the adsorption of ambient (usually organic) contaminants onto the metal surfaces.

It was also recently demonstrated in the paper by Li *et al.*[2] that platinum-oxide surfaces demonstrate a different water contact angle evolution than fresh Pt as a function of time, due to different rate of adsorption of contaminants from the environment. As such, the measurements of the water contact angle evolution as a function of time also presented a means of verifying the conclusion from the optical data above that no Pt oxide surface layer is present on the TS Pt surface.

The water contact angle measurements were performed using a VCA 100 video contact angle system (AST Products Inc., Billerica, MA). Water drops were lowered onto the surface using a syringe dispenser and expanded to a few millimeters in diameter. Once fully expanded, a digital photograph was captured, from which the contact angle between the edge of the water droplet and the surface were calculated using AST software.

Figure 2-8 plots the measured water contact angle on TS Pt surfaces as a function of exposure time to ambient, up to several hours after stripping. This curve is representative of samples that have sat for anywhere between a few hours to six weeks after being prepared and prior to being stripped. The hydrophilicity of the surfaces immediately upon stripping revealed that the TS Pt appear largely uncontaminated by organic contaminants, even after a significant self-life. This result demonstrated that organic contaminants are not migrating between the Pt surface and silicon-oxide template. Similar data were acquired for Au, demonstrating the same hydrophilicity expected for uncontaminated Au, and good agreement between the temporal evolution of the contact angle for freshly deposited Au and freshly stripped TS Au.

For comparison, data curves are also included in Figure 2-8 for fresh metallic Pt surfaces and Pt films covered in platinum-oxide; the data for both curves are from Li *et al.*[2], and are utilized with express permission. The TS Pt curve in the figure clearly matches that of fresh metallic Pt surfaces, supporting the conclusion

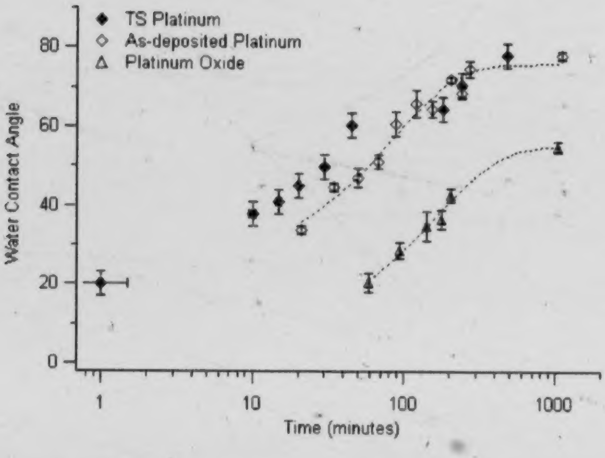

Figure 2-8 Contact angle of water as a function of exposure time to air for platinum films: Template-Stripped, fresh metallic Pt (as-deposited) and Platinum-Oxide coated; see legend. The As-Deposited and Platinum-Oxide data are from Li et al. (2003).[2] (with permission) The dashed lines are a fit to $y = y_{\infty} - y_{\Delta} * \exp[-t/\tau]$, which describes a first order surface adsorption process.

of the optical data that no significant surface Pt oxide is present on the TS Pt surface.

X-ray Photoelectron Spectroscopy (XPS)

While the above results demonstrate that no significant contamination of the TS Pt surfaces was occurring via suspect routes, spectroscopy data were sought as corroboration, and to confirm that no unexpected contamination or contamination at trace levels was occurring. Of the available techniques, angle-resolved XPS (AR-XPS) was selected as the spectroscopic technique of choice. In XPS, the attenuation length of photo-electrons generated in the sample is routinely on the order of nanometers, making the technique extremely surface sensitive. In AR-XPS, the angle of the photoelectron detector is varied with respect to the surface normal while keeping the X-ray bombardment of the surface constant. Analysis of the spectra produced at different electron take-off angles can be then used to provide an depth profile of the surface, up to several nanometers (depending on the density of the material).[29, 30]

The AR-XPS was carried out on an AXIS 165 from Kratos, at the *Alberta Center for Surface Engineering and Science* (ACSES) with the assistance of

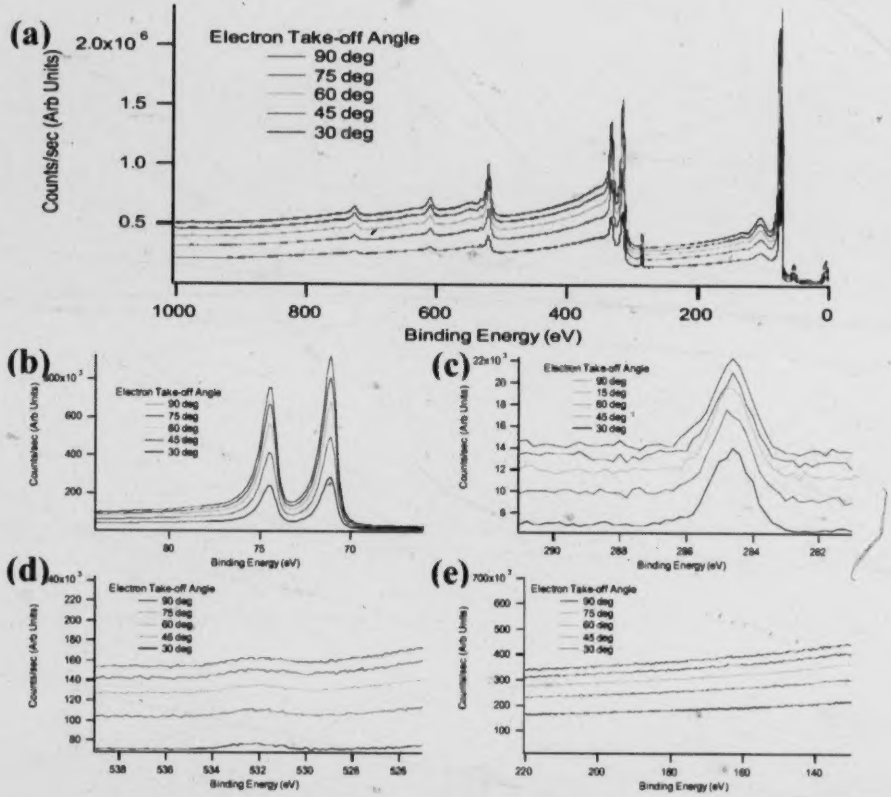

Figure 2-9 AR-XPS results from a fresh TS Pt sample: (a) survey scan; (b) Pt 4f peak range; (c) carbon 1s peak range; (d) O2 1s peak range; (e) Si 2s peak range.

Dimitre Karpuzov. TS Pt samples were freshly stripped in ambient conditions immediately before loading into the AR-XPS vacuum chamber, with exposure times of the stripped surfaces to ambient prior to loading being kept to a minimum (in the range of a few minutes). Despite this short period, however, observable adsorption of molecular oxygen and organic contaminants is expected, as evidenced above by the water contact angle data. Once the samples were loaded into the chamber, XPS spectra were recorded as a function of electron take-off angle over a wide range electron energies.

Figure 2-9 shows the XPS spectra as a function of angle for both the entire scan range (a) and several scan ranges of particular relevance (b-d). Most important are the strong Pt4f doublet peaks shown in Figure 2-9 (b) as a function of electron take-off angle. These peaks correspond precisely with expectations for metallic Pt, and show no evidence of the peak splitting and shifted associated with platinum compounds. This result firmly establishes that the formation of metallic Pt surfaces at the silicon-oxide templating surface is not compromised by chemical contaminants.

As stated above, the contamination of the surface with adsorbed oxygen and organics is expected based on the exposure to ambient conditions. Figure 2-9 (c) and Figure 2-9 (d), respectively, show the carbon and oxygen peak ranges of the XPS spectra as a function of electron take-off angle. The peak positions are respectively associated with adventitious organics and molecular O_2, and the lack of intensity variation of the signals as a function of electron take-off angle confirms that they are both isolated to the top surface of the sample. The XPS peak range for silicon is also shown in Figure 2-9 (e). This region was examined to confirm that no trace of silicon could be detected on the TS Pt surface, ensuring that no silica is transferred from the templating surface to the TS Pt and no platinum silicide is forming.

These spectroscopic results corroborate the conclusion that the freshly stripped TS Pt surfaces are uncontaminated. Similar results were also obtained for TS Au samples.

X-ray Diffraction (XRD)

With the above data demonstrating that the template-stripping from ultra-flat silicon-oxide templates generates surfaces which are both ultra-flat and chemically pure, the main remaining question was regarding the atomic structure of the surfaces. Due to both the weak interaction between the metal atoms, epitaxial growth on the silicon-oxide surface was not anticipated. Rather, the high mobility of the metal atoms on the surface was expected to result in the atoms arranging into the lowest energy configuration. For both Pt and Au, the <111> crystal surface is the lowest energy surface, and thus predominantly <111> textured TS films were anticipated on this basis.

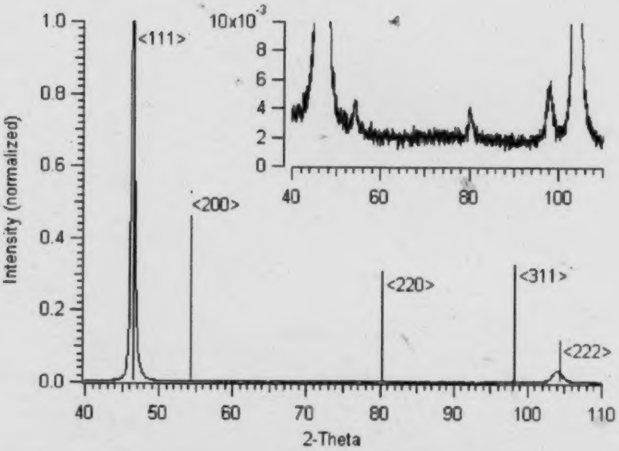

Figure 2-10 Representative X-ray diffraction profile taken from a Template-Stripped platinum sample, along with peak position and intensity markers for polycrystalline platinum from Swanson (1953).[1] Inset shows an enlarged scale.

XRD was selected as a rapid technique for examining the bulk atomic structure of the metal films. The XRD was carried out using a Rigaku Geigerflex 2173 (Rigaku/MSC, The Woodlands, TX) operating with a cobalt X-ray source. This was conducted at the UofA in the Department of Earth and Atmospheric Science, with the assistance of Diana Caird.

Shown in Figure 2-10 is the XRD pattern obtained from the TS Pt samples prepared using sputtering, along with peak position and intensity bars for a polycrystalline platinum from Swanson (1953).[1] Immediately observable is the bulk <111> orientation of the TS Pt film. The <200> and <220> peaks in Figure 2-10 are less than 1% of their expected intensities for randomly oriented polycrystalline platinum (representing the <100> and <110> orientations respectively). It is important to note, however, that these data do not confirm that the *surface* of the TS films are predominantly <111> textured — only that the bulk structure of the films are so oriented. Confirmation of the <111> texture of the surfaces required direct examination of the surfaces using techniques such as UHV-STM, which are employed later in this chapter.

An average crystallite size (D) for the metal film was also calculated from the diffraction data in Figure 2-10 using the Scherrer equation: $D \approx \frac{0.9\lambda}{\beta \cos\theta}$ (λ is X-ray wavelength; β is the corrected full-width at half-maximum in radians of the <111> peak in Figure 2-10; and θ is the Bragg angle of the XRD peak).[31] A crystallite size of ~21 nm was calculated for the TS Pt films. Comparatively, a somewhat larger crystallite size of ~38 nm was calculated for sputtered TS Au from similar XRD data. Looking back at the ambient condition STM images in Figure 2-5, the resolution is sufficient to reveal the metallic grain sizes at the TS surfaces. In the STM images, the surface grain size for both TS surfaces appears roughly ~30% smaller than the bulk grain size calculated from the XRD data, as is expected due to various crystallite cross-sections occurring at the surface interface.

2.2.2 UHV-STM of TS Pt

In order to further investigate the nano- and atomic-scale, the *in-situ* template-stripping technique presented in 2.1.3 was developed to prepare TS samples for examination using UHV-STM. The superior resolution of UHV-STM relative to the ambient condition STM employed above allowed for the nanoscale structure of the TS surfaces to be investigated in greater detail. The UHV-STM focused on addressing two remaining questions, deemed of particular importance for understanding the TS noble metal surfaces:

- How is the nanoscale surface structure of a TS noble metal surface influenced by annealing (heat-treatment) of the samples, while the TS surface is still in contact with the templating silicon-oxide?
- Is the atomic-scale texture of the surface reflective of the bulk <111> orientation of the TS films?

The author gratefully acknowledges Doug Ohlberg, Regina Ragan and Sehun Kim for acquiring the STM images presented in this subsection. The author prepared the TS samples, conducted data analysis and worked with the other scientists throughout the STM data collection. This data is included in this thesis with the express permission of the other scientists.

Influence of Pre-stripping annealing

The grain size of the TS metal films prepared using the specific procedure described in 2.1.1 was determined in the previous subsection by the XRD and ambient condition STM data. The procedure outlined in 2.1.1 involves the curing of the epoxy for 2 hours at 150°C, which also serves as an annealing period for the TS surfaces. It was expected that different annealing conditions for the TS films — while in still in contact with the templating silicon-oxide surface — would result in crystallite grain growth. In addition, it was also anticipated that the annealing process could also generate changes in the nanoscale physical structure of the TS surfaces.

Three TS Pt samples, prepared as described in 2.1.3, are examined by UHV-STM in this subsection. The only parameter varied between the three samples was the duration of the 125°C anneal in the UHV chamber prior to template-stripping; the anneal times employed were 0 hours, 18 hours and 144 hours. After the annealing and template-stripping, the STM imaging was conducted using an Omicron UHV-STM system, at a base pressure of $\leq 10^{-10}$ Torr.

Representative images of the three surfaces with $(500\text{nm})^2$ and $(100\text{nm})^2$ dimensions are shown respectively in Figure 2-11 and Figure 2-12; the duration of the anneal increases from (a) to (c) in both figures. Immediately evident from the images is the expected growth of the crystallite grain size with annealing time. With no annealing (0 hours), the average crystallite size appears in the range of ten nanometers in diameter. After annealing for 18 hours, this grain size has increased to roughly 30 nanometers, and by 144 hours the grains have reached several hundred nanometers in size. This demonstrates that subtle differences in bulk film structure (such as different crystallite grain size), generated by the use of different PVD techniques or deposition conditions, can be overwritten by the post-deposition and pre-stripping annealing process.

Turning to the evolution of the surface nanostructure with annealing time, Figure 2-12 (a) demonstrates a large number of highly irregular and randomly oriented terraces, with the steps between terraces showing large curvature and virtually no oriental relationship to neighbouring steps. This is physical structure

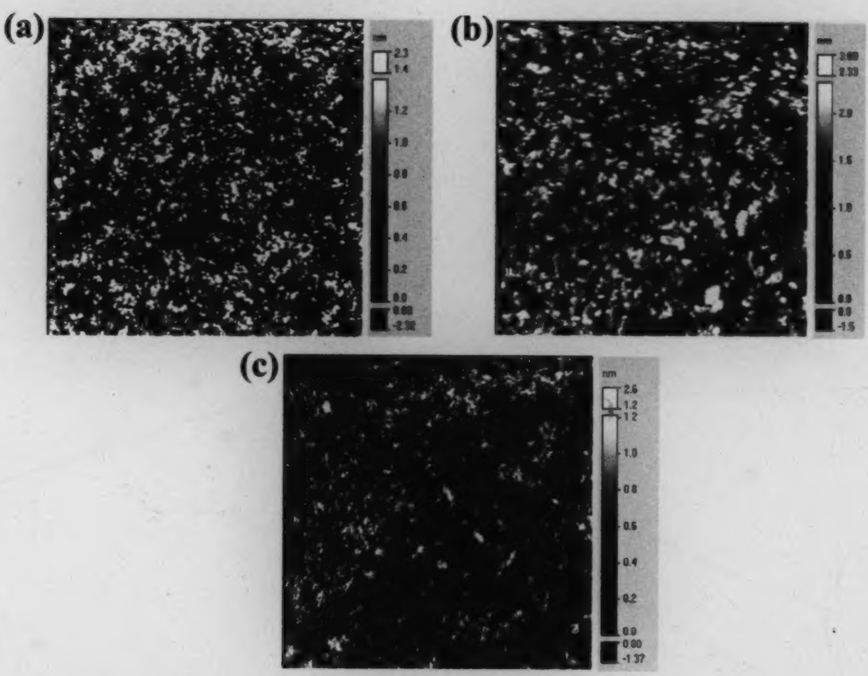

Figure 2-11 {500nm}^{2} UHV-STM topography images, taken in constant current mode, of TS platinum samples stripped in-situ in the UHV environment. Samples were annealed at 125°C prior to stripping for (a) 0 hours {-0.23Vgap, 2.0nA} (b) 18 hours {-1.0Vgap, 1.03nA} and (c) 144 hours {-1.07Vgap, 1.13nA}. (Listed in brackets are the constant current gap voltage and the current used to acquire each image.)

of the un-annealed TS surface is likely the result of metal crystallites random nucleating on the silicon-oxide surface during the initial deposition of the metal film. Conversely, after the 144 hour pre-stripping anneal, Figure 2-12 (c) shows significant linear correlation between the alignment of neighbouring steps; Figure 2-12 (b) shows the 18 hour anneal TS Pt surface at an intermediate stage between the other two. Whereas the crystallite expansion discussed above is due to the coalescing of neighbouring grains, the rearrangement of the step edges is occurring at the atomic-scale on the surface of individual crystallites. This evidences the high mobility of the Pt atoms (and thus step edges) at the TS Pt/silicon-oxide interface. The gradual linearization and alignment of the step edges reflects the movement of the Pt atoms towards a nanoscale surface structure with the lowest energy configuration possible.

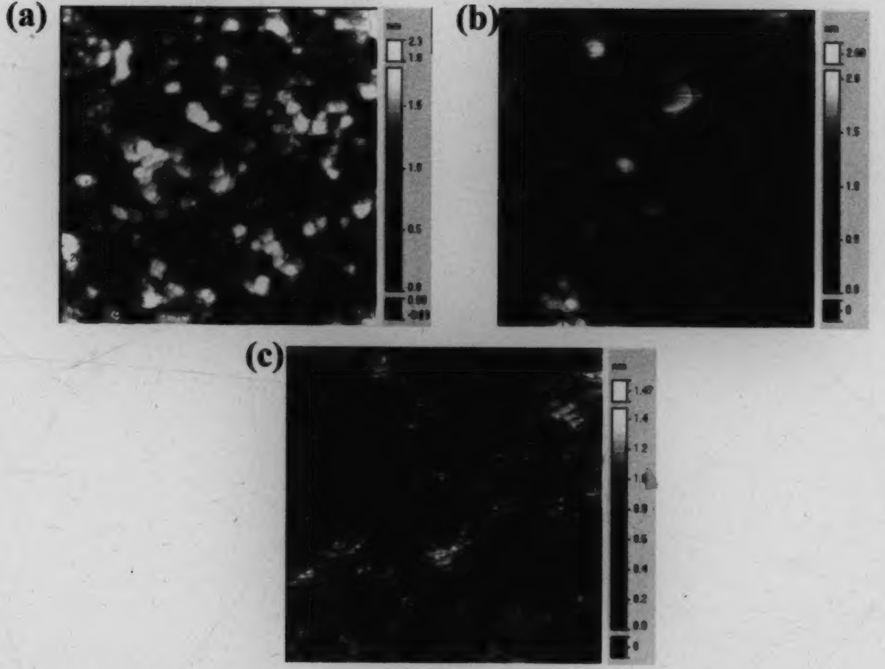

Figure 2-12{100nm}^{2} UHV-STM topography images, taken in constant current mode, of TS platinum samples stripped in-situ in the UHV environment. Samples were annealed at 125°C prior to stripping for (a) 0 hours {-0.1Vgap, 2.0nA} (b) 18 hours {-0.6Vgap, 1.7nA} and (c) 144 hours {-1.07Vgap, 1.13nA}.

Examining Figure 2-12 (b) and (c) more closely also reveals that the number of steps on the TS Pt surface has increase with longer annealing times. For surfaces exposed only to free-space (vacuum), the formation of steps is generally associated with a higher energy landscape, and thus is not anticipated to result from during an annealing process. Rather, highly mobile steps generally coalesce (a process called step-bunching), forming fewer steps of greater magnitude. For the TS Pt surface, Figure 2-12 (b) and (c) shows that the annealing causes the formation of a greater number of steps, but with the average step height tending towards being only a single-atom in height.

To understand this observation, the additional constraints caused by annealing while in contact with a templating surface must be considered. For step-bunching to occur on the TS surface, the multi-atom high steps that would form would have to create regions where there were no Pt atoms in contact with the Si-oxide surface. The energy cost of forming such a void are expected to be significantly greater the decrease in energy associated with a less stepped surface structure. Conversely, the formation of a greater number of single-atom steps on the surface enables the TS surface to establish more uniform contact with the ultra-flat templating silicon-oxide. Indeed, this is demonstrated by examining the evolution of the surface roughness during the annealing process. The RMS roughness of the $(100nm)^2$ images shown in Figure 2-12 were calculated to be (a) 3.7Å, (b) 3.1Å and (c) 1.7Å respectively. The observed consistent increase in smoothness confirms that the formation of the additional single-atomic steps results in the TS Pt surfaces better adopting the ultra-flatness of the underlying silicon-oxide template. These roughness values are expectedly higher than those observed with the ambient condition SPM investigation (though not significantly), due to the greater resolution of the UHV-STM.

The obvious supposition from this data is that longer annealing should produce the optimum TS surface. However, additional investigation of the 144 hour anneal revealed that there are limits to the benefits of the annealing process. Re-considering the ≥100nm grain size observable in Figure 2-11 (c) for the 144 hours annealed sample, and contrasting it to the film thickness of only 100nm, shows the fact that there must very direct routes at crystallite boundaries connecting the front and back surface of the film. Indeed, post-STM examination of the samples using XPS revealed trace amounts of the silver epoxy used for the template-stripping process on the surface of the sample that was annealed for 144 hours; no traces of silver were observed on the other two sample surfaces. Based on this data, it appears as though mobile chemical species from the silver epoxy utilized in this experiment migrated between crystallite grain boundaries and contaminated the TS Pt surface. While a network of boundaries between crystallites also percolates through the films annealed for 0 hours and 18 hours (as the films are still polycrystalline), the pathways crossing the films appear sufficiently convoluted to prevent the material from the silver epoxy from migrating to the surface during the limited annealing period.

This data reveals a critical limitation of the annealing process that must be considered when preparing TS surfaces: the potential contamination of the TS surface with chemical species used in the adhesion of the TS film to the solid support. Adhesion methods utilizing chemical species which are less mobile than the silver epoxy used herein — such as the cold-welding process in 2.1.2 — could potentially limit this observed contamination issue. However, growth of the film crystallites diameters large than the film thickness provides ideal avenues for the diffusion of any possible contaminants, and is therefore not recommended. In cases where very large crystallite size is desirable, annealing could be employed with thicker TS metal films and detailed spectroscopic examination of the TS surfaces to confirm the absence of migrated contaminants from the bask side of the TS film.

Surface Structure

Having established the evolution of the nanoscale features of the surface, the focus now turns to examining the atomic-scale texture of the surfaces. The XRD data at the end of the previous subsection demonstrated the TS films were <111> in the bulk, leading to the plausible conjecture that the atomic texture of the TS surfaces are also likely <111> oriented. Nanoscale UHV-STM images of the TS Pt were obtained in order to explore the atomic-scale texture of the surfaces. The results presented herein were obtained from imaging the TS Pt sample that was subject to the 18 hour pre-stripping anneal period, as the crystallite grain size for the 18 hour sample was closest to that determined using XRD and ambient condition STM for the TS Pt samples prepared using as described in 2.1.1. This was presumed to make the data from the 18 hour sample most representative of the TS Pt surfaces and characterized in 2.2.1.

As a basis for comparison and analysis, the atomic and nanoscale structure of a single crystal Pt(111) sample was also examined using UHV-STM. The single crystal Pt(111) surface was prepared in the Omicron UHV chamber by first sputtering it at room temperature with a 1 kV, *ca* 35 μA Ar ion beam under dynamic flow conditions adjusted to maintain an Ar background pressure of 10^{-5} Torr. After sputtering, the Pt(111) sample was annealed at 500 °C in an O_2

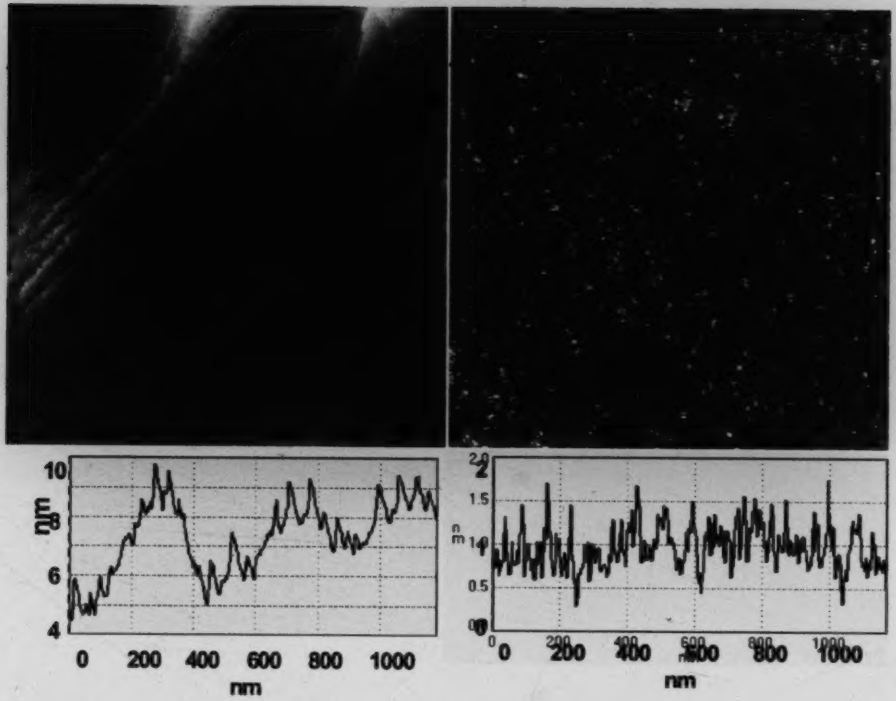

Figure 2-13 (1um)2 STM topography images, taken in constant current mode, of (a) SC Pt(111) {0.58Vgap, 1.66 nA} and (b) TS Pt {1.06 Vgap, 0.91 nA). The blue line on the images denotes the section represented by the line [illegible] on the bottom of the images.

ambient of 10^{-8} Torr. The initial sputter regime was repeated and followed by an anneal in UHV at 500 °C. This process was iterated until STM imaging verified an atomically clean Pt(111) surface.

Shown in Figure 2-13 (a) and (b) are $(1\text{um})^2$ STM images of single-crystal (SC) Pt(111) and TS Pt, respectively. Large, atomically flat terraces are visible on the SC Pt(111) surface. In Figure 2-13 (a), the step edges are parallel to the $\langle 1\bar{1}0 \rangle$ direction and exhibit numerous salients with 60° angles where those sections of the step edge oriented along a $\lfloor 0\bar{1}1 \rfloor$ direction encounter sections oriented along a $\lfloor \bar{1}01 \rfloor$ direction. Qualitatively, the TS Pt surface appears quite dissimilar to the SC Pt(111) surface on the micron length scale. Atomically flat terraces on the TS Pt surface are not distinguishable at this scale, whereas flat

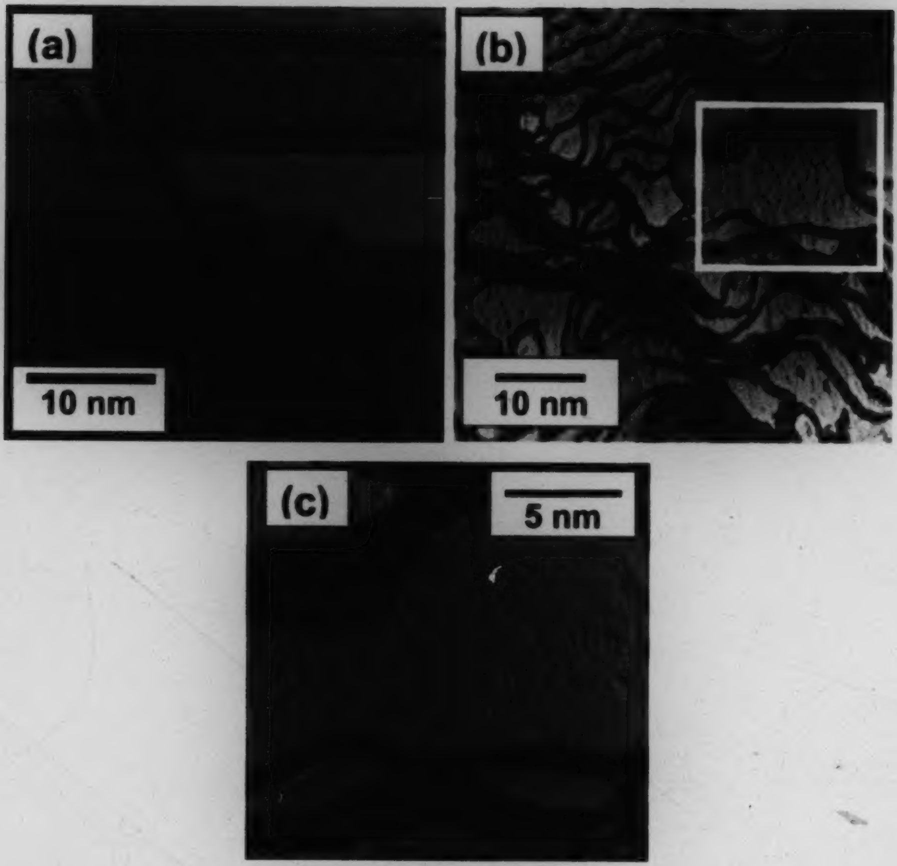

Figure 2-14 (50nm)2 STM topography images, taken in constant current mode, of (a) SC Pt(111) (-0.32 Vgap and 2.42 nA) and (b) TS Pt (-0.66 Vgap and 1.46 nA). (c) The region highlighted by white box in (b) shows the highly kinked step edges. The Laplacian was convoluted with the original STM image for each image to accentuate local curvature.

terraces are observed on the SC Pt(111) surface. Despite the lack of large terraces, however, TS Pt shows smaller variations in vertical topography than SC Pt(111), as evidenced by the cross-sectional profiles provided at the bottom of Figure 2-13. Using RMS roughness as a criterion, the TS Pt surface is quantitatively smoother than SC Pt(111). The RMS roughness values of the two surfaces are 2.7Å for TS Pt versus 29.7Å for the SC surface.

Figure 2-14 (a) and (b) show (50 nm)^2 STM images of both the SC Pt(111) and TS Pt surfaces, respectively, clearly revealing individual terraces and steps on both surfaces. For each of these images, the local curvature at step edges has been accentuated by convoluting the images with their Laplacian; this results in vertical steps between adjacent planes being denoted by the continuous dark lines in the images. The artificial colour scheme used for the terraces emphasizes the vertical displacement between adjacent planes, with significant colour change between adjacent terraces denoting large vertical displacement between them (i.e. large steps). The differences between Figure 2-14 (a) and (b) illustrate the difference in the average vertical displacement between terraces on the SC Pt(111) TS Pt surfaces (i.e. larger in the case of the SC surface). The variation in colour on individual terraces of the TS Pt surface in Figure 2-14 (b) is indicative of an image plane slightly mis-aligned with the plane of the surface terraces; this mis-alignment is caused by the challenge of plane-fitting to the small terrace size in the image. (The image in Figure 2-14 (c) was re-scanned with a smaller scan area, allowing more accurate plane-fitting to be conducted).

Though large terraces are not visible on the TS Pt film at the micron length scale, atomically flat terraces tens of nanometers in width are observed in the higher resolution scan of Figure 2-14 (b). Qualitative differences between the two surfaces are pronounced in Figure 2-14. Whereas the SC Pt(111) surface demonstrates straight terrace boundaries, the terrace edges on the TS surface appear highly kinked and meandering. Although, the terrace boundaries appear curved in Figure 2-14 (b), the higher resolution image taken of the region defined by the white box in Figure 2-14 (b) is shown in Figure 2-14 (c), revealing highly kinked step edges with distinct crystal facets.

Step-bunching is evident on the $(50\ \mathrm{nm})^2$ image of the SC Pt(111) surface, where, on average, adjacent terraces are separated by distances of multiple atomic steps. As discussed above, such step-bunching is expected on the SC surface, whereas it is not observed on the TS surface, due to the constraint placed on the TS Pt surface to conform to the ultra-flat templating silicon-oxide. Figure 2-14 clearly demonstrates that the steps on the TS Pt surface are only one or two atomic layers in height. The dramatic differences in RMS values calculated from the $(1\ \mathrm{um})^2$ images of SC Pt(111) and TS Pt shown in Figure 2-13 stem from step

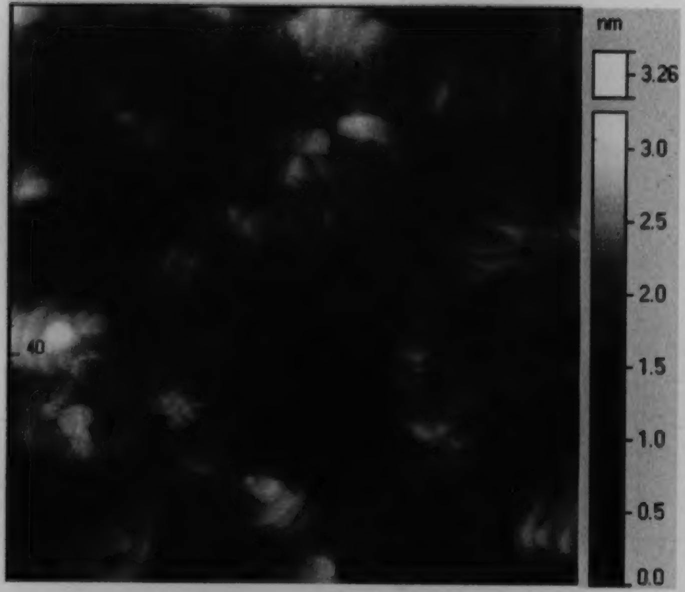

Figure 2-15 A (100nm)2 UHV-STM topography image, taken in constant current mode, of a TS Pt surface {-1.0Vgap, 1.03nA}, demonstrating different rotational orientations of neighbouring <111> textured crystallites.

bunching and multilayer step heights between terraces on SC Pt(111). This is illustrated in the jagged saw-tooth like appearance of the line profile, shown at the bottom of Figure 2-13 (a).

Another observable feature on the TS surface of Figure 2-13 (b), is the lack of a single in-plane crystallographic orientation for neighbouring Pt crystallites; the step edges are not separated by 60° angles as expected for step edges parallel to $\langle 1\bar{1}0\rangle$ on a single crystal surface. On this length scale, grain boundaries are distinguishable due to this in plane misorientation. From both $(50\text{ nm})^2$ and $(100\text{ nm})^2$ images, the crystallite grain size was estimated to be on average ~30 nm in diameter. Shown in Figure 2-15 is a $(100\text{ nm})^2$ STM image of the TS Pt surface, where adjacent crystallite grains show different rotational orientations of terraces and steps. This is in good agreement with observation in the previous subsection that the TS Pt crystallite grains appear to nucleate randomly on the

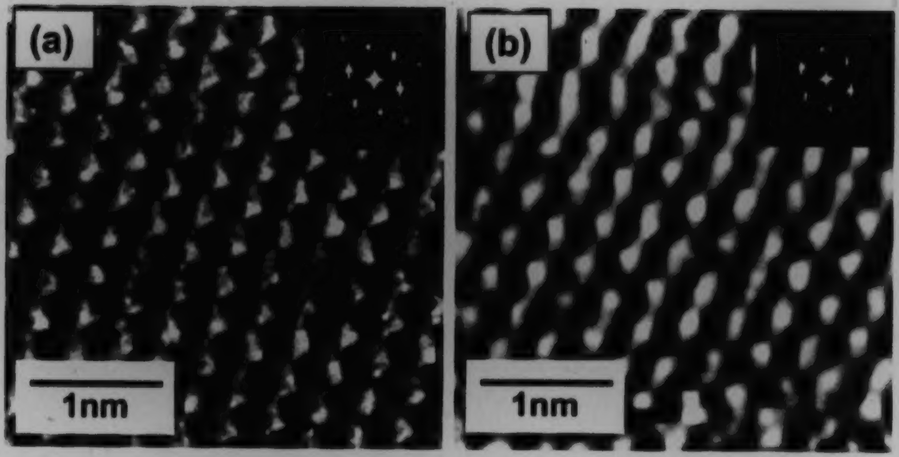

Figure 2-16 High resolution (3nm)^2 STM images taken with current feedback of (a) SC Pt(111), -0.1 Vgap and 2.42 nA, and (b) TS Pt, 0.45 Vgap and 0.85 nA. The 6-fold symmetry of the hexagonal close packed lattice is clearly distinguishable in the images and FFT patterns shown in the insets.

surface during the deposition process, without any epitaxial relation to the templating surface.

From a compilation of STM images of both surfaces, average values for the thickness of a single atomic layer was determined to be 2.7Å ± 0.8Å for the SC Pt(111) surface and 2.5Å ± 0.2Å for the TS surface. The quoted values are an average of at least 10 different measurements on each surface, and the quoted error is the standard deviation of the average — the larger error quoted for the SC surface is due to the fact that the majority of steps observed were multiple atomic layers in height, making the quantification of the single atomic layer thickness more challenging. The measured atomic layer thicknesses are in good agreement with both each other and the value expected for the interplanar spacing between planes of Pt atoms (2.25Å) in the fcc lattice.[32] This suggests that, while the various grains of the TS Pt are randomly rotated in the plane of the surface relative to each other, they appear predominantly <111> vertically orientated.

Atomic resolution STM images of SC Pt(111) and TS Pt surfaces taken on a flat terraces are shown in Figure 2-16 (a) and (b) respectively, each including insets showing the fast Fourier transforms (FFTs) of the images. Both images clearly show a <111> close-packed fcc lattice, and the reciprocal space FFT patterns demonstrate the corresponding 6-fold symmetry of the $\langle 1\,\bar{1}\,0 \rangle$ reflections. Quantitatively, the inter-atomic spacing of the surfaces was determined from the location of the 1st order spots in FFT pattern, yielding values of 2.7Å ± 0.3Å for the TS surface and 2.5Å ± 0.3Å for the SC surface. Once again, the quantitative values show exceptional agreement with each other, as well with the expected value of 2.8Å for the nearest neighbour spacing of Pt atoms in the <111> textured surface.[32] These UHV-STM data confirm that the TS Pt surface is <111> oriented, as was suggested by the XRD observation of the bulk <111> of the TS film.

References

(1) Swanson, T. *Natl. Bur. Stand. (U.S.)* **1953**, *Circ. 539*, I 31.

(2) Li, Z.; Beck, P.; Ohlberg, D. A. A.; Stewart, D. R.; Williams, R. S. *Surface Science* **2003**, *529*, 410-418.

(3) Hegner, M.; Wagner, P.; Semenza, G. *Surface Science* **1993**, *291*, 39-46.

(4) Wagner, P.; Hegner, M.; Guntherodt, H. J.; Smemnza, G. *Langmuir* **1995**, *11*, 3867-3875.

(5) Wagner, P.; Zaugg, F.; Kernen, P.; Hegner, M.; Semenza, G. *Journal of Vaccum Science & Technology B* **1996**.

(6) Stamou, D.; Gourdon, D.; Liley, M.; Burnham, N. A.; Kulik, A.; Vogel, H.; Duschl, C. *Langmuir* **1997**, *13*, 2425-2428.

(7) Samori, P.; Diebel, J.; Lowe, H.; Rabe, J. P. *Langmuir* **1999**, *15*, 2592-2594.

(8) Wong, S. S.; Porter, M. D. *Journal of Electroanalytical Chemistry* **2000**, *485*, 135-143.

(9) Huang, Y. W.; Gupta, V. K. *Macromolecules* **2001**, *34*, 3757-3764.

(10) Huang, Y. W.; Gupta, V. K. *Langmuir* **2002**, *18*, 2280-2287.

(11) Ge, C. W.; Liao, J. H.; Yu, W.; Gu, N. *Biosensors & Bioelectronics* **2003**, *18*, 53-58.

(12) Ederth, T. *Physics Review A* **2000**, *14*, 1466-1471.

(13) Diebel, J.; Lowe, H.; Samori, P.; Rabe, J. P. *Applied Physics A: Materials Science & Processing* **2001**, *73*, 273-279.

(14) Attempts to template-strip metal films deposited at rates of > 2.0 Å/sec for the whole deposition could not be lifted off of the surface, indicative of a reaction (potentially silicide formation) at the metal/Si-oxide interface.

(15) Ferguson, G. S.; Chaudhury, M. K.; Sigal, G. B.; Whitesides, G. M. *Science* **1991**, *253*, 776-778.

(16) Kim, C.; Burrows, P. E.; Forrest, S. R. *Science* **2000**, *288*, 831-833.

(17) Zaumseil, J.; Meitl, M. A.; Hsu, J. W. P.; Acharya, B. R.; Baldwin, K. W.; Loo, Y.-L.; Rogers, J. A. *Nano Letters* **2003**, *3*, 1223-1227.

(18) Chen, Y.; Ohlberg, D. A. A.; Li, X. M.; Stewart, D. R.; Williams, R. S.; Jeppesen, J. O.; Nielsen, K. A.; Stoddart, J. F.; Olynick, D. L.; Anderson, E. *Applied Physics Letters* **2003**, *82*, 1610-1612.

(19) Smith, T. *Interface Science* **1980**, *75*, 51-55.

(20) LEW-15922; Lewis Research Center, NASA: Cleveland, Ohio.

(21) Tabor, D. *Surface Science* **1979**, *89*, 1-12.

(22) Tabor, D. In *Surface Physics of Materials*; Blakely, J. M., Ed.; Academic Press: New York, 1975; Vol. 2, pp 475-529.

(23) Pethica, J. B.; Tabor, D. *Surface Science* **1979**, *89*, 182-190.

(24) Hartweck, W.; Grabke, H. J. *Surface Science* **1979**, *89*, 174-181.

(25) Wink, T.; van Zuilen, S. J.; Bult, A.; van Bennekom, W. P. *Analyst* **1997**, *122*, 43R-50R.

(26) Cornell, B. A.; Braach-Maksvytis, V. L. B.; King, L. G.; Osman, P. D. J.; Raguse, B.; Wieczorek, L.; Pace, R. J. *Nature* **1997**, *387*, 580-583.

(27) Shimoni, N.; Ayal, S.; Millo, O. *Physics Review B* **2000**, *62*, 147-152.

(28) Guo, S.; Hedborg, E.; Lundstrom, I.; Arwin, H. *Thin Solid Films* **1997**, *293*, 179-184.

(29) Cumpson, P. J. *Journal of Electron Spectscopy and Related Phenomena* **1995**, *73*, 25-52.

(30) Opila, R. L.; Eng, J. *Progress in Surface Science* **2002**, *69*, 125-163.

(31) Cullity, B. D.; Stock, S. R. In *Elements of X-Ray Diffraction, Third Edition*; Prentice Hall, Inc.: Upper Saddle River, New Jersey, 2001, pp 167-171.

(32) Noh, J.; Hara, M. *Langmuir* **2001**, *18*, 1953.

Chapter 3: Alkanethiol SAMs on Ultra-flat Metal Surfaces

3.0 Introduction

The chemical self-assembly of ultra-thin films of organic monolayers onto surfaces has received considerable attention as a method of modifying and engineering the properties of surfaces for a wide range of applications.[3-7] In particular, the self-assembly n-alkanethiols onto noble metal surfaces has been widely studied over the past two decades as a model system for investigating the formation dynamics and structures of self-assembled monolayers (SAMs).

From the considerable research that has been done on alkanethiol SAMs, the critical importance of several parameters governing the self-assembly process has been identified. These parameters include: substrate cleanliness[4, 8-12]; n-alkanethiol solution or vapour concentration and self-assembly time (strongly coupled variables)[8, 13-18]; and the crystallographic texture of the metallic surface.[3-5, 19]

Despite the large volume of research however, the influence a variety of important parameters still has yet to be elucidated. For example, the impact of surface roughness[13, 16, 19-25] and metallic substrate material[2-4, 26] on the structure of n-alkanethiol monolayers has only been partially investigated — particularly with respect to correlations between the two parameters. Taking advantage of the ultra-flat TS metal substrates demonstrated in Chapter 2, the research in this chapter explores the influence these two parameters.

The experimental characterization of series of n-alkanethiol SAMs $\{CH_3(CH_2)_{n-1}SH;\ n=6\rightarrow22\}$ formed on ultra-flat TS Pt and TS Au surfaces, as well as on rougher Pt and Au surfaces prepared using conventional PVD techniques, is presented in Section 3.1; the techniques employed therein include ellipsometry, reflection-absorption infrared spectroscopy (RAIRS) and contact angle measurements. The data reveal that the alkanethiol monolayers on the Pt surfaces form with the alkane chains tilted on average at 12° to 15° from the surface normal, unlike the monolayers on Au, which form with an angle closer to

28°. Significant differences between the structures of the monolayers formed on the smooth and rough Pt surfaces are also observed with all three techniques. While the techniques observe much smaller differences between monolayers formed on the smooth and rough Au surfaces, contact angle measurements do demonstrate that the smoother (TS) Au surfaces generate more homogenous and defect free monolayer surfaces.

In Section 3.2, the experimental results are correlated with the physical structure and intrinsic properties of the various metal surfaces. This evaluation points strongly to $\sqrt{3}\times\sqrt{3}$ overlayer relation of the alkanethiol molecules to the Pt atoms of the underlying <111> oriented ultra-flat surfaces. For broader comparison, limited characterization of n-alkanethiol SAMs on conventionally sputtered Ag is also presented, and results on other metals from literature are considered. Comparing the SAMs on Pt to those on Au and Ag reveals notable differences, demonstrating the refractory nature of Pt has a significant influence on the formation and structure of the n-alkanethiol SAMs.

3.1 Experimental Characterization of SAMs

The TS Pt and TS Au surfaces employed in this study were prepared as described in Chapter 2 (subsection 2.1.1). The conventionally deposited, rougher Au surfaces (labelled "as-dep" surfaces) were prepared by sputtering a 10nm adhesion layer of Ti, followed by 100nm of Au, onto fresh piranha cleaned Si substrates; the as-dep Ag films were similarly prepared. The rough, as-dep Pt surfaces were prepared on Si substrates subjected to an argon back-sputter cleaning in the sputtering chamber immediately prior to the deposition of 100-150 nm of Pt. This process results in good Pt film adhesion, eliminating the need for an underlying adhesion layer. The RMS surface roughness values of the two Pt surfaces employed herein, as measured over 1μm^2 by AFM, are presented in Table 3-1. Also included in Table 3-1 are RMS roughness values for other substrates discussed throughout this chapter.

Substrate	RMS Surface Roughness over (1μm)^2
TS Pt	1.1Å
As-Dep Pt	5.4Å*
TS Au	1.7Å
As-Dep Au	5.9Å
As-Dep Ag	14Å
Love *et al.* As-Dep Pd	8Å[‡]

Table 3-1 Average AFM roughness values over (1μm)^2 surface areas for the substrates discussed employed and discussed throughout the text. [†]Reported by Love *et al.* (2003).[17].

Solutions of various length n-alkanethiols $CH_3(CH_2)_{n-1}SH$ (n= 6, 8, 10, 12, 14, 16, 18, 20 & 22 → abbreviated CnSH) were prepared with 99.9% anhydrous ethanol (Aldrich) purged with filtered argon for ≥7 minutes prior to use. Sufficiently concentrated solutions of the n-alkanethiols (1mM ≤ 10mM) and long substrate incubation periods (≥16 hours) were used to ensure complete monolayer formation. As this study focuses only on the static properties of the studied monolayers, these self-assembly conditions were chosen to preclude partial monolayer formation that can occur at lower concentrations and/or shorter incubation periods.[8, 15, 17; 18, 27]

The n-alkanethiols used as received from commercial sources were: C6SH (1-hexanethiol, 95%, Aldrich); C8SH (1-octanethiol, 98.5%, Aldrich); C10SH (1-decanethiol, 96%, Aldrich); C12SH (1-dodecanethiol, 98%, Aldrich); C14SH (1-tetradecadethiol, 98% Fluka); C16SH (1-hexadecanethiol, 95%, Fluka); and C18SH (1-octadecanethiol, 98%, Fluka). C20SH (1-eicosanethiol) and C22SH (1-docosanethiol) were synthesized according to literature procedures and provided to the author courtesy of Zhiyong Li.[8]

Immediately after template-stripping (for TS samples) or removal from the deposition chamber (for as-dep samples), the metal substrates were immersed into the n-alkanethiol solutions (volume: 5mL ≤ 20mL). During the incubation period, the solutions were stored in argon-purged, air-tight containers. When the samples were removed from the n-alkanethiol solutions, they were copiously rinsed with neat anhydrous ethanol followed by Nanopure water (resistivity ≥ 18 MΩ·cm) before being dried under a stream of argon.

3.1.1 Ellipsometry

Ellipsometry was performed on the SAM samples using a variable-angle Gaertner ellipsometer (Gaertner Scientific Corporation, Skokie, Il), operating at three wavelengths (543.5nm, 632.8nm and 832.2 nm) and a typical incident angle of 70°.[28] The complex refractive indexes of the substrates at these wavelengths were determined from readings on bare, fresh substrates, immediately prior to examining SAMs on similar substrates. The thicknesses of the SAMs were calculated using a three-phase model (air-monolayer-substrate) in the Gaertner software, with the refractive index for the n-alkanethiol SAMs assumed to be 1.47 at all wavelengths; a minimum of five different locations on each sample were examined.

Figure 3-1 shows the results of the ellipsometry thickness measurements for the n-alkanethiol SAM series on the two Pt surfaces. Presented as a function of alkane chain-length, the SAMs on both Pt surfaces demonstrate average slopes near the theoretically expected 1.27 Å/CH_2 for vertically oriented, all-trans

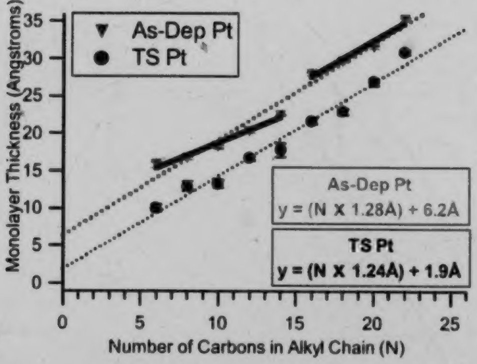

Figure 3-1 Ellipsometry measured SAM thicknesses as a function of n-alkanethiol chain-length for monolayer series on the two Pt surfaces. The displayed error bars are the standard deviation of the set of individual measurements (≥ 5) made for each data point. The two dashed lines are linear best fits to each series respectively (the best fit parameters are provided in the text insets). The two short solid lines are linear best fits to the short (n≤14) and long-chain (n≥16) regimes of the monolayer series on as-dep Pt (the best fit slope values as listed in Table 3-2).

configured alkane chains; the slopes are provided in the figure insets and summarized in Table 3-2.[29] These data suggest that the n-alkanethiol SAMs assemble on Pt with the alkane chains extending close to normal from the surface, as is observed on Ag,[4, 30] and not at the ~30° tilt angle observed on Au.[3, 4] Ellipsometry measurements of the n-alkanethiol SAM series on both the TS Au and the as-dep Au surfaces revealed slopes, also listed in Table 3-2, in good agreement with the expected value of 1.10 Å/CH_2 for alkane chains tilted at ~30° to the surface normal.

Substrate	Slope (Å per CH_2)
TS Pt	**1.24Å ± 0.07Å**
As-Dep Pt	**1.28Å ± 0.08Å**
(n ≤ 14)	(0.85Å ± 0.08Å)
(n ≥ 16)	(1.19Å ± 0.17Å)
TS Au	**1.06Å ± 0.05Å**
As-Dep Au	**1.10Å ± 0.05Å**

Table 3-2 Average increase in SAM thickness per methylene group determined by linear least-squares fitting to the ellipsometry thicknesses of the n-alkanethiol monolayer series on both TS and as-dep Pt and Au surfaces, shown in Figure 3-1. The quoted errors are those of the linear fit to the respective monolayer series.

A more detailed examination of the results presented in Figure 3-1 further reveals that the monolayer series on the two Pt surfaces demonstrate distinct chain-length dependant trends. Looking first at the SAM series on the as-dep Pt, different behaviours in the short ($n \leq 14$) and long ($n \geq 16$) chain regimes are observable. These regimes are denoted in Figure 3-1 by the two independent linear fits (solid lines) to the as-dep Pt series; the slopes of the two fits are also listed in Table 3-2 for reference. Such a division between short- and long-chain regimes has been previously observed by ellipsometry,[1] and other techniques,[2, 8] for alkanethiol SAMs on Au. These previous observations were explained by STM experiments which revealed that shorter chain monolayers on Au exist with a strong 2D-liquid phase (disordered) component at room temperature, whereas longer chain monolayers demonstrate only 2D-crystalline phase(s).[31] Although the observation of two regimes on the as-dep Pt substrates appears qualitatively similar to the behaviour previously observed on Au, however, it is notable that the transition to the short-chain regime (2D-liquid phase) on Au occurs at a significantly shorter chain-length ($n{\sim}8$)[1, 31,32] than the transition to the short-chain regime observed in the ellipsometry data for the as-dep Pt ($n{\sim}14$).

Equally notable is the lack of a similar transition around $n{\sim}14$ for the monolayer series on the TS Pt surfaces in Figure 3-1. Contact angle data presented later in this section does reveal the onset of a short-chain regime at around $n{\sim}8$ on the TS Pt,[33] though this is clearly considerably shorter than the as-dep Pt case. Re-examining the past literature data[1, 2, 8, 31] on Au reveals that the transition from short- to long-chain regimes (2D-liquid to 2D-crystalline) occurs at roughly the same chain-length ($n{\sim}8 \Leftrightarrow 6$), relatively independent of the original Au surface topography — a fact confirmed by RAIRS data presented later in this section. The monolayer behaviour observed here on the Pt substrates appears even qualitatively different than on Au, with the results on Pt showing a strong dependence on surface topography.

3.1.2 RAIRS

RAIRS spectra were acquired using a Nexus 870 FTIR spectrometer (Thermo-Nicolet, Madison, WI) with p-polarized light. Reflected intensity was recorded

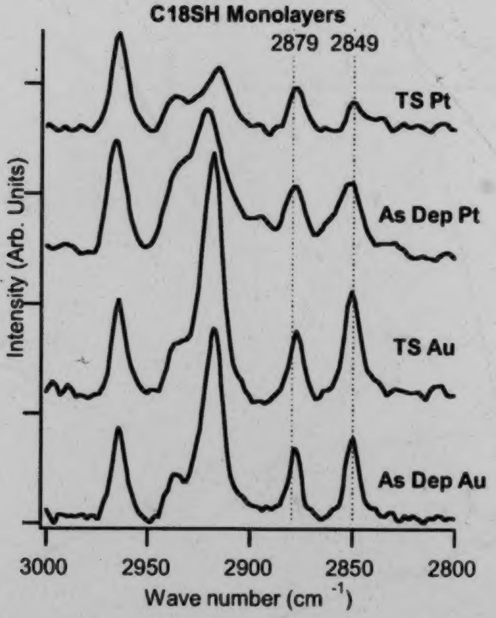

Figure 3-2 RAIR spectra in the C–H stretching region of C18SH SAMs on template-stripped and as-deposited surfaces of both Pt and Au. The position of the two C–H peaks used to calculate the tilt angles (see text for details) are marked with vertical lines: $\nu_s(CH_3)$ 2879 cm^{-1}; and $\nu_s(CH_2)$ 2849 cm^{-1}.

using a liquid nitrogen cooled narrow-band MCT (mercury-cadmium-telluride) detector. Background spectra were recorded using bare, fresh metal substrates immediately prior to taking spectra from SAMs on similar substrates. SAM spectra were averaged over a minimum of 256 scans and obtained with a minimum resolution of 2 cm^{-1}.

Analysis of the RAIR spectra focus on the 3000cm^{-1} to 2800cm^{-1} range, which includes the C–H stretching mode peaks of the alkane molecules. Peak intensities, peak widths and peak positions are all evaluated to provide information regarding the packing and orientation of the alkane molecules in the SAMs. The spectra of C18SH monolayers on the TS and as-dep Pt and Au surfaces, shown in Figure 3-2, are analyzed first.

C18SH

A wide variety of methods for determining an average orientation of alkane molecules in SAMs from the peak intensities of RAIR spectra have been previously developed, ranging in complexity from simple analytical approximations[34, 35] to computationally intensive simulations of RAIR spectra.[36, 37] These methods all make use of the fact that the strong electromagnetic absorption (large k value) of the metal substrates effectively cancels all electric fields perpendicular to the surface normal near the metal surface. Thus, only the surface-normal components of the molecular vibrations in the monolayers appear in the observed RAIR spectra.[34, 35, 38]

Herein we consider only a simple, single alkane chain model for the average molecular orientation, shown in Figure 3-3. Used previously to describe average alkane chain orientations of n-alkanethiol monolayers on a variety of metal surfaces,[2, 17] this model includes only the two variables of alkane chain tilt (θ) and twist (φ). To determine the most suitable model parameters from the RAIR spectra, two different methods were employed. As a first order approximation, the analytical RATIO method of Debe[34] was used. This method directly ratios the peak intensities of the n-alkanethiols in the monolayer to the spectra of the same molecules in KBr pellets; an approximate value for the average tilt angle (θ) of the alkane chains was calculated using the intensities of the $\nu_s(\mathrm{CH_2})$ peak at ~2849 cm^{-1}, and the $\nu_s(\mathrm{CH_3})$ peak at ~2879 cm^{-1}. These two peaks were selected because they were are easily isolated in the monolayer RAIR spectra and clearly discernable in the KBr spectra. Listed in Table 3-3 are the approximate tilt angles calculated from the RAIR spectra in Figure 3-2 using this RATIO method. The analytical RATIO expression used to estimate the tilt angle θ from the RAIR spectra was:

$$\left(\frac{\upsilon_s(\mathrm{CH_2})}{\upsilon_s(\mathrm{CH_3})}\right)_{KBr} \Big/ \left(\frac{\upsilon_s(\mathrm{CH_2})}{\upsilon_s(\mathrm{CH_3})}\right)_{SAM} = \frac{Cos^2(34.75^\circ - \theta)}{Cos^2(90^\circ + \theta)}$$

To verify the results of this simple analytic approach based on only two of the C–H vibrations, simulated RAIR spectra including all the C–H vibration modes were generated from the single chain model using software provided by the Allara research group (Penn State) and described previously by Parikh and Allara.[37] The

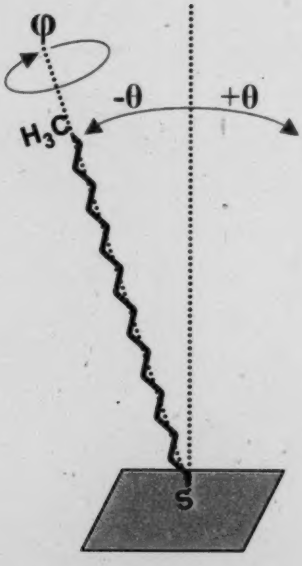

Figure 3-3 A schematic diagram depicting the two variables – tilt (θ) and twist (φ) – of the single chain model used herein to described the average molecular orientation of the alkane molecules in the monolayers. This schematic was adapted from Laibinis *et al.* (1991).[2]

theoretical spectra generated with the tilt angles listed in Table 3-3 (along with a chain twist angle (φ) of 45°) demonstrated reasonable agreement with the corresponding spectra in Figure 3-2, validating the first order approximation of the simplistic RATIO method and the single chain model.

Substrate	Approximate Average C18SH Tilt Angle (θ) from RAIRS
TS Pt	-12°
As-Dep Pt	-15°
TS Au	28°
As-Dep Au	26°

Table 3-3 Approximate molecular tilt angles (θ) determined from the RAIR spectra of C18SH monolayers presented in Figure 3-2, assuming a single chain model. The tilt angles were calculated using a variation of the RATIO method originally presented by Debe (1984)[34] and validated using the computational techniques of Parikh and Allara (1992).[37] (See text for details.)

Considering the tilt angles listed in Table 3-3, good agreement is observed with the conclusion from ellipsometry data that the alkane chins on the Pt surface are oriented significantly closer to the surface normal than the alkane chains on Au. It is also notable that the sign of the tilt angle is negative in the case of Pt, versus positive for the Au case. These results are similar to those presented by Laibinis *et al.*,[2] who employed the same single chain model for the average molecular orientation to explore n-alkanethiol monolayers on Cu, Ag and Au. They observed that the single chain model required a positive tilt angle of $\theta \approx 27^\circ$ for Au, whereas a negative tilt of $\theta \approx -12^\circ$ best agreed with their data on Cu and Ag.[2] Their explanation for this difference was based on different energetic balances between chain-chain and sulphur-substrate interactions on the various surfaces.[2] These results suggest the monolayer structure on the Pt surfaces are similar to those on the Cu and Ag surfaces.

Turning to the differences between the C18SH monolayers on TS Pt and on the as-dep Pt, the higher intensity of the CH_2 peaks at 2918 cm^{-1} and 2849 cm^{-1} on the as-dep Pt is evident in Figure 3-2. Recalling the tilt angle calculation above, this higher CH_2 intensity is the origin of the ~3° higher tilt angle listed in Table 3-3. The greater average tilt angle observed on the as-dep Pt surface is likely the result of disorder in the monolayer packing. This disorder is verified by looking at the peak widths of the CH_2 peaks in the RAIR spectra. Methylene groups in different local packing environments will display slightly different peak positions due to shifts in energy of the vibrations caused by the different surroundings.[1] For a monolayer displaying a highly consistent molecular orientation and packing, the CH_2 peaks should be relatively narrow. Conversely, defects or disorder in the molecular orientation and packing will broaden the CH_2 peaks of the monolayers. Table 3-4 lists the peak widths of the $\nu_s(CH_2)$ peaks for the RAIR spectra in Figure 3-2, showing a substantially larger width of the peaks on the as-dep Pt surface, confirming the presence of higher disorder in the monolayer. The widths (W) were determined from Gaussian best fit ($y = y_0 + Ae^{-\left[\frac{x-x_0}{W}\right]^2}$) to the $\nu_s(CH_2)$ peak of each spectra.

Similarly comparing the C18SH monolayers on the two Au surfaces reveals considerably less difference than is seen on the two Pt surfaces. The fact that the peak width on the as-dep Au is only slightly higher than on the TS Au (see Table 3-4) demonstrates that the added roughness of the initial as-dep Au surface introduces only marginal disorder into the monolayer packing. Although a tilt angle difference of ~2° is observed between the C18SH monolayers on the two Au surfaces, the expression used to estimate the tilt angles from the C18SH RAIR spectra (see above) is significantly more sensitive at higher tilt angles. Thus, only relatively minor variations in the $\frac{\upsilon_s(\mathrm{CH_2})}{\upsilon_s(\mathrm{CH_3})}$ intensity ratio for the 26°⇔28° range are necessary to produce the observed ~2° difference on the Au surfaces, whereas a significantly larger change in the ratio is required in the 12°⇔15° range of the Pt surfaces to produce the observed ~3° disparity.

Substrate	RAIRS $\nu_s(CH_2)$ Peak Width for C18SH Monolayers
TS Pt	**4.8 cm^{-1}**
As-Dep Pt	**8.3 cm^{-1}**
TS Au	**5.0 cm^{-1}**
As-Dep Au	**5.6 cm^{-1}**

Table 3-4 The RAIR spectra peak widths of the $\nu_s(CH_2)$ vibration (around ~2850 cm^{-1}) for the C18SH monolayers on the listed substrates.

In concert, these data demonstrate that the differences in the molecular packing and orientation between the C18SH monolayers on the two Au surfaces are minor by comparison with those observed between the two Pt surfaces. As the roughness of the TS and as-dep surfaces are roughly equivalent for both metals, this result implies that the influence of the initial metal surface roughness on the monolayers is governed by the intrinsic physical properties of the metals themselves.

Using the above analysis of the C18SH monolayers as a benchmark, the RAIRS data on the full n-alkanethiol series, shown in Figure 3-4 and Figure 3-5, are evaluated next.

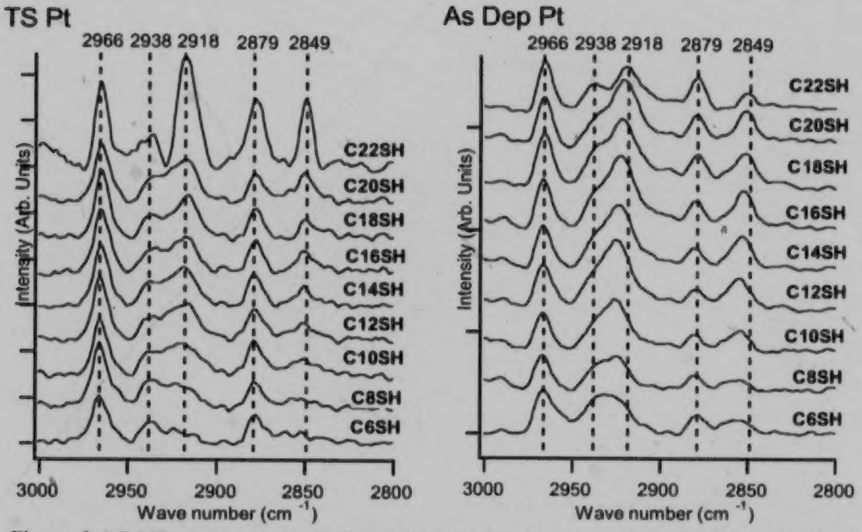

Figure 3-4 RAIR spectra in the C–H stretching region of a series of n-alkanethiol SAMs on template-stripped (left) and as-deposited (right) Pt surfaces. The position of the 5 C–H stretching mode peaks in a solid/crystalline packed monolayer (see text) are marked with vertical lines: $\nu_a(CH_3)$ – 2966 cm^{-1}; $\nu_a(CH_2)$ – 2918 cm^{-1}; $\nu_s(CH_2)$ – 2849 cm^{-1}; $\nu_s(CH_3,FR)$ – 2938 cm^{-1}, 2879 cm^{-1}.

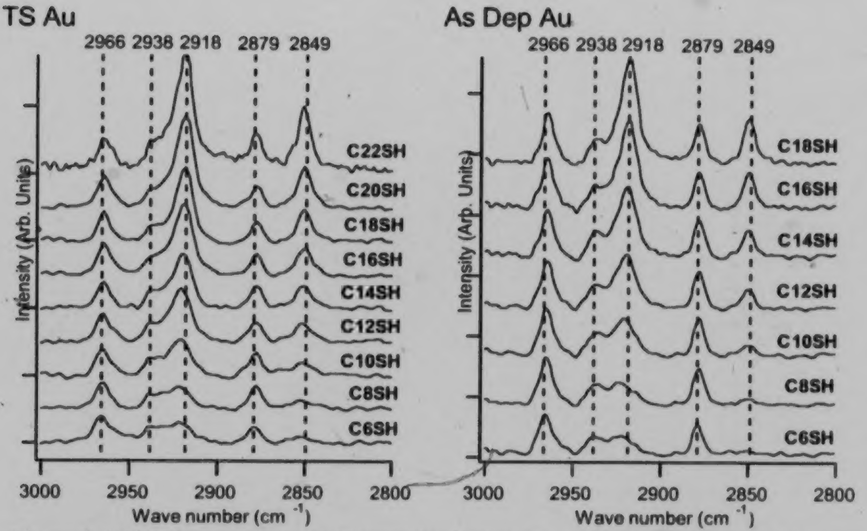

Figure 3-5 RAIR spectra in the C–H stretching region of a series of n-alkanethiol SAMs on template-stripped (left) and as-deposited (right) Au surfaces. The position of the 5 C–H stretching mode peaks are marked as in Figure 3-4.

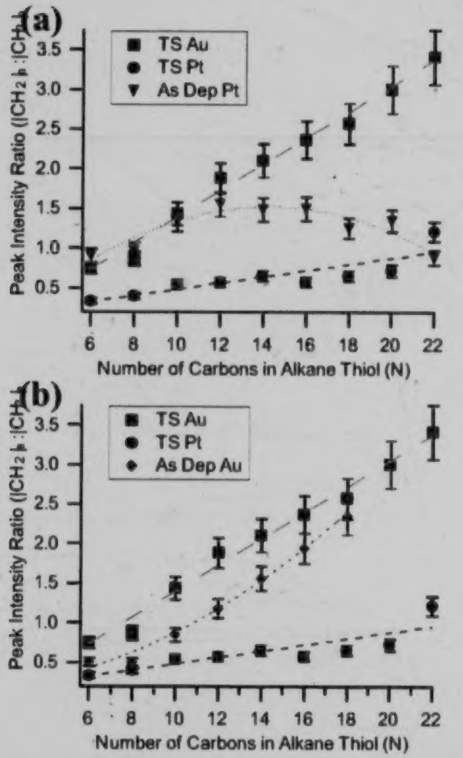

Figure 3-6 Ratio of the anti-symmetric CH_2 and CH_3 peak intensities $\left(\frac{\upsilon_a(CH_2)}{\upsilon_a(CH_3)}\right)$ as a function n-alkanethiol chain-length from the RAIR spectra in Figure 3-4 and Figure 3-5: (a) SAM series on TS Pt, TS Au and as-dep Pt; (b) SAM series on TS Pt, TS Au as-dep Au. Error bars represent the accuracy (±10%) with which the ratio could be determined from the collected RAIR spectra.

Alkane Series

As the calculation of tilt angles for the entire alkane series using the RATIO method described above is problematic due to the low intensity of the $\nu_s(CH_2)$ peak at ~2849 cm^{-1} for short-chain-lengths (observable in Figure 3-4 and Figure 3-5),[39] focus is instead shifted to analysing the intensity ratio between the $\nu_a(CH_2)$ and $\nu_a(CH_3)$ peaks, at ~2918 cm^{-1} and ~2966 cm^{-1}, respectively; both peaks maintain reasonable intensity throughout the alkane series explored. These ratios are plotted in Figure 3-6 as a function of alkane chain-length for the monolayer series on the as-dep and TS Pt and Au surfaces.

Looking at the monolayers on the two TS surfaces (shown in both graphs of Figure 3-6), a consistent linear dependence of this ratio on the chain-length is observed. In other words, the ratio of the CH_2 to CH_3 RAIRS peak intensities increases monotonically with the number of CH_2 groups in the alkane chain. This is as expected for a monolayer series whose molecular packing and orientation is relatively uniform across the range of chain-lengths examined. A dependence of the average molecular packing structure on the length of the alkane molecules would result in pronounced deviations from the observed linearity. The linear trend in Figure 3-6 for the TS Pt surface substantiates the ellipsometry observation that indicated a consistent molecular packing and orientation over the entire alkane length series. The linearity and consistency of the trend on the TS Au surface is equally notable.

This linearity is starkly contrasted by the highly non-linear chain-length dependence of the SAMs on as-dep Pt, shown in Figure 3-6 (a). The prominent deviation from linearity demonstrates that the molecular orientation and packing structure is a strong function of chain-length on the as-dep Pt surface. In good agreement with the ellipsometry data, the as-dep Pt trend in Figure 3-6 (a) demonstrates a transition around n~14 between a short and a long-chain regime. To better understand the nature of this transition, the position of the $\nu_a(CH_2)$ peak is examined as a function of chain-length.

As discussed earlier, the energy of the methylene vibrations is affected by the local environment of the alkane chain. Because different molecular packing schemes and alkane orientations result in substantially different atomic-scale environments for the methylene groups, the positions of methylene peaks in the RAIR spectra can be used to deduce qualitative information about the average packing of the alkane molecules composing the monolayer. In order to extract this information from the peak positions, the position of the peaks in RAIR spectra for alkane chains in bulk solid and bulk liquid states are separately measured.[1] These values are then used as standard comparators for the peak positions observed in the monolayers to determine if the monolayer packing structure is (on average) closer to a 2D-crystalline or 2D-liquid state.[1]

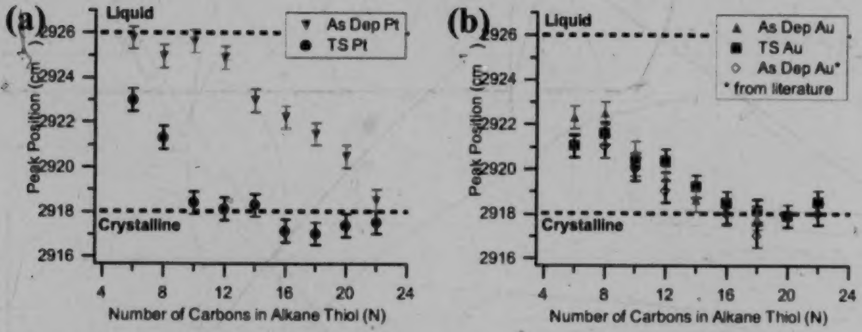

Figure 3-7 Position of the anti-symmetric CH_2 peak {$\nu_a(CH_2)$} from the RAIR spectra in Figure 3-4 and Figure 3-5 as a function of n-alkanethiol chain-length for SAMs on template-stripped and as-dep surfaces of: (a) Pt and (b) Au. Also included in (b) are literature values from a previous study[1] of n-alkanethiol monolayers on as-dep Au. Error bars demonstrate the accuracy (~1cm^{-1} or ±0.5cm^{-1}) with which the peak positions can be stated based on the collected RAIR spectra.

Shown in Figure 3-7 are the peak positions of the $\nu_a(CH_2)$ peak as a function of alkane chain-length, for the spectra displayed in Figure 3-4 and Figure 3-5. The dashed horizontal lines in Figure 3-7 denote the peak positions of the alkanes in bulk solid and bulk liquid states.[40] Examining the peak position series for the as-dep Pt in Figure 3-7 (a), the transition between the short- and long-chain regimes is striking. For the short-chain monolayers ($n \leq 14$) the $\nu_a(CH_2)$ peak position demonstrates an average molecular packing that is liquid-like, whereas for the long-chain monolayers the peak position evolves towards more crystalline packing. These data identify the nature of the transition to the short-chain regime on the as-dep Pt surface as being a shift from 2D-crystalline to 2D-liquid-like molecular packing.

Figure 3-7 (a) and Figure 3-7 (a) both show the behaviour of the long-chain monolayers on as-dep Pt tending towards the consistent 2D-crystalline behaviour observed on the TS Pt. In other words, at sufficiently long chain-lengths, the monolayers appear to overcome the higher surface roughness of the as-dep Pt surface and adopt a similar structure to the monolayers on the ultra-flat TS Pt. Interestingly, Figure 3-7 (a) shows the short-chain phase $\frac{\upsilon_a(CH_2)}{\upsilon_a(CH_3)}$ intensity ratio similar to that observed on the TS Au surface, suggesting an alkane chain tilt much greater than is observed on the TS Pt. Also, looking back at Table 3-2 we see that the slope of the ellipsometry data for the short-chain regime is only 0.85 Å/CH_2, which correlates to an average alkane chain tilt angle of ~50°. Although similarly high tilt angles have been reported[41, 42] on Au(111), they have only been observed for monolayers carefully prepared with incomplete (non-saturated) coverage. Understanding this short-chain 2D-liquid regime on the as-dep Pt surface in detail will require further study, and is beyond the scope of the research herein.

Looking at the TS Pt series in Figure 3-7 (a), the consistent 2D-crystalline packing of the monolayers for all chain-lengths with n≥10 is in excellent agreement with the previous data. We note that for the shorter chains (n=6 and 8) the peak position shifts rapidly away from being crystalline, in direct correlation with the advancing contact angle observation of numerous defects being present in these monolayers. This observation demonstrates that a transition to a 2D-liquid-like regime also occurs on the TS Pt, albeit at significantly shorter chain-lengths than are observed on as-dep Pt; it is noted that substantial qualitative differences between the 2D-liquid-like behaviour on the two Pt surfaces could exist.

The experimental RAIRS data on the two Au surfaces were different from the Pt case. For the C18SH monolayers specifically, the differences between the two Au surfaces were much smaller than the differences between the two Pt surfaces. Figure 3-6 (b) and Figure 3-7 (b) demonstrate that this trend is reflected across the entire monolayer series examined. Figure 3-7 (b) shows a transition from 2D-crystalline to 2D-liquid packing behaviour beginning at n~8, though unlike the Pt case however, the chain-length onset of this transition is unaffected by the roughness of the Au surface. In addition, Figure 3-7 (b) includes the peak position data from Porter *et al.* (1987)[1] in order to emphasize that the consistency of these values across a variety of Au surfaces.

Figure 3-6 (b) shows some differences between the monolayer series on the two Au surfaces that are more pronounced at the lower chain-lengths. Though the impact of substrate surface roughness for monolayers on Au is significantly less than that observed on Pt, these data do indicate that Au surface roughness still has influence on SAM formation and structure, as has been observed previously.[15, 19, 23, 25]

3.1.3 Contact Angle Measurements

SAMs on Pt

The advancing water contact angle was measured for the whole series of alkanethiol SAMs on both rough and smooth Pt surfaces. These measurements were recorded on an AST-VCA 1000 video contact angle system (AST Products, Inc., Billerica, MA). A ~2 μL drop of high-purity Nanopure water (resistivity ≥ 18 MΩ·cm) was lowered onto each sample from a syringe and expanded prior to a video image of the drop being acquired. The drop shape was analyzed using AST software to determine the advancing water contact angle. A minimum of six measurements per sample were averaged to provide the reported contact angles.

The advancing water contact angle data taken for the monolayer series on the two Pt surfaces are presented in Figure 3-8, as a function of alkane chain-length. For the n-alkanethiol monolayers with n≥12 on the TS Pt a consistent contact angle at ~110.5° is observed (marked by the solid horizontal line in the figure), in agreement with expectations for a densely packed, methyl (CH_3) terminated surface.[8] The consistency of the contact angle for these long-chain monolayers suggests a similar consistency in the orientation and dense packing of the alkane molecules composing the monolayers. As the chain-length decreases to n≤10 for monolayers on the TS Pt surface, the observed contact angle begins to systematically decrease. This reveals the presence of defects in the molecular packing and methyl termination of these monolayers. The systematic nature of the decrease indicates a direct correlation between shorter chain-length and higher defect density, demonstrating the onset of a 'short-chain' regime at n~8.

Shifting focus to the monolayer series on as-dep Pt, we see in Figure 3-8 a similar trend of decreasing contact angle at shorter chain-lengths, only this time with a substantially higher onset length of n~14, in good agreement with the ellipsometry data. A higher defect density for the monolayers on the as-dep Pt relative to those on the TS Pt in the range of n≤14 is clearly evidenced by the ~5° lower contact angle.

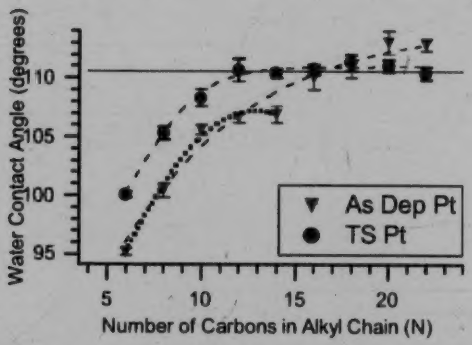

Figure 3-8 Advancing water contact angle as a function of n-alkanethiol chain-length for monolayers on the two Pt surfaces. The displayed error bars are the standard deviation of the set of individual measurements (≥ 6) made for each data point. The two dashed lines are best fit guides-to-the-eye for the monolayer series on the two Pt surfaces. The dotted line is a best fit guide-to-the-eye for monolayers in the short-chain regime on as-dep Pt ($n \leq 14$). The solid horizontal line denotes the a contact angle of 110.5° which is in good agreement with expectations for a primarily CH_3 terminated surface.

Although the $n \geq 16$ range the monolayer series on the as-dep Pt exhibits contact angle values at or above the level expected for a methyl terminated surface, the general trend still deviates from the consistency observed for the long-chain regime on the TS Pt. Rather than settling at a consistent value around ~110.5°, the contact angle for the as-dep Pt series in Figure 3-8 steadily increases from n=16 to n=22. A contact angle higher than 110° is observed[25] for n-alkanethiol monolayer surfaces where significant amounts of methylene (CH_2) groups are exposed. As with the lower contact angles, this behaviour is also indicative of defects in the molecular packing of the monolayer. The difference in this case is that these defects allow water molecules to access only methylene parts of the chain, but not to diffuse down to access the underlying hydrophilic substrate. For long-chains, this suggests that relatively ordered molecular packing still occurs for the lower parts of the alkane chain, protecting the substrate surface, but that disorder in the packing occurs at the upper portions, allowing molecular bending and rotation to expose methylene groups to the water molecules.

SAMs on Au

As the RAIRS and ellipsometry data above revealed only subtle differences between the alkanethiol SAMs on Au, compared with the significant differences observed on Pt, a more complete contact angle study of C18SH monolayers on both rough (as-dep) Au and smooth (TS) Au was undertaken, in collaboration with Kelvin Issacson, in the labs of Daniel Y Kwok. The advancing and receding contact angles[43-45] of several liquids were measured for monolayers of C18SH on the two Au surfaces. The contact angle results for and are presented in Table 3-5.

Liquid	θ_a	θ_r *(deg)*
Water	108.9° ± 1.1°	102.9° ± 3.5°
Formamide	91.6° ± 1.5°	82.8° ± 5.2°
Ethylene Glycol	84.1° ± 1.7°	79.1° ± 4.3°
Hexadecane	44.1° ± 2.8°	39.9° ± 4.7°

Table 3-5 Advancing (θ_a) and receding (θ_r) contact angles for monolayers of C18SH on TS Au. The quoted errors are the 95% confidence limits.

In the ideal limits of assuming a perfectly homogeneous and smooth surface, the values of the advancing and receding contact angle should be identical.[25] In reality however, inhomogeneities and defects on real surfaces result in the contact angle being dependant on whether the drop is expanding (θ_a) or retracting (θ_r) on the surface. Comparing the hysteresis ($H=\theta_a-\theta_r$) observed on chemically similar surfaces provides a good comparator of the homogeneity and density of defects between the various surfaces. The hysteresis values calculated for a variety of liquids on C18SH monolayers on both the TS Au and as-dep Au surfaces are summarized in Table 3-6.

Liquid	***Hysteresis*** $H = \theta_a - \theta_r$	
	Template-Stripped Au	***As-dep Au***
Water	6.4° ± 3.0°	18.9°
Formamide	8.7° ± 3.6°	25.7°
Ethylene Glycol	5.0° ± 2.0°	23.1°
Hexadecane	3.5° ± 0.6°	25.4°

Table 3-6 Contact angle hysteresis ($H=\theta_a-\theta_r$) for C18SH monolayers on TS Au, Annealed Au and Non-Annealed Au. The quoted errors on the TS hysteresis are the standard deviation a series of measurements of the hysteresis. The hysteresis values for the as-dep Au surface were previous reported in Yang et al. (2003),[25] without error values and are reproduced herein as such.

The low hysteresis observed for the monolayers on TS Ay reveals a more homogeneous and defect free surface. Though in the previous subsection the influence of surface roughness for n-alkanethiol SAMs on Au was shown to be dramatically less than on Pt, these results demonstrate that surface roughness is still a crucially important factor for obtaining the highest quality and most uniform n-alkanethiol SAMs on Au surfaces.

3.2 Discussion

Pt Surface Roughness

The cumulative data presented in Section 3.1 demonstrate that surface roughness has a large impact on the behaviour of n-alkanethiol monolayers formed on platinum surfaces. One significant difference revealed between the monolayer series on the ultra-flat TS Pt versus the much rougher as-dep Pt was the longer chain-length at which a transition from 2D-crystalline (long-chain regime) to 2D-liquid (short-chain regime) alkane packing structure occurred on the as-dep Pt. In addition, higher levels of disorder were observed for monolayers of all chain-lengths on the as-dep Pt, though the disparity was lessened by increasing chain-length.

In Figure 3-9, simplistic physical models of the monolayers on both Pt surfaces are presented. The representations of the underlying surfaces were derived from characterizations of these substrates presented in Chapter 2 (as well as in several publications[46-48]). The representation of the TS Pt surface is based directly on the UHV-STM images in Chapter 2, which revealed the surface to be made primarily of atomically flat terraces separated by steps only a single atomic layer in height. The vertical scale in Figure 3-9 is such that the step heights shown on the TS Pt surface are increments of the atomic step height of the Pt(111) surface (~2.25Å) and are roughly to scale (±10%) with the heights of the displayed alkanethiol molecules.

For the as-dep Pt surface, less detailed knowledge of the surface structure is available. XRD results from the as-dep Pt surface demonstrate a bulk <111> orientation. AFM images of the as-dep Pt surface (as shown in Chapter 2) reveal the as-dep Pt surface to be composed of vertical protrusions or islands in the range of ~1-3 nm in height, and on average ~30 nm in diameter. From these results, two representations of the as-dep Pt substrate are proposed in Figure 3-9, with one demonstrating well-defined steps and small terraces, and the other displaying rounder, less-structured features. No claim is made as to which graphic better represents the as-dep Pt surface; these graphics are used simply to facilitate the

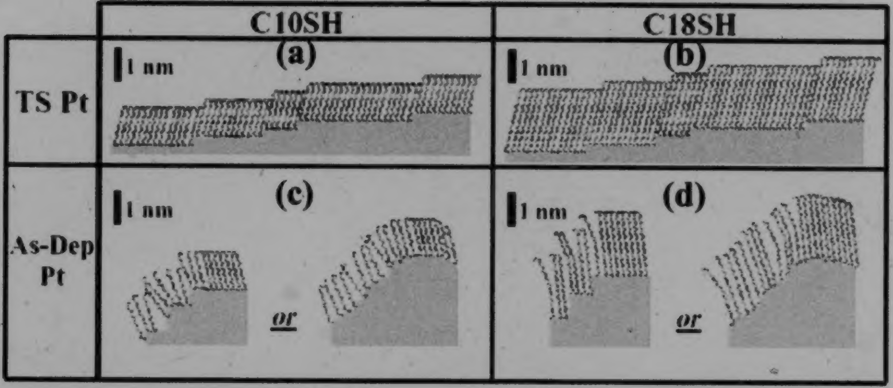

Figure 3-9 Schematic models of (a,c) C10SH and (b,d) C18SH monolayers on (a,b) TS Pt and (c,d) as-dep Pt surfaces. Step heights shown on the TS Pt surface are in increments of the atomic step height of the Pt(111) surface (~2.25Å) and are roughly (±10%) to scale with the heights of the C10SH and C18SH molecules. For a further description of the models, please see the main text.

depiction of the structural properties of the overlying SAM, which are equivalently represented by both schematics.

The experimental observations all demonstrated that the n-alkanethiol SAMs on TS Pt surfaces were densely packed, CH_3 terminated crystalline monolayers, with highly consistent molecular orientation and packing, and very low defect densities for n-alkanethiols of $n \geq 10$. In Figure 3-9 (a) and (b) respectively, the structure of C10SH and C18SH monolayers on the TS Pt are depicted as quite similar. This vertical scale model demonstrates that the topography induced by the single atomic layer steps between terraces is small, even with respect to the length of the C10SH molecule. As a result, it is expected that the amount of additional freedom or flexibility accorded on average[49] to alkane molecules along the step edges to be minimal, resulting in only minor disruptions to the monolayer packing. As the onset of a 2D-liquid, short-chain regime on the TS Pt ($n \leq 8$) coincides with a similar onset chain-length observed on Au,[1, 2, 8, 31] this transition is attributed to the weakening of the intermolecular van der Waals interaction to the point where room-temperature thermal motion of the chains becomes dominant.

On the as-dep Pt surface, on the other hand, the RAIRS data (Figure 3-9 (a)) demonstrate that the C10SH SAMs fall into a 2D-liquid short-chain regime

($n \leq 14$). The experimental observations also revealed a large number of defects that allow access to the underlying hydrophilic substrate (advancing contact angle – Figure 3-8) and a monolayer configuration with a large average tilt relative to the surface normal (ellipsometry – Figure 3-1; RAIRS – Figure 3-6(a)). The illustrations of a C10SH monolayer the as-dep Pt in Figure 3-9(c) demonstrate how these experimentally observed characteristics could arise as a result of the large surface topography of the as-dep Pt, independent of which surface representation is employed. Essentially, at locations of topographical variation on the surface, the intermolecular van der Waals interaction between neighbouring alkane chains is reduced, providing greater orientational freedom for C10SH molecules. The resultant monolayer structure should therefore be less-tightly packed (as depicted in Figure 3-9 (c)), resulting in a more liquid-like average molecular packing environment, a large number of defect-sites, and a more titled average orientation of individual alkane chains.

As the alkane molecules increase in length, the influence of the surface topography on the as-dep surface can reasonably be expected to decrease. Beyond a certain chain-length — when the alkane molecules begin to exceed the height of the average topographic variation on the surface — the influence of the intermolecular van der Waals interactions should begin to reassert and drive the structured packing of the monolayer. This is precisely what the experimental data revealed, showing the transition between the two behaviour regimes on the as-dep Pt was occurring an alkane length of $14 \leq n \leq 16$, equating to a physical chain-length of ~2 nm. This is roughly the vertical size of the major topographical variations observed on the as-dep Pt surface by AFM. Once the alkane molecules exceed this critical length, the characteristics of the SAMs on the as-dep Pt became significantly closer to those of the SAMs on the TS Pt.

The illustrations in Figure 3-9 (d) attempt to capture the long-chain regime ($n \geq 16$) behaviour on the as-dep Pt surface by depicting how the length of the C18SH molecule partially overcomes the as-dept Pt surface topography. Rather than the more dramatic orientational freedom observed for C10SH molecules in Figure 3-9 (c), C18SH molecules in Figure 3-9 (d) are still partially constrained

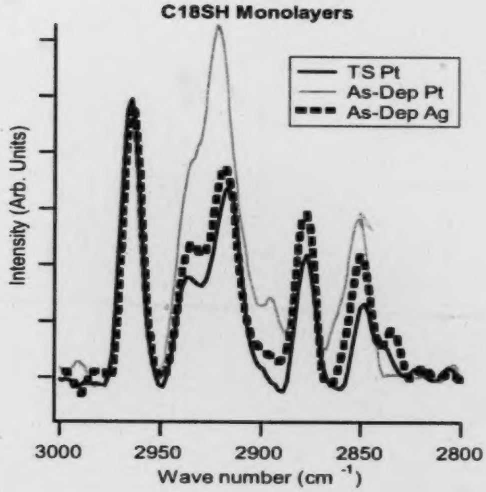

Figure 3-10 RAIR spectra in the C–H stretching region of C18SH SAMs on template-stripped and as-deposited Pt compared with a C18SH SAM on as-deposited Ag.

across the topographical variations. This results in a more crystalline packing of the monolayer and a limitation of defects that allow direct access to the underlying substrate, in good agreement with the RAIRS (Figure 3-7) and advancing contact angle (Figure 3-8) data, respectively. However, as the packing environment remains less rigorous than on the ultra-flat TS Pt surface, the intermolecular van der Waals interactions should still be reduced in the upper portions of C18SH monolayer, and some disorder in the monolayer packing is still expected. This is depicted in Figure 3-9 (d), which shows the upper portions of some C18SH molecules displaying additional orientational freedom and exposing methylene moieties to the surface. The exposure of these methylenes at the surface depiction corresponds well with the advancing contact angle measurements (Figure 3-8), and is supported by the RAIRS observations of average tilt angle (Table 3-3) and CH_2 peak width (Table 3-4).

n-alkanethiol Packing Structure on Pt

As pointed out above, the ellipsometry slope and average tilt angle (θ) of the n-alkanethiol SAMs on Pt appear very close to those observed on Ag. Figure 3-10 directly compares the RAIR spectra from a C18SH monolayer on Ag to those from the two Pt surfaces. In this figure, the correlation between the TS Pt and Ag surfaces is quite evident, suggesting that the molecular packing on TS Pt is indeed similar to that found on Ag. This similarity is initially surprising for two reasons: the very different intrinsic <111> lattice spacing of the two metal surfaces (discussed below); and the RAIR spectra in Figure 3-10 is from a C18SH monolayer on very rough (see Table 3-1) conventionally sputtered (as-dep) Ag surface.

When considering the packing of monolayers on any surface, an important consideration is what monolayer packing structures are commensurate with the substrate lattice. If preferential atomic binding sites for the molecular head group on a periodic crystalline surface exist, then the overlayer structure of the monolayer on this surface should reflect the same periodicity. Presented in Table 3-7 are the lattice spacings of various metal <111> surfaces, alongside which are listed the associated surface areas per alkane molecule for commensurate overlayer structures adopting either of the two basic overlayer schemes commonly associated with n-alkanethiol SAMs on <111> surfaces.[3, 4] At the same time however, the bodies of the molecules will themselves have an optimum packing structure based on steric constraints and the optimization of intermolecular van der Waals interactions. Table 3-8 therefore provides values for the surface area per alkane molecule for various alkane tilt angles, based on the steric diameter of alkane molecules determined from the bulk packing of n-alkanes.[3, 4] The balances between these headgroup-substrate and molecule-molecule (or chain-chain) interactions are thought to generally govern the packing of SAMs.[42]

Metal	Lattice Constant*	Area/Molecule[‡] for a Commensurate $\sqrt{3}\times\sqrt{3}$ Monolayer	Area/Molecule[‡] for a Commensurate $\sqrt{7}\times\sqrt{7}$ Monolayer	Melting Point	Boiling Point
Ag	4.09Å	21.7Å^2/M	**16.9Å^2/M**[†]	962°C	2162°C
Au	4.08Å	**21.6Å^2/M**	16.8Å^2/M	1064°C	2927°C
Pt	3.92Å	**20.0Å^2/M**	15.6Å^2/M	1768°C	3825°C
Pd	3.89Å	**19.7Å^2/M**	15.3Å^2/M	1555°C	2963°C

*All metals listed here have cubic-close-packed crystal structures.

[‡] Calculated from the lattice constant assuming a <111> metal surface plane and the basic overlayer structure defined by Sellers *et al.*[26]

[†] Experimental observations show that the Ag lattice is reconstructed by alkanethiol monolayers to accommodate $\sqrt{7}\times\sqrt{7}$ packing, resulting in an Area/Molecule of between 19 and 20Å^2/M.[30]

Table 3-7 Fundamental material properties of the metals examined and/or discussed in this paper, along with the surface areas per alkane molecule calculated for hypothetical monolayers adopting perfectly commensurate $\sqrt{3}\times\sqrt{3}$ or $\sqrt{7}\times\sqrt{7}$ overlayer structures. Values for area per alkane chain listed in GREY are either not experimentally observed (for Au and Ag) or considered too small to allow for reasonable alkane packing (for Pt and Pd) due to the 18.4Å^2/molecule sterically required by close packed alkane chains in bulk.

Tilt Angle (θ)	Area/Molecule*
0°	18.4Å^2/M
12°	18.8Å^2/M
32°	21.6Å^2/M

*Calculated using the molecule···molecule (M···M) nearest neighbour distance found in bulk n-alkanes.[4]

Table 3-8 Surface areas per alkane molecule for various average monolayer tilt angles (θ), calculated based on the steric diameter of alkane molecules observed for bulk packing of n-alkanes.[3, 4]

The complexity of this balance is emphasized by contrasting the Ag and Au cases in Table 3-7. Despite the nearly identical lattice spacings, the structure of n-alkanethiol monolayers on Au is known to be based on a $\sqrt{3}\times\sqrt{3}$ (abr. $\sqrt{3}$) overlayer basis, whereas the structure observed on Ag clearly demonstrates a $\sqrt{7}\times\sqrt{7}$ (abr. $\sqrt{7}$) overlayer basis.[3, 4, 30] This has been understood as being a consequence of the lower atomic corrugation of the Ag(111) surface, which results in less preferential binding of the sulphur atoms on the Ag lattice.[3, 4] In other words, the sulphur headgroups bind to the Ag surface in a configuration that favours the maximization of the chain-chain van der Waals interactions, resulting in a close to vertical alkane chain orientation. This turns out to be a $\sqrt{7}$ basis, with sulphur atoms bound to both top and hollow sites of the Ag lattice.[26, 30] However, comparing Table 3-7 and Table 3-8, it can be seen that a perfectly commensurate, basic $\sqrt{7}$ structure on Ag would result in an area per alkane chain smaller than the steric radius of alkanes packed on the surface with no tilt (Table 3-8; $\theta=0$). In order to accommodate a variant of the $\sqrt{7}$ structure favouring close alkane chain packing, the Ag surface is rearranged by the binding of the n-alkanethiol monolayer,[30, 50] producing a packing density in the range of 19-20Å^2/molecule.[4, 30]

Conversely, the atomic corrugation is much higher on the Au surface,[3, 4] resulting in the preferential binding of sulphur atoms at hollow sites, and therefore forcing the monolayer to adopt a $\sqrt{3}$ packing basis. As seen in Table 3-8, the area per alkane chain for a perfectly commensurate overlayer is substantially larger than the steric radius of an alkane chain. As a result, the alkane monolayers on Au adopt a conformation with large (~30°) tilt in order to optimize chain-chain interactions given the constraint of the preferential binding (cf. Table 3-7 and Table 3-8).[3, 4]

Due to the large difference in atomic lattice spacing between Ag and Pt seen in Table 3-7, and the correspondingly different parameters associated with the two basic overlayer packing structures, the similarity observed by RAIRS in the structure of the C18SH monolayers on the two surfaces is at first surprising.

Looking at the area per molecule predicted for the $\sqrt{7}$ basis on Pt, it is obvious that only an extreme rearrangement of the Pt surface — much more so than is seen on the Ag surface — could accommodate such packing for the dense, low defect alkane monolayers observed in this study. As discussed below, the high melting and boiling points of Pt (Table 3-7) make such a Pt surface rearrangement unlikely.

For the basic $\sqrt{3}$ structure on Pt, the area per alkane chain is easily sufficient to allow unresisted packing, while it is clearly too low to allow the high tilt angle of the $\sqrt{3}$ packing on Au (cf. Table 3-7 and Table 3-8). Although based on a completely different overlayer configuration, the value of 20.0Å^2/molecule predicted for $\sqrt{3}$ packing on Pt is close to the 19-20Å^2/molecule for the $\sqrt{7}$ variant observed on the restructured Ag.[30] As observed by Fenter *et al.* (1997),[51] alkane monolayers are capable of accommodating different strains through uniform elastic responses. Noting that the $\sqrt{3}$ and $\sqrt{7}$ overlayer structures on the <111> surface are both roughly hexagonal, it is reasonable to assume that minor strains caused by the overlayer relation to the metal lattice could be accommodated by such elastic responses of the alkane chains, and therefore monolayers with similar packing densities on any <111> surface could demonstrate similar packing structures. Additional constraints — such as the fact that the optimal packing of alkane chains requires the interlocking of protruding CH_2 groups only possible at particular tilt angles[41, 42, 52, 53] — should further increase the similarity of the packing structures at similar packing densities.

Taken in concert with the RAIRS data clearly showing a very similar alkane packing structure on the Pt and Ag surfaces, these arguments cumulatively suggest a $\sqrt{3}$ overlayer structure along with a near vertical alkane chain orientation for the n-alkanethiol monolayers on Pt. A similar conclusion was recently reached by Love *et al.* (2004)[17] for monolayers on <111> palladium, which has a lattice spacing very close to Pt (see Table 3-7); the monolayers on Pd will be discussed in more detail below. For conclusive verification of this hypothesis (for both metals), further studies employing more rigorous techniques such as STM,[19, 41] x-ray diffraction[51, 54] and He diffraction[55] will be necessary.

Metal Malleability and the Influence of Surface Roughness

We now return to the fact that the RAIR spectra for the C18SH monolayer on Ag in Figure 3-10 were obtained from an Ag substrate with very high surface roughness (see Table 3-1). If the preceding discussion comparing the packing on Ag and Pt is valid, this raises the question of why the C18SH monolayer on as-dep Ag does not show the same disorder (and thus appear closer to the RAIR spectra) that is observed for the C18SH monolayer on as-dep Pt?

As noted above, the Ag surface is well known to be reconstructed by the self-assembly process of the n-alkanethiol monolayers.[4, 30, 50] Similar reconstruction resulting in etch-pits is also well documented on Au substrates,[4, 56, 57] and is believed to occur even more prominently on Cu surfaces.[4] For these cases, the binding of the sulphur headgroup to the surface appears to weaken the metal-metal bonds of a single metal atom, providing the metal-atom-S-alkane complex considerable mobility along the surface. This bond weakening would be enhanced for less firmly bound Au or Ag atoms at step edges, and thus providing a mechanism for rearranging the surfaces in a manner that reduces the influence of the roughness of the original bare substrate. Such rearrangement of the Ag surface reasonably accounts for the C18SH spectra on rough Ag substrate in Figure 3-10, though still leaves the question of why similar rearrangement does not occur for the as-dep Pt surface?

Included in Table 3-7 are the melting and boiling points of the various metals, which demonstrate that the Pt-Pt binding energy is significantly higher than the Ag-Ag or Au-Au binding energies. It is reasonable to expect that the binding of sulphur atoms to the Pt surface would not effect the Pt-Pt bonds as significantly as it does for Au or Ag cases, and should therefore result in substantially less mobility of the Pt-S-alkane complex.

The lack of significant rearrangement of the Pt surface explains the different influence of original substrate surface roughness on monolayer structure observed between Pt and Au cases. While the rough Au surface is rearranged during the monolayer self-assembly, the monolayers self-assembled on the Pt surface have to generally 'make do' with the surface as is. As a result, even after the monolayer self-assembly, the Pt surfaces are reasonably described by the models in Figure 3-9, with the original roughness of the rough (as-dep) Pt causing very significant deviations from the ideal monolayer packing observed on flat (TS) Pt. Conversely, the as-dep Au surfaces — though starting with very similar roughness (Table 3-1) and topographic features as the as-dep Pt — will be reconstructed during the self-assembly process to allow a more optimal monolayer packing structure. In this scenario, one would expect the rearrangement of rough Au surfaces would make the kinetics of the self-assembly process slower on rough Au surfaces than on flat, which has indeed been observed previously.[15, 30] In addition, the resultant packing on rough (as-dep) Au would not be expected to be as defect free or as uniform as that observed on flat (TS) Au, which is in good agreement with both the results presented here and those of previous studies.[15, 23, 25]

This analysis suggests platinum's refractory nature plays a strong role in governing the SAM behaviours observed on Pt, and particularly suggests that the mobility of Pt-S-alkane complex should be significantly less than that of the Ag-S-alkane or Au-S-alkane complexes. Planned STM experiments will help to verify this observation by demonstrating conclusively how much, if at all, Pt surfaces are rearranged by the self-assembly of n-alkanethiol monolayers.

Pt and Pd: Similarities and Differences

As Pd is closer in lattice spacing and melting points to Pt than either Ag or Au (see Table 3-7), the recent exploration by Love *et al.*[17] of n-alkanethiol monolayers on Pd surfaces is also considered for comparison. Similar behaviour to that observed on Pt may therefore be anticipated for the monolayers on Pd surfaces, however — recalling the cautionary tale of the differences between the seemingly similar Au and Ag surfaces — no presumptions are made.

Love *et al.*[17] present compelling data and similar arguments to those detailed above for the Pt case, suggesting a $\sqrt{3}$ overlayer structure for the n-alkanethiol monolayers they studied. Figure 12 of their paper directly compares the RAIR spectra of C18SH monolayers on Pd and Ag (equivalent to Figure 3-10 Above, comparing Pt and Ag) which demonstrates the monolayers on the two metals are very similar in structure. Moreover, their monolayers were all formed on as-deposited Pd surfaces with equivalent roughness (Table 3-1) and topographical structure (AFM image in Figure 1 of ref[17]) to the as-dep Pt surfaces used herein. Looking more closely at their Figure 12, the differences between the RAIR spectra of C18SH on their as-dep Pd and Ag are very similar to the differences we observed between the RAIR spectra from C18SH on as-dep Pt and both Ag and TS Pt. These data suggest the behaviour of the long-chain n-alkanethiol SAMs on <111> Pt and Pd surfaces are nearly identical.

However, not all comparisons of the monolayer series on the two surfaces are as similar. In their paper,[17] Love *et al.* present the peak positions for the RAIRS $v_a(CH_2)$ peak as a function of alkane chain-length from n=8 to n=26. When compared with Figure 3-7, the trend observed on the Pd surface mirrors almost identically that displayed in Figure 3-7 (b) for Au. In other words, their RAIRS peak position data as reported for the as-dep Pd surface do not show evidence of a similar shift in the onset chain-length of the 2D-liquid to 2D-solid packing transition due to the surface roughness as is observed in Figure 3-7 (a) for the as-dep Pt surfaces. Noting that the melting and boiling points of Pd are still lower than Pt, this suggests that the Pd-Pd surface bonds may be made weak enough by sulphur binding to cause reasonable surface mobility of the Pd-S-alkane assembly, therefore allowing reconstruction of the Pd surface during the self-assembly process. However, the contact angle data presented by Love *et al.*[17] is suggestive both of some sort of regime transition around $n \approx 14$ and similar defects in the packing of C18SH as are observed on the as-dep Pt surface (significant CH_2 groups exposed at the surface).

While intriguing questions are derived by comparing the data in this study with that presented in Love *et al.* (2004),[17] there is insufficient congruity in the scope of the two studies for any conclusive understanding to be reached. As such, this comparison simply emphasises the need for further experiments on the self-assembly of thiol-based monolayers on both Pt and Pd surfaces.

References

(1) Porter, M. D.; Bright, T. B.; Allara, D. L.; Chidsey, C. E. D. *Journal of the American Chemical Society* **1987**, *109*, 3559-3568.

(2) Laibinis, P. E.; Whitesides, G. M.; Allara, D. L.; Tao, Y. T.; Parikh, A. N.; Nuzzo, R. G. *Journal of the American Chemical Society* **1991**, *113*, 7152-7167.

(3) Ulman, A. *Chem Rev* **1996**, *96*, 1533-1554.

(4) Schreiber, F. *Progress in Surface Science* **2000**, *65*, 151-256.

(5) Schwartz, D. K. *Annual Review of Physical Chemistry* **2001**, *52*, 107-137.

(6) Filler, M. A.; Bent, S. F. *Progress in Surface Science* **2003**, *73*, 1-56.

(7) Smith, R. K.; Lewis, P. A.; Weiss, P. S. *Progress in Surface Science* **2004**, *75*, 1-68.

(8) Bain, C. D.; Troughton, E. B.; Tao, Y. T.; Evall, J.; Whitesides, G. M.; Nuzzo, R. G. *Journal of the American Chemical Society* **1989**, *111*, 321-335.

(9) Peterlinz, K. A.; Georgiadis *Langmuir* **1996**, *12*, 4731.

(10) Ishida, T.; Tsuneda, S.; Nishida, N.; Hara, M.; Sasabe, H.; Knoll, W. *Langmuir* **1997**, *13*, 4638-4643.

(11) Xu, S.; Cruchon-Dupeyrat, S.; Garno, J. C.; Liu, G.-Y.; Jennings, G. K.; Yong, T.-H.; Laibinis, P. E. *Journal of Chemical Physics* **1998**, *108*, 5002.

(12) Dannenberger, O.; Buck, M.; Grunze, M. *Journal of Physical Chemistry B* **1999**, *103*, 2202.

(13) Guo, L.-H.; Facci, J. S.; McLendon, G.; Mosher, R. *Langmuir* **1994**, *10*, 4588-4593.

(14) Yang, Z.; Gonzalez-Cortes, A.; Jourquin, G.; Vire, J.-C.; Kauffmann, J.-M. *Biosensors & Bioelectronics* **1995**, *10*, 789-795.

(15) Terrill, R. H.; Tanzer, T. A.; Bohn, P. W. *Langmuir* **1998**, *14*, 845-854.

(16) Hoogvliet, J. C.; Dijksma, M.; Kamp, B.; van Bennekom, W. P. *Analytical Chemistry* **2000**, *72*, 2016-2021.

(17) Love, J. C.; Wolfe, D. B.; Haasch, R.; Chabinyc, M. L.; Paul, K. E.; Whitesides, G. M.; Nuzzo, R. G. *Journal of the American Chemical Society* **2003**, *125*, 2597-2609.

(18) Camillone III, N. *Langmuir* **2004**, *20*, 1199-1206.

(19) Kawasaki, M.; Sato, T.; Tanaka, T.; Takao, K. *Langmuir* **2000**, *16*, 1719-1728.

(20) Touzov, I.; Gorman, C. B. *Journal of Physical Chemistry B* **1997**, *101*, 5263-5276.

(21) Wong, S.-S.; Porter, M. D. *Journal of Electroanalytical Chemistry* **2000**, *485*, 135-143.

(22) Losic, D.; Gooding, J. J.; Shapter, J. G.; Hibbert, D. B.; Short, K. *Electroanalysis* **2001**, *13*, 1385-1393.

(23) Leopold, M. C.; Black, J. A.; Bowden, E. F. *Langmuir* **2002**, *18*, 978-980.

(24) Leopold, M. C.; Bowden, E. F. *Langmuir* **2002**, *18*, 2239-2245.

(25) Yang, J.; Han, J.; Isaacson, K.; Kwok, D. Y. *Langmuir* **2003**, *19*, 9231-9238.

(26) Sellers, H.; Ulman, A.; Shnidman, Y.; Eilers, J. E. *Journal of the American Chemical Society* **1993**, *115*, 9389-9401.

(27) Li, Z.; Chang, S.-C.; Williams, R. S. *Langmuir* **2003**, *19*, 6744-6749.

(28) For any sample where thickness calculations based on single angle measurements showed large distributions, additional angles between 60 and 80 degrees were measured and incorporated into the calculations to reduce the uncertainty in the reported values.

(29) The ellipsometry data for the SAM series on the as-dep Pt surfaces demonstrates a unphysically large zero-chain length intercept of 0.62nm. A similarly large and unphysical intercept of 0.51nm is observed for the SAM series on as-dep Au. Conversely, the data series on both TS surfaces demonstrate physically realistic intercept values of 0.12nm (TS Au) and 0.19nm (TS Pt). The large offset for the as-dep surfaces are the result of the greater roughness of these surfaces.

(30) Kawasaki, M.; Nagayama, H. *Surface Science* **2004**, *549*, 237-245.

(31) Poirier, G. E.; Tarlov, M. J.; Rushmeier, H. E. *Langmuir* **1994**, *10*, 3383-3386.

(32) The n-alkanethiol monolayer series on Au substrates did not go to sufficiently short chain lengths to substantively observe the short chain regime trend on Au.

(33) This transition was not observed by ellipsometry as the monolayer series on the TS Pt did not include a sufficient number of short chain lengths (n<6) to observe a substantivel trend deviating from that of the longer chains (n>8).

(34) Debe, M. K. *Journal of Applied Physics* **1984**, *55*, 3354-3366.

(35) Allara, D. L.; Nuzzo, R. G. *Langmuir* **1985**, *1*, 52-66.

(36) Nuzzo, R. G.; Dubois, L. H.; Allara, D. L. *Journal of the American Chemical Society* **1990**, *112*, 558-569.

(37) Parikh, A. N.; Allara, D. L. *Journal of Chemical Physics* **1992**, *96*, 927-945.

(38) Allara, D. L.; Swalen, J. D. *Journal of Physical Chemistry* **1982**, *86*, 2700-2704.

(39) As the RAIRS peak at ~2849 wavenumbers becomes very weak (near the noise threshold) for shorter chain lengths and the RATIO method used herein relies on this peak to calculate the tilt, the error in the tilt angle estimation rapidly increases with decreasing chain length. The error becomes so large for shorter chain lengths (N<12) as to eliminate any confidence in the approximation.

(40) The RAIR spectra of the bulk solid and liquid were repectively measured in this study using C18SH in a KBr pellet at room tempurature and neat C8SH.

(41) Barrena, E.; Ocal, C.; Salmeron, M. *Journal of Chemical Physics* **2001**, *114*, 4210-4214.

(42) Barrena, E.; Palacious-Lidon, E.; Munuera, C.; Torrelles, X.; Ferrer, S.; Jonas, U.; Salmeron, M.; Ocal, C. *Journal of the American Chemical Society* **2004**, *126*, 385-395.

(43) Kwok, D. Y.; Lin, R.; Mui, M.; Neumann, A. W. *Colloids and Surfaces* **1996**, *116*, 63.

(44) Kwok, D. Y.; Leung, A.; Lam, C. N. C.; Wu, R.; Neumann, A. W. *Colloid and Polymer Science* **1998**, *1998*, 459.

(45) Kwok, D. Y.; Leung, A.; Lam, C. N. C.; Lin, A.; Wu, R.; Neumann, A. W. *Journal of Colloid and Interface Science* **1998**, *206*.

(46) Li, Z.; Beck, P.; Ohlberg, D. A. A.; Stewart, D. R.; Williams, R. S. *Surface Science* **2003**, *529*, 410-418.

(47) Blackstock, J. J.; Li, Z.; Freeman, M. R.; Stewart, D. R. *Surface Science* **2003**, *546*, 87-96.

(48) Ragan, R.; Ohlberg, D.; Williams, R. S.; Blackstock, J. J.; Kim, S. *Journal of Physical Chemistry B* **2004**, *Submitted.*

(49) It is recognized that defects and grain boundaries in the monolayer are more likely to occur in coincidence with the Pt step edges, and that molecules at such sites along these steps could experience greater orientational freedom (not depicted in Figure 9). However, based on the low defect density suggested by the data in this study we believe that defects are not the dominant feature at the single atomic layer step edges and that on average the packing density remains relatively undisrupted.

(50) Dhirani, A.; Hines, M. A.; Fisher, A. J.; Ismail, O.; Guyot-Sionnest, P. *Langmuir* **1995**, *11*, 2609.

(51) Fenter, P.; Eberhardt, A.; Liang, K. S.; Eisenberger, P. *Journal of Chemical Physics* **1997**, *106*, 1600-1608.

(52) Karaborni, S.; Toxvaerd, S. *Journal of Chemical Physics* **1992**, *97*, 5876-5883.

(53) Barrena, E.; Kopta, S.; Ogletree, D. F.; Charuch, D. H.; Salmeron, M. *Physical Review Letters* **1999**, *82*, 2880-2883.

(54) Fenter, P.; Eberhardt, A.; Eisenberger, P. *Science* **1994**, *266*, 1216-1218.

(55) Camillone III, N.; Chidsey, C. E. D.; Liu, G.-Y.; Scoles, J. *Journal of Chemical Physics* **1993**, *98*, 3503.

(56) McCarley, R. L.; Dunaway, D. J.; Willicut, R. J. *Langmuir* **1993**, *9*, 2775-2777.

(57) Sondag-Huethorst, J. A. M.; Schonenberger, C.; Fokkink, L. G. J. *Journal of Physical Chemistry* **1994**, *98*, 6826-6834.

Chapter 4: Plasma Produced Ultra-thin Pt-oxide Surfaces

4.0 Introduction

Metal-oxides possess a wide array of physical, chemical and electrical properties that are ideal for exploitation in such technologies as electronics, chemical and photo sensors, optical devices and catalysts. For electronic applications, metal-oxides can span the entire range from fully metallic to highly insulating, even for different stoichiometric oxides of the same metal. The ability to prepare ultra-thin films (5Å→100Å) of metal-oxides, with well defined and potentially tuneable properties, could make this class of material surfaces particularly useful for nanoscale and molecular electronics.

As discussed in the thesis Introduction, platinum is a metal of particular interest, due to its compatibility with conventional silicon electronics. Previous literature[2-8] demonstrates that the range of platinum-oxides stable in ambient conditions (PtO_x for $x<\sim2.1$) cover a particularly appealing range of electrical properties. These oxides shift from being metallic at low oxygen ratios ($x<1$), to semi-metallic or semi-conducting in the mid-range (roughly $1\leq x<2$), and to semi-conducting/insulating near the oxygen saturation level of the stable oxides ($2\leq x<\sim2.1$).[2, 3, 5-8] In addition, these Pt-oxides could be good electrode materials for molecular electronic devices, as isocyanides can be selectively self-assembled on their surfaces.[4] Given these properties, the ability to fabricate ultra-thin PtO_x films would provide substantial opportunities for the use of platinum oxides as active electronic materials.

To date, the experiments on the physical and electrical properties of platinum oxides have been conducted on bulk fabricated samples on insulating substrates that were produced by reactive evaporation or sputtering in the presence of oxygen.[2, 3, 5-9] Despite the use of similar procedures for producing ultra-thin films of other metal oxides on conducting substrates,[10] attempts to fabricate thin PtO_x films on metallic gold or platinum using reactive deposition have been unsuccessful[7] — only metallic Pt was observed to form overtop the underlying metallic substrate. This behaviour was attributed to the <111> surface texture of the underlying metal epitaxially driving the spontaneous formation of Pt metal,[7] and is indicative of the Pt-oxides having a relatively lower stability than other metal oxides; an observation supported by the low thermal decomposition temperatures (500-650°C) of the oxides into Pt metal.[5, 8] In order to utilize the reactive deposition of PtO_x for electronics device fabrication, a suitable conductive substrate material would need to be found and the growth parameters of PtO_x on this substrate determined. Such studies are time-consuming and can generate secondary problems with material compatibility.

An alternative method of generating platinum oxide using an oxygen (O_2) plasma treatment of metallic platinum has been previously demonstrated in literature,[4, 11] however, the characterization of the resultant PtO_x surfaces has, thus far, been very limited. One major advantage of this technique is that the PtO_x forms as an ultra-thin film on the surface of any metallic Pt exposed to the O_2 plasma, immediately producing the sought after PtO_x-on-metal structure.

In order to capitalize on the advantages of this O_2 plasma Pt oxidization technique, a detailed understanding of the properties of the resultant oxide structure is required. This technique is different from the conventional reactive deposition processes — illustrated by the formation of PtO_x on metallic Pt — and the relation of the plasma-produced Pt-oxide to those Pt-oxides commonly studied in the literature has not been established. For reactively deposited PtO_x, large changes in the electrical properties of the oxide have been associated with changes from amorphous to crystalline oxide structure, [6, 8] and even with very small changes in the stoichiometry of amorphous oxides.[7] As such, a detailed understanding of the physical and chemical structural properties of plasma produced platinum oxides is essential for the development of these materials for electronic or other technological applications.

In Section 4.1, a detailed experimental characterization of the formation, and physical and chemical properties of O_2 plasma produced Pt-oxide, is presented. Electrical resistance measurements of micron-wide ultra-thin metallic Pt wires, collected as a function of plasma exposure time, demonstrate a monotonic consumption of metallic Pt by the O_2 plasma for the treatment time range examined. Conversely, the AR-XPS shows the thickness of the produced PtO_x surface layer to be constant over the same time regime. In conjunction, these data reveal that the O_2 plasma treatment results in a rapid initial formation of oxide on the bare Pt surface, followed by a long-time steady-state equilibrium between the processes of continuous surface etching and oxide formation. AR-XPS data also demonstrate that the platinum oxide is comprised of two distinct platinum-oxygen compounds, which reside respectively in the 'bulk' and at the exposed surface of the ultra-thin oxide overlayer.

Section 4.2 turns to examine the electrical properties of the ultra-thin Pt-oxide, using both ambient condition conductive-AFM (cAFM) and STM. To ensure that the collected SPM data accurately reflected the electrical properties of the ultra-thin Pt oxide, and was not convoluted with the topography of the underlying Pt surface, this series of experiments makes use of ultra-flat TS Pt surfaces, prepared as described in Chapter 2 (subsection 2.1.1). The cAFM results demonstrate that the ultra-thin Pt-oxide layers do display semi-conducting electrical characteristics. Furthermore, the STM data reveal nanoscale inhomogeneities laterally in the oxide structure, and both the cAFM and STM data reveal irreversible electrical switching of the oxide layer's electrical properties under various conditions.

4.1 Physical Characterization

All oxygen plasma treatments were conducted in a reactive ion etching chamber (RIE® model 1700 system). The base pressure was lowered to ≤10mTorr before beginning the constant flow of O_2 gas into the chamber. Once the O_2 pressure in the chamber was stabilized, the plasma was ignited and run at a set power level for a specific length of time. The O_2 plasma conditions (100mTorr and 100W) were selected directly from Li *et al.*(2003).[11] Three plasma exposure times (1, 5 and 15 minutes) were employed using these specific conditions in order to gain an understanding of the platinum oxide formation process.

4.1.1 Ultra-thin Pt Wire Electrical Resistance Measurements

Figure 4-1 shows a schematic (left) of the combined optical lithography and shadow angle evaporation patterning process used to produce micron-wide ultra-thin metallic platinum wires employed in this study, as well as optical images (right) of the resultant dumbbell film patterns. The 100μm squares at either end of each dumbbell were used as electrical contact pads for measuring the resistance of the wires in between. As is visible in the optical micrograph, a range of wire widths between 1μm and 10μm were fabricated while the wire length was held constant at 550μm.

Optical patterning and development of the photoresist (Figure 4-1 – step (a)) was carried out on prime polished Si<100> substrates with a 200nm capping SiO_2 layer. Four thicknesses of metallic Pt between 25Å and 130Å were sputter deposited (Figure 4-1 – step (b)) after a brief argon back-sputtering of the substrate to remove any remaining photoresist on the bottom of the patterned features. Along with the patterned substrates, unpatterned Si<100> wafers were also coated in the same sputtering runs. These blanket samples were used to precisely calibrate the thickness of these sputtering depositions with ellipsometric thickness measurements using a Gaertner ellipsometer (Gaertner Scientific Corporation, Skokie, Il) operating at three wavelength (543.5nm, 632.8nm and 832.2nm). This same instrument was used to determine the optical constants of

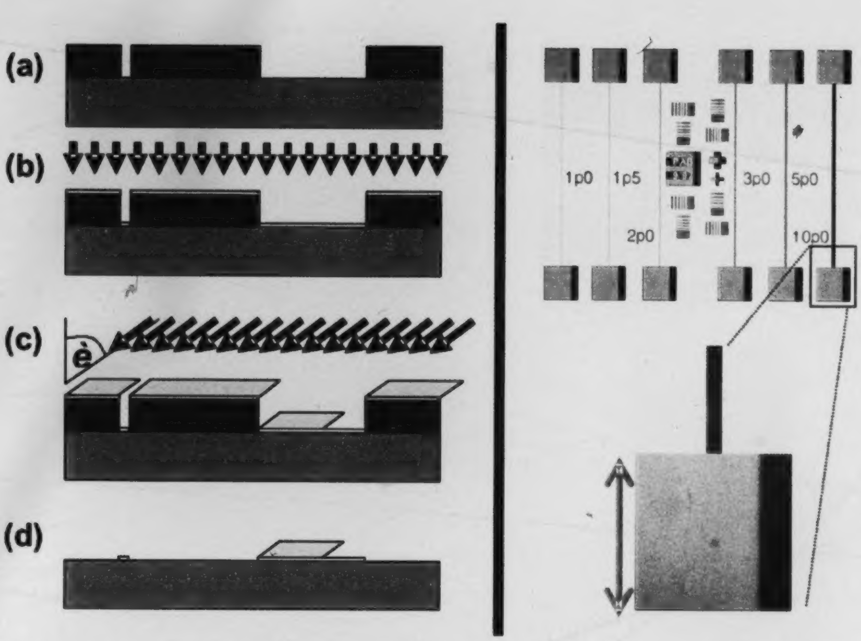

Figure 4-1 ***Left*** – Schematic illustration of the photo-lithography and shadow angle evaporation methods used to produce ultra-thin metallic Pt wires with thick electrical contact pads (see text for details). ***Right*** – Optical micrographs of the produced wire dumbbell patterns, with the micron wide ultra-thin Pt wires running between two thicker (100μm)^2 electrical contact pads. The numbers in the patterns beside the wires represent the nominal thickness of the wires.

the Pt films from thick (≥1000Å) Pt films prepared using the same sputtering chamber and conditions. The measured thicknesses of the four Pt film depositions and the corresponding ultra-thin Pt wire samples are presented in Table 4-1.

Measurement Technique	**Thickness 1**	**Thickness 2**	**Thickness 3**	**Thickness 4**
Ellipsometric Thickness*	26.5Å ±0.9Å	45.4Å ±0.5Å	62.6Å ±0.8Å	121.0Å ±0.4Å
Thickness from listed Resistances and Figure 4-2 Curve	25.3Å ±0.4Å (33.1±1.1kΩ)	46.9Å ±0.2Å (9.62±0.08kΩ)	62.7Å ±0.3Å (6.13±0.04kΩ)	118.2Å ±0.7Å (2.65±0.02kΩ)

*Measured for blanket ultra-thin Pt films

Table 4-1 Ellipsometry measured and resistively measured thicknesses (along with resistances) of the four thicknesses of the sputter deposited ultra-thin metallic Pt wires.

The photolithographically patterned substrates with the ultra-thin sputtered Pt films were subsequently loaded into an e-beam evaporation chamber and aligned with the substrate surface normal at an angle (θ) of 87° with respect to the highly directional evaporant flux, at which point a further 500Å of Pt was deposited (Figure 4-1 – step (c)). The high angle of incident flux with respect to the surface normal combined with the thickness of the photoresist (T~0.78μm) results in the additional Pt being deposited only into features in the photoresist that are wider than $T\times\tan(\theta)$, which in this case was >15μm. As such, with proper alignment of the patterned substrate on the angled mount, the 100μm contact pads were mostly coated with the thick evaporated Pt while even the 10μm wires remain entirely uncoated. Once the photoresist was lifted off (Figure 4-1 – step (d)), the final dumbbell patterns thus consisted of thick electrical contact pads (with one shadowed edge) and the ultra-thin Pt wires connecting them, as seen in the right panel of Figure 4-1.

This shadow angle evaporation thickening of the contact pads was used in order to ensure: (1) that the O_2 plasma did not significantly reduce the thickness of the contact pads and thus the microprobes used to make electrical contact to the wires could be pushed through the ultra-thin oxide, ensuring good metallic contact to the Pt underneath; and (2) that wherever the microprobes touched the electrical contact pad, the measured resistance was dominated by the wire and the contact pads made only a negligible contribution.

The electrical resistances of the ultra-thin Pt wires were then measured for the freshly deposited wires, and after various exposure times to the O_2 plasma treatment conditions described above (100mTorr and 100W). For each sample, the current-voltage (IV) curves of the wires were measured between a range of ±1.0V (and ±10.0V for at least one wire on every sample) and none of the wires examined demonstrated any non-linear IV behaviour. The experimental resistance of each wire measured was calculated from the slope of these IV curves. For simplicity, 5μm wide wires were used for all resistance measurements reported herein — measurements of different wire widths (between 1μm and 10μm) for several samples demonstrated the expected linear dependence of resistance on wire width. The average 5μm wire resistance for each sample was determined from the average of at least 4 different wires and the reported errors are the standard deviations of the measurements.

Relating the resistance of these ultra-thin Pt wires to their thickness is considerably more complex than with thick bulk films, primarily because of the influence of electron surface scattering effects. Zhang and Butler (1995)[1] employed semi-classical theory to calculate the ratio of ultra-thin film resistivity to that of the bulk metal (ρ_{film}/ρ_{bulk}), specifically for the case of metallic platinum. Their non-analytical calculations, presented in their paper as a function of film thickness (down to 10Å), demonstrate excellent agreement with previous experimental observations. Figure 4-2 plots the ρ_{film}/ρ_{bulk} curve Zhang and Butler determined for Pt (Figure 4 of ref[1]); the curve in Figure 4-2 has been converted to be in terms of the experimentally measured resistance of the 5μm wide wires, and normalized to the resistivity of thick Pt wire samples (1200Å, determined by profilometry) prepared using the same photolithographic patterning and sputtering conditions as for the ultra-thin Pt wire samples. For the complete calculations and theory, readers are referred to the publication of Zhang and Butler.[1]

In addition to the normalizing data point, four entirely independent data points are also shown in Figure 4-2. These four points represent the experimentally measured ellipsometric thicknesses and average wire resistances (both listed in Table 4-1) of the four freshly deposited ultra-thin Pt wire samples. As highlighted by the inset in Figure 4-2, these four independent data points show exceptional agreement with the normalized curve. In the reverse direction, the simple analytical expression describing the curve in Figure 4-2 can also be used to calculate a wire thickness from the measured wire resistances. These values are included in Table 4-1 (along with the experimental resistances), demonstrating equally excellent agreement with the ellipsometric measurement of the Pt thickness. Based on this agreement, this method of calculating ultra-thin Pt wire thicknesses was adopted directly from the experimentally measured wire resistances for analyzing the data from the Pt wire samples exposed to O_2 (and Ar) plasma treatments.

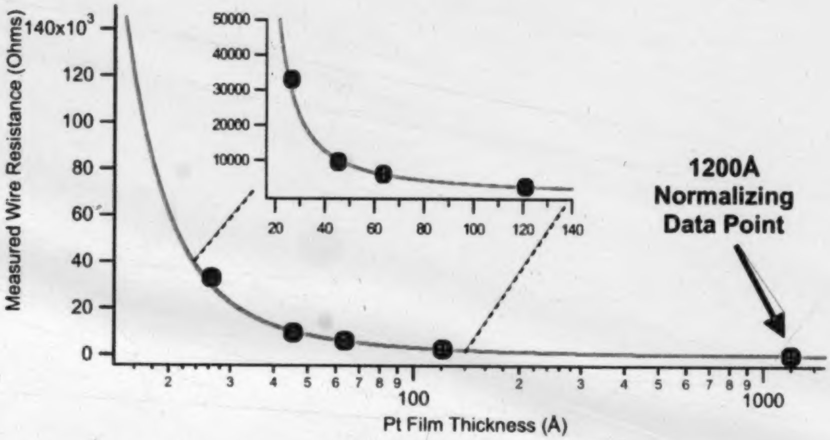

Figure 4-2 Plot of the ρ_{film}/ρ_{bulk} curve from Zhang and Butler (1995)[1] normalized to relate the resistant of the 5μm wide and 550μm long wires to the thickness of the ultra-thin metallic Pt comprising the wires. Also shown in the plot is the normalizing 1200Å data point and four independent data points based on the ellipsometric thickness and measured resistances presented in Table 4-1 for the sputter deposited ultra-thin metallic Pt wires.

Identical samples of all four thicknesses were also exposed to O_2 plasma treatment (100mTorr and 100W) for various lengths of time, and the *IV* curves of the treated wires were subsequently measured. Using the simple analytical expression for the curve in Figure 4-2, the wire resistances were converted to Pt wire thicknesses, which are plotted in Figure 4-3 (a).

These data demonstrate that the rate of decrease of the wire thicknesses is similar for all four cases. To better illustrate this, Figure 4-3 (b) re-plots the same data in terms of the change in resistively measured wire thickness. This plot demonstrates that the decrease in resistive thickness for all the wires as a function of O_2 plasma exposure time is identical to within experimental error. The only data point that deviates significantly from this general trend is that for the initially thinnest wires (Thickness 1; cf. Table 4-1) in the case of the 15min O_2 plasma, though it is important to note that after a 15min O_2 plasma treatment these initially thinnest wires showed infinite resistance (no conductivity). For this sample, all of the metallic Pt from the original wire had been consumed, and the oxidization process had terminated, prior to the end of the O_2 plasma treatment.[12] It was initially hypothesized that this would leave entirely oxidized Pt wires for

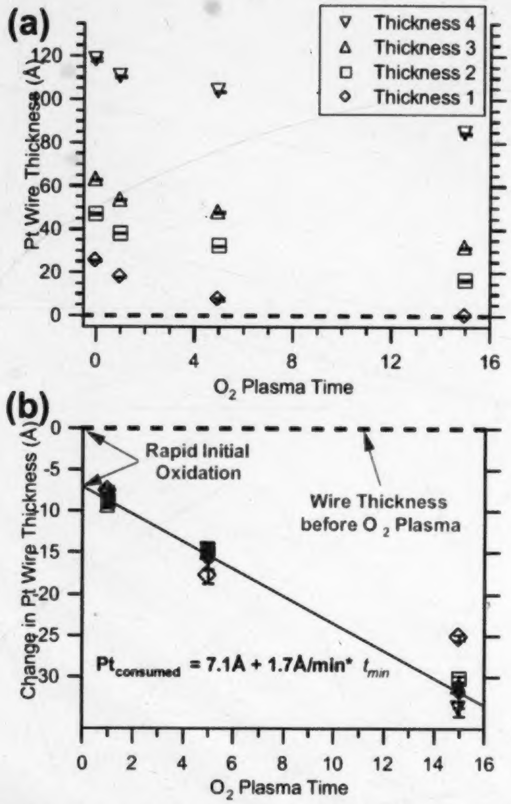

Figure 4-3 (a) Resistive wire thicknesses measured as a function of O_2 plasma treatment period for wires with the four initial thicknesses listed in Table 4-1. **(b)** Same data as in (a), re-plotted in terms of the decrease in wire thickness as a function of O_2 plasma treatment period. The equation of the linear fit to the data is included in the graph.

electrical testing, however even the PtO_x was removed by this length of O_2 plasma treatment.

Figure 4-4 depicts the basic model of metallic platinum to platinum oxide conversion for an ultra-thin Pt wire (or the top of the a thicker Pt film) via O_2 plasma treatment. The formation of PtO_x by the oxygen plasma must consume a corresponding amount of Pt from the metallic portion of the wire. At the same time, the density of the PtO_x must be lower than that of the platinum due to the incorporation of oxygen — in other words, the average volume per platinum atom must increase. Assuming no loss of platinum atoms during this oxide formation process, the conversion of metallic Pt to PtO_x by oxygen plasma must result in an

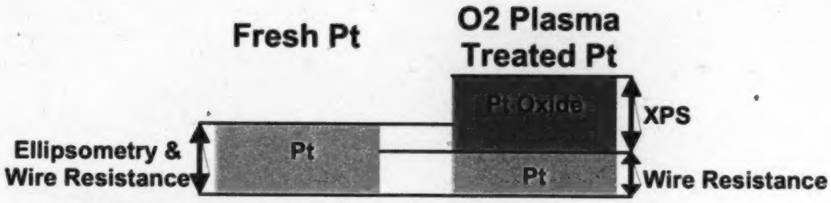

Figure 4-4 Basic model assumed for the formation of platinum oxide on a fresh Pt surface via O_2 plasma treatment. Listed in along side the vertically segmented regions of the model are the experimental techniques employed to characterize the thickness of each segment.

expansion of the Pt at the film surface. Due to the physical constraints of the film, this swelling can only occur vertically. Table 4-2 lists approximate densities for oxides with stoichiometric values of x=1 and x=2, along with calculated swelling ratios based on these densities.

Oxide Stoichiometry	Density Kg/m^3	Swelling Ratio Based on the ratio of volume per Pt atom: PtO_x/Pt
Pt	21,090	--
PtO	14,100	~1.62
PtO_2	11,800	~2.09

*Values in this table are based on PtO_x densities of crystalline oxides. The density of amorphous oxides will similar stoichiometries could still differ substantially from these values.

Table 4-2 Densities for two potential stoichiometries of platinum oxide from literature are listed, along with the calculated swelling ratios anticipated for the conversion of Pt→PtO_x (see text for details).

As indicated in Figure 4-4, it is expected the electrical resistance of the oxidized Pt wires to be related only to the thickness of the remaining metallic Pt In other words, the plasma produced PtO_x is assumed to be at least two orders of magnitude more electrically resistive than the metallic Pt. Since the PtO_x layer for each O_2 plasma treatment time should be identical for all wires, any notable contribution of the PtO_x layer to the conductivity of the wires will also be more significant as the initial Pt wire thickness decreased.[13] This would result in a variation of the observed electrical resistance (and thus the observed resistive thickness trend) with initial wire thickness.

Figure 4-3 (b) clearly shows the electrical resistance behaviour of the wires to be independent of the initial wire thickness (with the exception explained in the previous paragraph), verifying the expectation that any contributions of the plasma produced platinum oxide to the wires' electrical conduction are negligible. This result is corroborated the XPS data presented below, demonstrating an oxide stoichiometric ratio for the ultra-thin PtO_x layer of $x >> 1$ along with the studies of reactively sputtered PtO_x that demonstrate oxides in this range exhibit electrical properties ranging from semi-metallic to insulating.[2, 3, 5-8]

With this basis for interpretation, the analysis turns to the physical interpretation of the trend itself. As illustrated in Figure 4-3 (b), the reduction in resistive wire thickness as a function of O_2 plasma time for all initial wire thicknesses is well described by a linear slope with a non-zero intercept. This behaviour indicates the existence of two distinct time regimes in the consumption of Pt by the O_2 plasma: (1) the initial rapid oxidization of the fresh Pt surface, represented in the data by the consistent non-zero intercept of ~7.1Å; and (2) the monotonic steady-state that occurs once the PtO_x layer is well established, represented by the linear slope of ~1.7Å/min. While the rapid initial oxidization process is relatively unremarkable (and apparently complete on a time frame shorter than 1min), the monotonicity of the steady-state regime was unexpected.

For a kinetic oxide growth model, based only on the conversion of Pt→PtOx and resulting in the constant thickening of the PtOx with time, the rate of metallic Pt consumption would be expected to demonstrate a rapid (roughly exponential) decrease with time, associated with the gradual increase in difficulty of the reactive O_2 plasma accessing the metallic Pt atoms underlying the surface oxide. The monotonicity of the steady-state regime observed in Figure 4-3 (b) rather indicates that a second — non-diffusive process — governs the rate of metallic Pt consumption by the O_2 plasma treatment. This issue is returned to in subsection 4.1.4, in conjunction with the results of the XPS analysis presented in the following subsection.

4.1.2 X-ray Photoelectron Spectroscopy

Unpatterned metallic platinum films, 1000Å thick, were prepared using the same sputter-deposition technique as the ultra-thin Pt wires examined above. These samples were subject to the same range of O_2 (and Ar) plasma treatments as the ultra-thin Pt films and were then transported to the XPS facility for a series of AR-XPS measurements. XPS measurements were conducted at the *Alberta Center for Surface Engineering and Science* (ACSES) on an Axis-165 X-ray photoelectron spectrometer (Kratos Analytical, Manchester, UK) using five different electron takeoff angles ranging uniformly from 0° to 60° relative to the surface normal.

Oxide Thickness

The X-ray photoelectron spectroscopy (XPS) characterization of the plasma produced platinum oxide on the ~1000Å Pt films focused on the regions of the platinum 4f and oxygen 1s electrons.[14] Thicker films were chosen over the ultra-thin Pt for XPS studies in order to prevent any signal from the underlying silicon oxide substrate from complicating the analysis of the oxygen 1s peak region.[15] Figure 4-5 shows the XP spectra taken at 5 different electron takeoff angles between 0° and 60° (measured from the substrate normal) for both an untreated (bare) Pt surface (a,b) and a Pt surface treated with the O_2 plasma for 5 minutes (c,d). Similar spectra to those in Figure 4-5 (c) and (d) were also obtained for samples treated with the O_2 plasma for 1 and 15 minutes.

Qualitative comparison of the spectra from the two samples in Figure 4-5 evidences the appearance of new Pt(4f) and O(1s) peaks after the O_2 plasma treatment. Quantitative fitting of the range of spectra actually reveals that at least two new peaks emerge in each region.[16] Figure 4-6 shows an example of the quantitative fitting analysis for one pair of Pt(4f) and O(1s) spectra. For the Pt(4f) region, a minimum of 3 doublet peaks are required in order to reasonably fit the data. By comparison, the spectra for the bare Pt surface demonstrates only the metallic Pt(4f) doublet peak (cf. Figure 4-5). In the case of the O(1s) region, the bare Pt sample has only a background oxygen signal from adventitious oxygen in physisorbed molecules (cf. Figure 4-5). Accounting for this background signal in

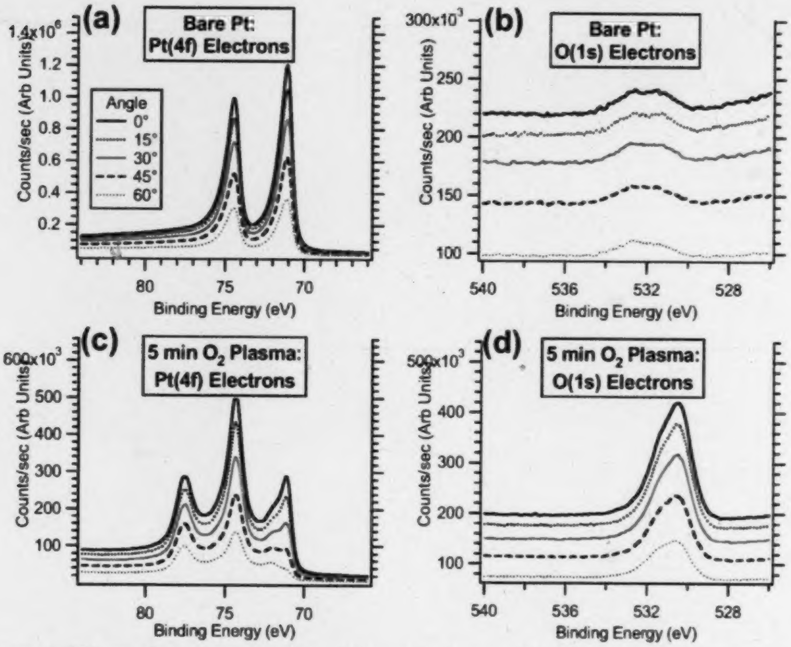

Figure 4-5 X-ray photoelectron spectra taken at 5 electron takeoff angles between 0° and 60° for both **(a & b)** an fresh/untreated Pt and **(c & d)** Pt treated with O_2 plasma for 5 minutes.

the analysis of the O1s regime of the plasma-treat samples[17] still leads to a minimum of two singlet peaks being required in order to reasonably fit the data.

Precise assignment of the peaks, labelled 1 to 4 in Figure 4-6, to particular chemical states of the Pt and O atoms is made in the following subsection. At present, these peaks are grouped together as being from the PtO_x overlayer formed on the O_2 plasma-treat Pt surfaces. This general assignment allows the thickness of the whole PtO_x overlayer to be calculated in several ways from the set of AR-XP spectra.

A simple overlayer-substrate model was employed for the purposes of this analysis. The model presumes that there exists a well-defined, sharp (step function) interface between the overlayer and the substrate, as is suggested by the physical model in Figure 4-4. Based on this model, the metallic Pt(4f) peak intensity should be attenuated by a factor of $e^{-d/(\lambda \cos\theta)}$ on the O_2 plasma-treated samples relative to the bare Pt sample (d-oxide thickness; λ-electron attenuation length in the oxide for electrons at the kinetic energy associated with the peak; θ-

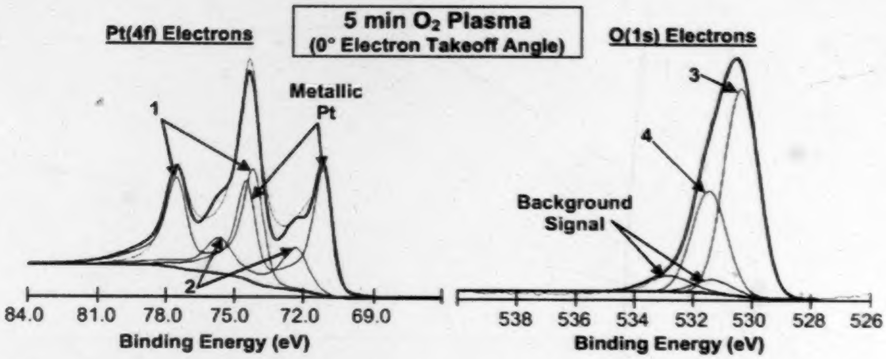

Figure 4-6 An example of the quantitative data fitting carried out for the XP spectra. The metallic Pt(4f) and background O(1s) peaks are clearly labelled, along with the four new peaks that emerge in the XP spectra as a result of O_2 plasma treatment (labelled 1→4).

electron takeoff angle). Values for the d/λ ratio were therefore calculated from the normalized intensity ratio of the metallic Pt(4f) peak in the O_2 plasma-treated spectra to the bare Pt(4f) peak obtained at the same electron takeoff angle $\left(\frac{d}{\lambda} = -\ln\left[\frac{Pt(4f)_{O_2}}{Pt(4f)_{Bare}}\right]\times Cos(\theta)\right)$. Included in Table 4-3 are the average d/λ ratios for the three O_2 plasma treatment times. These were obtained by averaging the ratios calculated for each of the five examined electron takeoff angles (the quoted errors are the standard deviation of the five values).

Oxide Property	1 min O_2 Plasma	5 min O_2 Plasma	15 min O_2 Plasma
d/λ ratio	1.23 ±0.07	1.25 ±0.1	1.25 ±0.07
Thickness (d) with $\lambda \approx$ 20Å	~24.6Å	~25.0Å	~25.1Å

Table 4-3 The average d/λ ratios calculated from the attenuation of the metallic Pt(4f) XPS signal on O_2 plasma-treat samples along with the corresponding Pt-oxide layer thicknesses calculated using the electron attenuation length value of $\lambda \approx 20$Å estimated using the empirical approximation formula of Tanuma *et al.* (1994)[18] and software from NIST.[19]

One of the advantages of this simple model is that the calculated d/λ ratio is entirely independent of the oxide properties. Extracting an oxide thickness from this ratio, however, still required the determination of the electron attenuation length (λ) in the oxide at the kinetic energy associated with the Pt(4f) peak. To obtain a reasonable estimate of this attenuation length, the empirical approximation formula of Tanuma *et al.* (1994),[18] built into the *Electron Effective Attenuation Length Database* software from the US National Institute of Standards and Technology (NIST),[19] was employed. These calculations required input estimates of both the stoichiometry and density of the platinum oxide; estimates were provided on the basis of the analysis in the next subsection. An approximate value for the attenuation length was calculated to be $\lambda \approx 20$Å, though the uncertainty surrounding this value is large (estimated at ~15%). Table 4-3 also includes the thickness values corresponding to the listed d/λ ratios and an attenuation length of $\lambda \approx 20$Å for Pt(4f) electrons in the PtO_x layer.

To verify the thickness results calculated solely from the metallic Pt(4f) signal, the *Angle Resolved Concentration-depth Profile* software (*ARtick*) provided by the UK National Physical Laboratory[20] was used to calculate PtO_x thicknesses based on the intensities of both the Pt(4f) and O(1s) signals from within the oxide, and their variations with electron takeoff angle. From the start, these calculations required stoichiometry and density estimates for the oxide and provided only a single average d/λ ratio for each sample. However, these calculations also employed independent portions of the collected XPS spectra and, for the case of the O(1s) oxide signals, required the electron attenuation value at a different electron kinetic energy (also calculated from the NIST electronic database). The thicknesses from these calculations are listed in Table 4-4, demonstrating excellent agreement between the independent Pt(4f) and O(1s) values and with the values listed in Table 4-4 from the simple overlayer-substrate model.

Oxide XPS Peaks Used in Calculation	**1 min O_2 Plasma**	**5 min O_2 Plasma**	**15 min O_2 Plasma**
Pt(4f)	**~23.6Å**	**~25.4Å**	**~25.7Å**
O(1s)	**~24.3Å**	**~25.5Å**	**~25.1Å**

Table 4-4 Pt-oxide layer thickness calculated respectively from the takeoff angle dependence of the oxide Pt(4f) and O(1s) XPS signal intensities using the *ARtick* software for the UK National Physical Laboratory.[20]

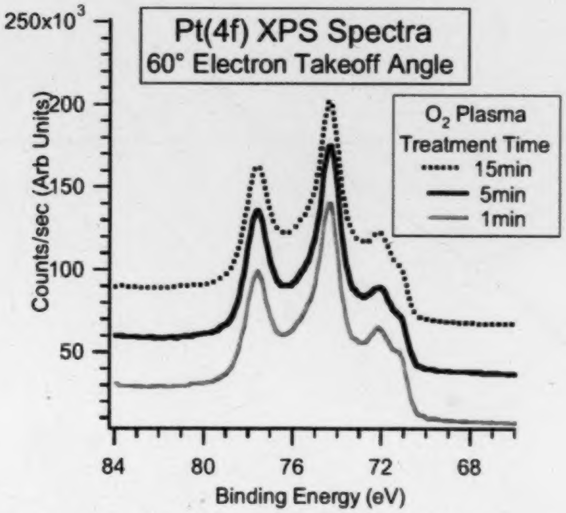

Figure 4-7 XP spectra of the Pt(4f) taken at a takeoff angle of 60° region for the 1min, 5min and 15min O_2 plasma-treat samples.

The most notable feature of the thicknesses presented in Table 4-3 and Table 4-4 is that they are *independent* of O_2 plasma treatment time – the d/λ ratios listed in Table 4-3 for all three O_2 plasma treatment times are identical to within the error of the experimental measurements. This result initially appears contrary to the earlier finding with the ultra-thin wire measurements that metallic Pt is steadily being consumed throughout the O_2 plasma treatment. Nonetheless, Figure 4-7 shows that the XP spectra of samples treated for the three different O_2 plasma treatment periods (taken at the same electron takeoff angle) are virtually indistinguishable, which verifies that plasma produced PtO_x surface layers are nearly identical. This is in line with expectations for an oxide growth model in which the oxide growth rate decreases rapidly (roughly exponentially) with O_2 plasma exposure time (equating to oxide thickness), though with an time decay constant (τ) much shorter than the time frames explored in this study (τ<<1min).[21] This observation is returned to in subsection 4.1.4, along with the results of the resistive wire measurements.

Oxide Chemical and Physical Properties

Having established that the plasma produced ultra-thin PtO_x surface layers are identical across the range of O_2 plasma treatment times examined, our attention

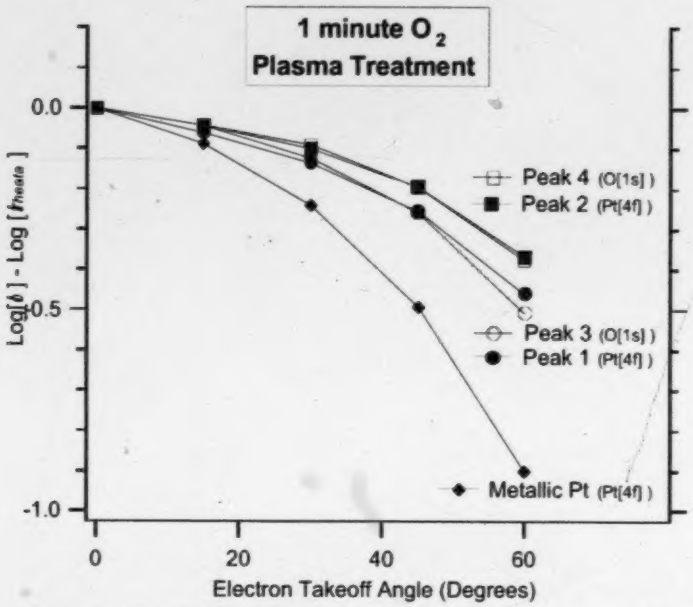

Figure 4-8 Plots the $\log_{10}[I_0]$- $\log_{10}[I_\theta]$ versus electron takeoff angle for all the XPS peaks observed on the 1min O_2 plasma-treat sample; I_0 is the peak intensity at a 0° takeoff angle and I_θ is the peak intensity at takeoff angle θ.

shifts to consider the question of chemical and physical structure of the Pt-oxide itself. To address this question, our focus returns to the quantitative data fitting of the XPS spectra presented in Figure 4-5 and Figure 4-6. The presence of at least two new Pt(4f) and O(1s) peaks resulting from the O_2 plasma treatment indicates that at least two different chemical species (stoichiometries) of platinum-oxide are present in the PtO_x surface layer.

Based on literature[6, 8, 9] and database[22] values, Peak 1 at 74.1eV in the Pt(4f) electron region[23] are assigned to PtO_2 — no other stable platinum oxide species demonstrates such a prominent shift from the metallic Pt(4f) peak at 71.2eV.[9, 22] The position of Peak 2 at 71.3eV is very close to the reported values for PtO.[9, 22] Confident assignment to a particular platinum-oxygen compound, however, is complicated because several stable platinum-hydroxide species ($Pt(OH)_y$) also demonstrate peak positions in this range.[22] In addition, platinum oxide with an intermediate oxidation state between PtO and PtO_2 (labelled as $PtO_{1+(z<1)}$) has also been observed to have a peak position nearly identical to both PtO and Peak 2.[9]

The assignment of Peak 2 to a particular platinum-oxygen compound is thus deferred to later in this analysis.

In order to associate the two Pt(4f) platinum-oxide peaks with the corresponding oxygen peak in the O(1s) region of the XP spectra (Peaks 3 and 4 in Figure 4-6), the intensity trend of each peak was examined as a function of electron takeoff angle. Pt(4f) and O(1s) peaks that correspond to the same chemical species are expected to demonstrate a very similar dependence of peak intensity on electron takeoff angle due to their identical locations in the platinum oxide surface layer. Figure 4-8 plots the $\log_{10}[I_0]$- $\log_{10}[I_\theta]$ for each of the Pt(4f) and O(1s) peaks as a function of electron takeoff angle (I_0 is the peak intensity at a 0° takeoff angle and I_θ is the peak intensity at takeoff angle θ). The correlations of Peak 1 with Peak 3 and Peak 2 with Peak 4 are clearly distinguishable in the figure. In other words, Peak 3 at 530.4eV in the O(1s) XP spectra region is associated with the PtO_2 oxide stoichiometry along with the Pt(4f) 74.1eV peak (Peak 1) while Peak 4 at 531.5eV is correlated with the ambiguous Pt(4f) 71.3eV peak (Peak 2). Table 4-5 summarizes the peak positions and chemical species assignments for the four O_2 plasma generated XP spectra peaks shown in Figure 4-6.

Atomic Species and Photoelectron	Peak Designation (cf. Figure 4-6)	Peak Position (±0.1eV)	Experimental O:Pt Ratios from XPS	Experimental Composition of Oxide	Chemical Species Assignment
Pt(4f)*	**Peak 1**	**74.1 eV**	**1.97** **±0.13**	**~70%**	**PtO_2**
O(1s)	**Peak 3**	**530.4 eV**			
Pt(4f)*	**Peak 2**	**71.3 eV**	**1.79** **±0.13**	**~30%**	**$Pt(OH)_z$// PtO**
O(1s)	**Peak 4**	**531.5 eV**			

*Pt(4f) peak positions are quoted for the P4(4f-7/2) peak. The doublet separation between the 4f-7/2 and 4f-5/2 peaks was taken to be constant at 3.35eV for all Pt chemical states.

Table 4-5 Peak position and chemical species assignments for the four oxide XPS peaks, along with the experimental O:Pt ratio calculated using corresponding O(1s) and Pt(4f) peaks, and the experimental oxide composition calculated from all four oxide peaks.

With the Pt(4f) and O(1s) platinum oxide peaks appropriately paired, the atomic ratio of oxygen to platinum (O:Pt) for both chemical species of platinum oxide present in the PtO_x surface layer can be calculated from the experimental

XPS data. Using the XPS atomic sensitivity factors for the oxygen and platinum atoms to relate the intensities of the two sets of peaks,[24] the O:Pt ratio for both oxide species was calculated for all five electron takeoff angles examined for each sample. These values were averaged to produce the O:Pt ratios presented in Table 4-5; the quoted error is the standard deviation of all the individually calculated values from the three samples treated with different O_2 plasma times. No notable variation of the ratios with O_2 plasma treatment time was observed, in agreement with the earlier observations.

As indicated in Table 4-5, the average O:Pt ratio determined from the intensity ratio of Peaks 1 and 3 is in good agreement with the earlier assignment of these peaks to PtO_2 based on peak position. Similarly, the O:Pt ratio calculated from the ratio of Peaks 2 and 4 validates the earlier hesitancy to assign these peaks to a particular chemical species. The observed O:Pt ratio of ~1.8 indicates that this chemical component of the oxide is not associated with only PtO. Possible explanations include a uniform $PtO_{1+(z\leq 1)}$ composition as reported previously by Hecq *et al.*[9] or a mixture of $Pt(OH)_y$ and PtO.[25] Before further considering this assignment, one other oxide feature revealed by the plot in Figure 4-8 is examined.

Examining the metallic Pt(4f) peak in Figure 4-8, it is observed that the falloff of peak intensity with increasing electron takeoff angle is stronger than for any of the oxide peaks. This is simply a graphical illustration of the metallic Pt peak signal being attenuated by the ultra-thin oxide overlayer (exploited in the previous subsection to calculate the thickness of the oxide) and, as such, is not particularly revealing. What is revealing in Figure 4-8, however, is the fact that the two oxide components display very distinct angular dependencies. Though the intensity of neither oxide component deceases as fast with angle as the metallic Pt peak, Peaks 1 and 3 assigned to PtO_2 show a much more significant fall off with angle than Peaks 2 and 4. This demonstrates that the PtO_2 signal is more strongly attenuated with angle, indicating that the signal is coming (on average) from deeper within the oxide layer. Phrased another way, these different angular dependencies (used to correlate the O(1s) and Pt(4f) peaks) demonstrate that the ultra-thin platinum film is not a homogenous mixture of the two oxide components identified by XPS. The oxide film structure rather appears to be roughly segregated into sub-layers, with the PtO_2 component being on average deeper in the oxide, next to the underlying metallic Pt, and with the other chemically ambiguous oxide component residing at the surface.

In order to quantify the stratification of the oxide, a simple two sub-layer model was taken as a first order approximation of the oxide structure. This model assumes the two oxide components to be entirely segregated into separate sub-layers, with the ambiguous component layer at the surface and the PtO_2 layer underneath. The simplicity of this model allows a thickness to be calculated for the surface (ambiguous) oxide component layer using the same techniques employed above for calculating the total oxide thickness. Using these techniques, the average thickness for this ambiguous component surface sub-layer of the oxide was calculated to be ~4.7Å.[26] Taking an average total oxide thickness from Table 4-3 and Table 4-4 of ~24.9Å, this implies the PtO_2 should make up roughly ~80% of the oxide component.

The oxide composition independently calculated from the areas of Peaks 1 thru 4 in all the recorded XPS spectra (fitted as shown in Figure 4-6) is also provided in Table 4-5, revealing an oxide composition of ~70% PtO_2.[27] This is roughly in agreement with the prediction of the two sub-layer model for the oxide structure, suggesting the model is a reasonable first order approximation of the ultra-thin oxide film structure. Intermixing of oxide components at the boundary between the two sub-layers and surface roughness of the Pt substrate are the most likely origins of the observed minor deviation. Shown in Figure 4-9 is a schematic illustration of the stratified oxide structure including all the structural details of the ultra-thin oxide film revealed by the AR-XPS data.

Returning finally to consider the chemical species assignment of the ambiguous oxide surface component, it is noted that, in a recent separate experiment,[28] densely packed monolayers of trichlorosilane molecules were successfully self-assembled on the O_2 plasma-treated platinum surfaces. The self-assembly of these molecules on a surface is known to require a high density of

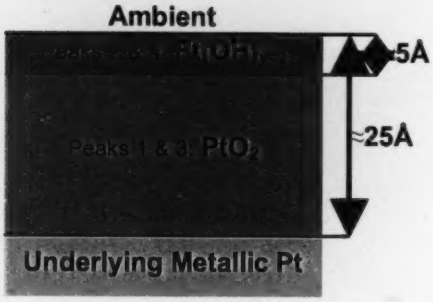

Figure 4-9 Stratified ultra-thin oxide layer structure based on the analysis of the AR-XPS data.

hydroxyl (–OH) terminal groups on the surface,[29-31] indicating that the exposed surface of the ultra-thin platinum oxide layer is most likely densely covered with $Pt(OH)_y$. Combined with the understanding of the oxide stratification illustrated by Figure 4-9, Peaks 2 and 4 of the oxide XP spectra (cf. Figure 4-6 and Table 4-5) are assigned primarily to $Pt(OH)_y$. This hydroxide surface is expected to be formed on the freshly O_2 plasma-treat Pt surfaces upon exposure to ambient conditions (likely associated with the catalytic breakdown of water molecules).

The O:Pt ratio in Table 4-5 suggests a stoichiometry for the $Pt(OH)_y$ oxide surface of $y \approx 1.8$. However, PtO defects in the underlying PtO_2 will also contribute to Peaks 2 and 4; such defects are known to be present even in the most rigorously prepared reactively sputtered PtO_2 films.[6, 8, 9] A reasonable estimation would be that Peaks 2 and 4 are due to a surface layer stoichiometry of $Pt(OH)_{y \approx 2}$, along with a small concentration of PtO defects through the PtO_2 bulk of the ultra-thin oxide layer.

4.1.3 Argon Plasma Treatment

Using the same resistivity measurement technique described above, it was determined that the 1min Ar plasma treatment (40mTorr and 15W) of the fresh ultra-thin Pt wires decreased the thickness of the wires by 0.4Å (±0.1Å). XPS demonstrates that the Ar plasma did not change the surface chemistry of the Pt. Instead, the Ar plasma continuously physically etches the Pt surface at a constant rate of roughly ~0.4Å/sec.

On the other hand, the Ar plasma treatment of a previously O_2 plasma-treated Pt surface reveals substantial changes in surface chemistry. As previously reported,[11] the Ar plasma completely reduces the ultra-thin platinum oxide overlayer, removing any obvious traces of the oxide's previous existence, even for the very low power Ar plasma and short exposure time employed in this study. XPS of Pt samples treated with O_2 plasma followed by Ar plasma appear identical to freshly prepared metallic Pt films. This rapid decomposition of the platinum oxide surface layer by the Ar plasma demonstrates the low stability of the oxide relative to the metallic Pt state.

Resistive thicknesses were also determined for the ultra-thin Pt wires which had undergone O_2 plasma followed by Ar plasma, in order to determine whether the Pt atoms from the oxide were reconstituted onto the underlying metallic Pt or whether they were etched away from the surface. The results demonstrated that the resistive wire thicknesses of the O_2 plasma-treat ultra-thin wires increased on average by 6Å (±1Å) after the Ar plasma treatment (independent of the original O_2 plasma treatment time), indicating that at least some of the Pt atoms from the oxide overlayer return to being part of the underlying metallic Pt surface.

4.1.4 Oxide Formation Kinetics

The AR-XPS measurements in subsection 4.1.2 demonstrate the overlayer Pt-oxide thickness to be roughly time-independent for the range of O_2 plasma treatment times examined (cf. Table 4-3 and Table 4-4). This is indicative of the rate of platinum oxide formation being initially very high, though decreasing rapidly (~exponentially) as the oxide thickens and the reactive atoms of O_2 plasma have increasingly greater difficulty reaching the metallic Pt atoms underlying the oxide layer. Based on this model alone, it could be anticipated that the rate of metallic Pt consumption should decrease to negligible levels on a similar time scale — ie. much shorter than the time frames explored in this study. However, the resistive thickness measurements in subsection 4.1.1 demonstrate that metallic Pt is being continuously consumed throughout the plasma treatment process (cf. Figure 4-3). In addition, the resistive thickness measurements reveal that the rate of Pt consumption is monotonic over the range of oxide O_2 plasma treatment times examined in this study. This monotonic time dependency is discordant with a kinetic model based solely on the diffusion formation of platinum oxide.

The reconciliation of these two observations is to include a slow etching of the Pt-oxide surface by the O_2 plasma in the kinetic model along with the rapid oxide formation process. This slow etching process would thus be the rate limiting step for the consumption of the underlying metallic Pt. Indeed, the constant metallic Pt consumption rate of ~1.7Å/min observed in Figure 4-3 is of the same order of magnitude as the ~0.4Å/min etch rate of the fresh Pt ultra-thin wires observed for the Ar plasma treatment. The etching rate of the O_2 plasma is expected to be higher than that of the Ar plasma due to the greater reactivity, the higher power of the plasma treatment conditions and the lower thermal stability of platinum oxides relative to metallic platinum.

The ~7.1Å intercept of the Pt consumption curve in Figure 4-3 was also associated with the initial rapid formation of platinum oxide. Presuming this to be roughly the amount of metallic Pt incorporated into the oxide overlayer, this value is compared to the estimated oxide thickness from the XPS data (cf. Table 4-3 and Table 4-4). Calculating the ratio of consumed metallic Pt thickness (~7.1Å) to produced oxide thickness (~24.9Å) in this manner yields an average estimate for the swelling ratio of ~3.5. This is larger than the swelling ratio of 2.09, predicted in Table 4-2 from the literature values for the density of PtO_2, however the density listed in the table is for crystalline PtO_2 (and PtO). The highly invasive and non-equilibrium process of platinum oxide formation by O_2 plasma treatment is highly unlikely to be conducive to the formation of a crystalline oxide layer. Which is more likely is that the 'bulk' PtO_2 component of the oxide is amorphous and very similar to the amorphous PtO_2 films produced by reactive sputtering.[2, 3, 5-7] Based on the roughly estimated swelling ratio, the density of the ultra-thin Pt-oxide layers is approximated to be around ~7000kg/m^3 ≈ {2.09/3.5} × 11,800kg/m^3.[32]

4.2 Electrical Characterization

The cAFM and STM experiments presented below were conducted on samples of freshly stripped TS Pt, prepared as described in Chapter 2 (subsection 2.1.1), treated with an O_2 plasma (100mTorr and 100W) immediately before SPM examination using a Dimension 3100 microscope (Digital Instruments). Identical behaviour was observed with the SPM techniques employed in this section for TS Pt surfaces exposed to 1min, 5min and 15min plasma treatments. Freshly stripped TS Pt samples without O_2 plasma treatment were also examined as a reference for comparison. For the cAFM experiments, gold-coated silicon-nitride cantilevers (0.35 N/m; radius of curvature ≤50nm; μMasch) were employed, and platinum-iridium tips (Digital Instruments) were used for the STM experiments. All SPM experiments were conducted in ambient laboratory conditions. The convention adopted for the reporting of all voltages in this subsection (and this thesis) is to report the bias of the SPM tip relative to a grounded substrate.

cAFM Results

To begin the cAFM experiments, freshly stripped metallic TS Pt samples were examined using the Au coated cantilevers to confirm that good metallic contact between the tip and substrate could be formed under the ambient conditions of the AFM laboratory. Initial experiments demonstrated that scanning the bare Pt surfaces in contact mode with the Au coated cantilevers, even with contact forces of ≤5nN, rapidly wore away the Au coating and left the tips non-conducting. As a result, current-voltage (*IV*) curves were recorded on all samples by lowering fresh Au-coated tips vertical onto randomly selected positions on the surface with the horizontal position of the tip frozen.[33] The *IV* curve shown in Figure 4-10 demonstrates the good metallic contact routinely achieved to the freshly stripped metallic TS Pt surfaces; the contact resistance between the tip and sample was routinely in the range of 1-5kΩ. The exact contact resistance varies from tip to tip, and was also noted to systematically increase with the wearing down of the tip after extended electrical cycling.

Similarly obtained *IV* curves from samples of freshly stripped TS Pt treated with O_2 plasma immediately before examination revealed different behaviour.

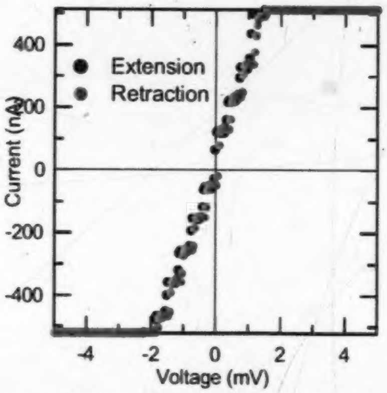

Figure 4-10 A current-voltage (*IV*) curve recorded by cAFM on freshly stripped metallic TS Pt. The 'extension' trace was recorded on the –ve→+ve voltage sweep and the 'retraction' trace was recorded on the retuning +ve→-ve voltage sweep.

Shown in Figure 4-11 are averaged[34] *IV* curves taken at different locations on a 5min O_2 plasma treated TS Pt sample using the same Au coated tip, but after varying amounts of tip-wear. The non-linear and non-metallic *IV* curves reveal a low-conductance, bandgap-like region between ~±0.6V, followed by high conductance region at higher biases in both directions. This *IV* behaviour is consistent with a model of the ultra-thin PtO_2 layer as a semiconductor with a band gap in the range of ~1.2eV, in excellent agreement with the literature observations of the bulk reactively-sputtered PtO2 having a bandgap in the range of 1.2 to 1.5eV.[2, 5] The roughly symmetric nature of the *IV* curve suggests that the Fermi level of the metallic leads in the non-biased case is located roughly in the middle of the PtO_2 bandgap.

Quantitative interpretation of the *IV* curves is made difficult by the lack of knowledge regarding the precise tip geometry and radius of curvature of the cAFM probe. As stated above, the three *IV* curves in Figure 4-11 were obtained using the same Au coated cAFM tip after increasing amounts of tip usage/wear. As the tip is repeatedly used for *IV* measurements, the contact area of the Au tip appears to decrease until the point where electrical contact breaks altogether. This is to be due to both the gradual frictional wearing of the tip and the electromigration of the Au away from the apex of the cAFM tip during electrical cycling. Between Figure 4-11 (a) and (c), the low-voltage current drops by a

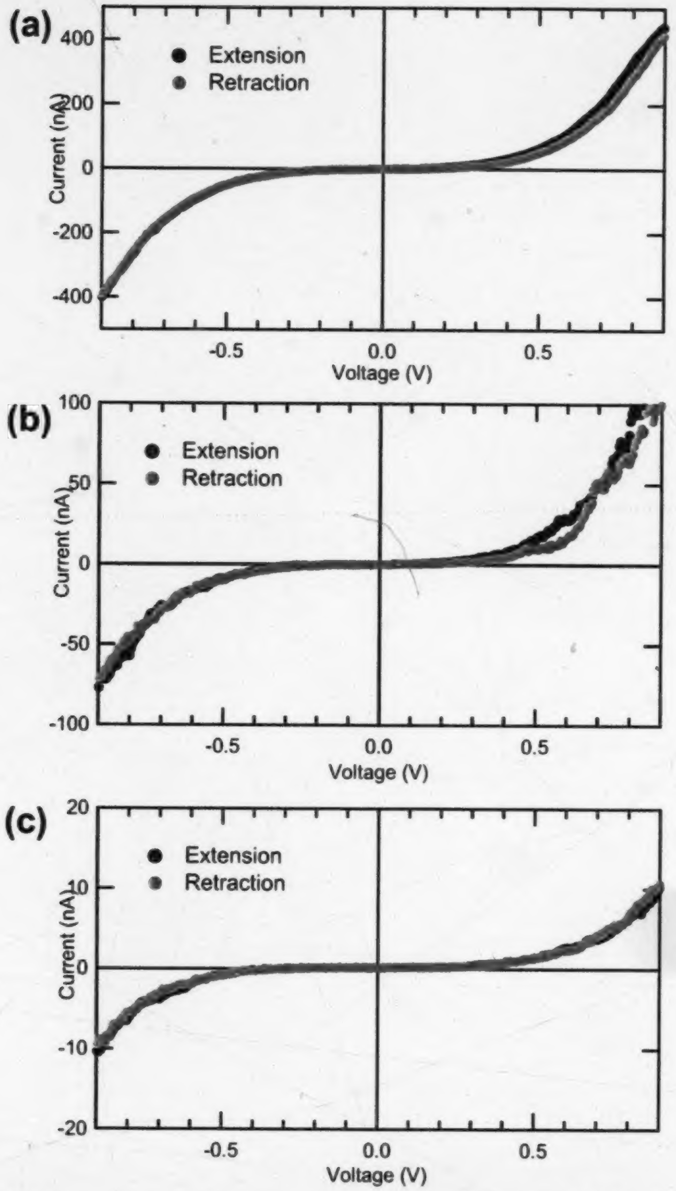

Figure 4-11 Three averaged *IV* curves taken on TS Pt surfaces immediately after a 5min O_2 plasma treatment, taken after varying amounts of tip-wear (a=no-wear thru c=max-wear). The applied contact forces were varied between 3 and 20nN with no observable influence on the *IV* curves.

factor of ~10 while the high-voltage current drops by a factor of ~40. These are associated with resistances in the range of ~0.1-1.0GΩ and ~2-90MΩ at 0V and

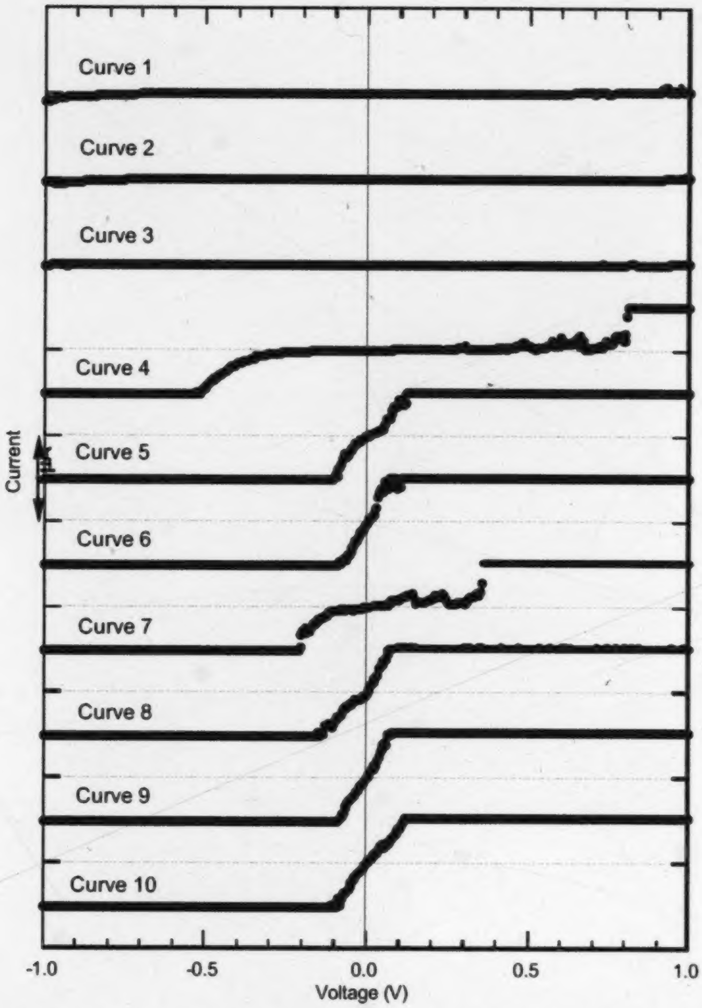

Figure 4-12 Series of successively captured *IV* curves, taken at the same location on a 5min O_2 plasma treated sample with a force of 20nN. The curves were taken at a rate of 1Hz without any delay between successive *IV* curves. The flat lines on the extremes of *IV* curves for curves 4-10 is caused by the saturation of the current pre-amplifier.

±0.9V respectively. Without reasonable estimates of the contact areas of the cAFM tip for the different measurements, even order of magnitude current density estimates are, at best, speculative.

Another important qualitative feature of the observed electrical behaviour for the O_2 plasma treated TS Pt surfaces was the observed breakdown of the oxide layer under specific conditions. Figure 4-12 provides a series of successive individual *IV* curves between ± 1.0V, showing the evolution of the *IV* curves as a function of the number of bias cycles. For the first 3 bias cycles, the *IV* curves show qualitatively identical behaviour to that observed Figure 4-11. However, between curves 3 and 4, the oxide appears to undergo an irreversible breakdown. Over the next several bias cycles, the *IV* curves evolves noisily towards high current, linear *IV* traces. This general behaviour was observed with several samples and cAFM tips, consistently showing rapid transitions from the behaviour shown in Figure 4-12 to linear behaviour.

The breakdown trigger voltage is estimated from the range of observed breakdown events to be between $|0.6 \rightarrow 1.2|$V; as indicated by the absolute value notation, a dependence on bias direction could not be deduced from the limited range of cAFM experiments conducted. Occasionally, breakdown was observed to occur even after numerous (30+) bias cycles of a similar bias range had already been collected at the same location. This could be due to a combination of local inhomogeneities in the Pt-oxide layer and tip drift gradually shifting the cAFM tip to a different location on the surface.

Attempts were made to look for inhomogeneities in the Pt-oxide layer by using cAFM to create current maps of the O_2 plasma treated surfaces at constant voltage. The cAFM tip was scanned along the surface in contact mode while the current was monitored at a range of bias values and applied forces. For all bias values and forces, as low as 10mV and ~3nN, shortly after the scan began the current was observed to rapidly (almost instantly upon tip motion) increase to metallic levels. This was true even at locations already observed to have *IV* curves similar to those in Figure 4-11. After imaging the surface, *IV* scans taken within the imaged region revealed only metallic *IV* behaviour, similar to that observed in Figure 4-10. Though a previous study[7] has shown bulk reactively-sputtered, crystalline α-PtO_2 to be a relatively hard material, the ultra-thin plasma produced PtO_2 (most likely amorphous) layer could be substantially softer; the scanning cAFM tip could be scratching away the oxide layer. Equivalently, the scanning tip could be finding local defects in the oxide at locations such as grain boundaries between underlying Pt crystallites. These defects could be the initiation site of the local breakdown of the oxide. Once the oxide breakdown has begun locally, it could be propagated by the tip along the surface. In either case, exploring the lateral homogeneity of the Pt-oxide ultra-thin film using cAFM was unsuccessful, and STM was turned to as an alternative.

STM Results

Ambient-condition STM imaging of the freshly stripped metallic TS Pt surface was conducted over a wide range of bias and tunnel current settings. Results of such imaging were presented previously in Chapter 2. For the STM imaging of the 5min O_2 plasma treated TS Pt surfaces, a problem with tip-crashing arose with the typical low-voltage (≤20mV), high current (≥1nA) imaging conditions used on the metallic TS Pt surfaces. Higher voltage (≥100mV) and lower current (≤0.2nA) scanning conditions were required in order to avoid tip-crashing. All imaging was conducted at slow scan rates of ≤4Hz/line.

Shown in Figure 4-13 are two sets of STM images (50pA, ±250mV) of a 5min O_2 plasma treated TS Pt surface. In these images, the surface appears inhomogeneous, with nanoscale variations in current (right hand images) across clearly visible. Looking at the current images of Figure 4-13, a pattern underlying the current variations is evident, with domains in the range of ~10-30nm of constant current surrounded by spots of higher current fluctuations (higher current appears darker in the current image of Figure 4-13 (a) and lighter in the current image of Figure 4-13 (b); this is caused by the bias inversion between the imaging conditions). This pattern and size scale is consistent with the grain size of the TS Pt underlying the plasma produced oxide layer. The inhomogeneous appearance of the surface at these imaging conditions could be related to variation in the oxide structure or thickness, or else, it could simply be due to topographical variations of the surface which are accentuated at the grain boundaries. At the scanning conditions employed (50pA, ±250mV) the images of the surface were stable over an indefinite number of repeat scans.

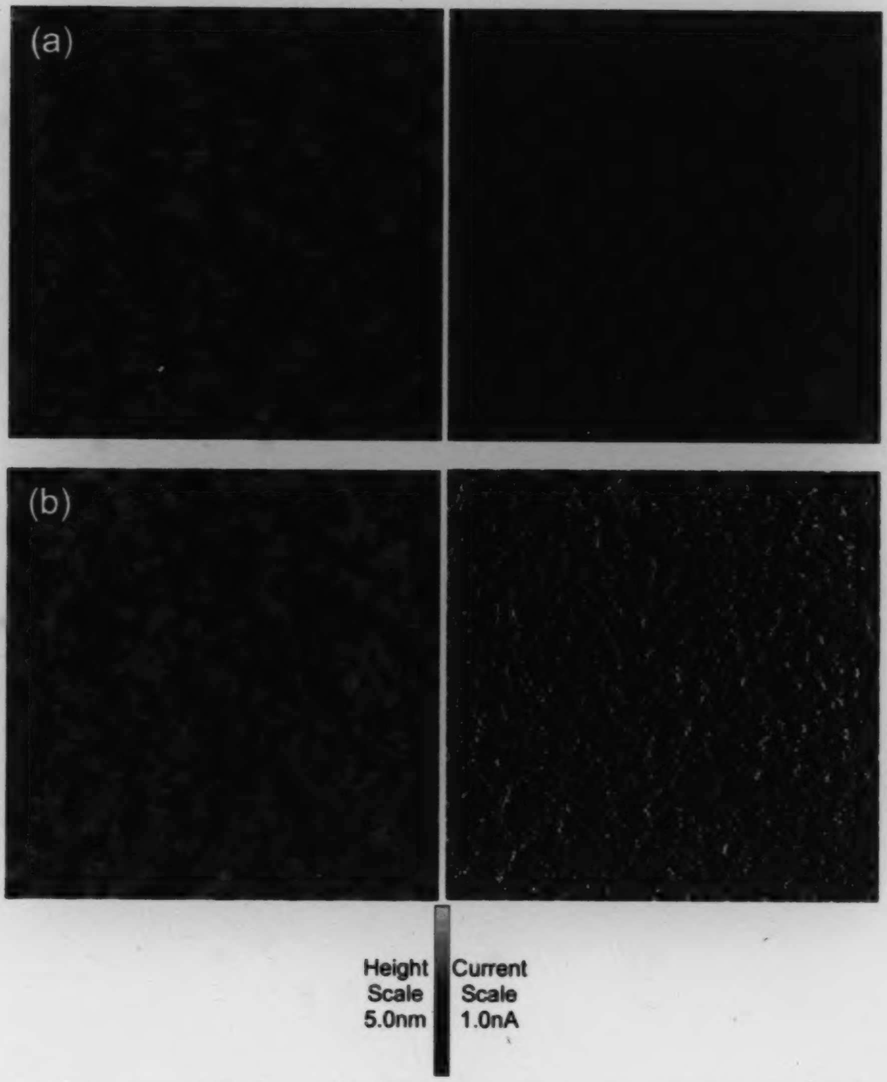

Figure 4-13 Two sets of $(500\text{nm})^2$ ambient condition topography (left) and current (right) STM images of freshly stripped TS Pt surfaces treated with a 5min O_2 plasma immediately before imaging. The images were taken in constant current mode with slow feedback settings, a current of 50pA and tip voltage relative to the grounded sample of **(a)** -250mV and **(b)** +250mV.

A wide range of other scanning conditions were also explored; for each set of conditions, a new location on the same sample was used. For most of the scanning conditions studied (-500mV≤V≤+300mV; I≤200pA) the images recorded were the same as seen in Figure 4-13 and were stable over an indefinite number of repeat scans. However, once the tip bias was raised above +400mV, the surface began to show dramatic changes in response to the STM imaging. Shown in Figure 4-14 are three successive STM images (topography: left; current: right), taken at a setting of 500mV and 100pA, demonstrating the evolution of the surface as a result of continuous STM imaging at these conditions.

Observable in the evolution of the current (right hand) images of Figure 4-14 (a) through (c) is the growth in width and intensity of inhomogeneous high current spots with continuous imaging. Reversal of the tip-sample bias (or even lowering of the bias to ≤+300mV) resulted in the alteration of the surface stopping, however, no scanning conditions explored were found under which the changes could be reversed. As the higher voltage and lower current of these surface-altering scanning conditions equates to a larger tip-surface separation than for the previous, non-surface-altering scanning conditions, these irreversible changes cannot be attributed to the physical crashing of the tip into variations of surface topography. Rather, these data imply the initial high current inhomogeneities observed in the oxide are likely defects/variations in the structure or thickness of the Pt-oxide layer, which then act as initiation sites for the irreversible oxide breakdown observed to occur with successive scanning at a higher positive voltage.

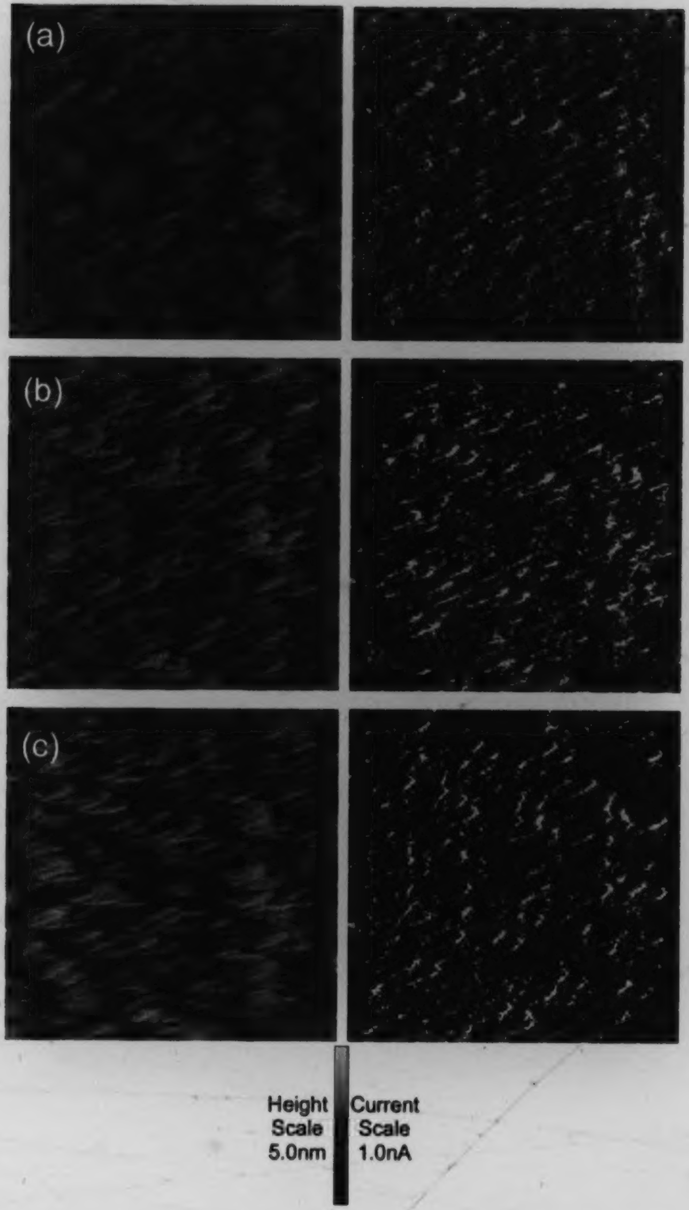

Figure 4-14 Three sets of successive $(500nm)^2$ ambient condition topography (left) and current (right) STM images of freshly stripped TS Pt surfaces treated with a 5min O_2 plasma immediately before imaging. The images were taken in constant current mode with slow feedback settings, a current of 100pA and tip voltage relative to the grounded sample of +500mV.

The voltage-onset of the surface-alteration suggests the changes occurring are electrochemical in nature, possibly related to the reduction of the PtO_2 to PtO or Pt. The original high current spots observed in Figure 4-14 (a) are likely concentrations of defect sites or thinner regions of the PtO_2 where higher currents can initially flow. These higher currents could in turn allow the easier reduction of the surrounding PtO_2 once the voltage is raised to sufficient levels for the chemical reduction to take place, by allowing more current to pass. As any stresses in the oxide leading to cracking or the incorporation of defects during the oxide formation could easily be accentuated at the grain boundaries of the underlying Pt, the appearance of the high current sites in patterns consistent with the grain boundaries of the underlying TS Pt surface is also reasonable.

Based on these STM results, the oxide breakdown observed by cAFM and discussed above is likely driven by the same mechanism, seemingly electrochemical in nature. These results indicate that the physical and chemical model of the oxide presented in Section 4.1 must be expanded to incorporate the lateral nanoscale structure of the oxide layer. Particularly when considering applications of the plasma produced Pt-oxide layer in nanoelectronic devices, the STM data reveal the lateral nanoscale structure plays a crucial role in the mechanisms of electrical conduction through, and electrical breakdown or switching of, the ultra-thin Pt-oxide layer.

References

(1) Zhang, X.-G.; Butler, W. H. *Physical Review B* **1995**, *51*, 10085-10103.

(2) Aita, C. R. *Journal of Applied Physics* **1985**, *58*, 3169-3173.

(3) McBride, J. R.; Graham, G. W.; Peters, C. R.; Weber, W. H. *Journal of Applied Physics* **1991**, *69*, 1596-1604.

(4) Hickman, J. J.; Laibinis, P. E.; Auerbach, D. I.; Zou, C.; Gardner, T. J.; Whitesides, G. M.; Wrighton, M. S. *Langmuir* **1992**, *8*, 357-359.

(5) Neff, H.; Henkel, S.; Hartmannsgruber, E.; Steinbeiss, E.; Michalke, W.; Steenbeck, K.; Schmidt, H. G. *Journal of Applied Physics* **1996**, *79*, 7672-7675.

(6) Abe, Y.; Yanagisawa, H.; Sasaki, K. *Japanese Journal of Applied Physics* **1998**, *37*, 4482-4486.

(7) Maya, L.; Riester, L.; Thundat, T.; Yust, C. S. *Journal of Applied Physics* **1998**, *84*, 6382-6386.

(8) Abe, Y.; Kawamura, M.; Sasaki, K. *Japanese Journal of Applied Physics* **1999**, *38*, 2092-2096.

(9) Hecq, M.; Hecq, A.; Delrue, J. P.; Robert, T. *Journal of Less-Common Metals* **1979**, *64*, 25-37.

(10) Street, S. C.; Xu, C.; Goodman, D. W. *Annual Review of Physical Chemistry* **1997**, *48*, 43-68.

(11) Li, Z.; Beck, P.; Ohlberg, D. A. A.; Stewart, D. R.; Williams, R. S. *Surface Science* **2003**, *529*, 410-418.

(12) The 5min data point of these thinnest wires also shows a slight deviation from the general trend, however the remaining wire thickness was calculated to be only 7.4Å ± 0.8Å. For films <10Å the semiclassical theory employed by Zhang and Butler begins to break down due to quantum effects, potentially accounting for this deviation.

(13) This presumes of course that the plasma produced platinum oxide does not conduct exactly as well as metallic platinum.

(14) Survey scans of the samples revealed no other peaks present except a small adventitious carbon peak. The influence of this adventitious carbon adlayer on the surface (such as minor signal attenuation) on the results presented in the text were calculated to be negligible.

(15) The platinum oxide formed on any similar Pt surface using the same O2 plasma treatment conditions and times is reasonably expected to be identical for this range of experiments and independent of the bulk volume of the underlying Pt.

(16) Peaks were fit using an asymmetric Gaussian-Lorentzian sum function with the constraint that all the peaks in a given range display the same asymmetry and Gaussian/Lorentzian ratio. In addition, the Pt(4f) doublet peaks were fit with the constraint that the doublet separation be held constant for all Pt chemical states.

(17) The signal from the adventitious oxygen signal was determined from bare Pt samples.

(18) Tanuma, S.; Powell, C. J.; Penn, D. R. *Surface and Interface Analysis* **1994**, *21*, 165.

(19) Powell, C. J.; Jablonski, A., NIST Standard Reference Database 82: Electron Effective Attenuation Length Database 1.0 ed.; National Institute of Standards and Technology: Gaitherburg, MD, 2001.

(20) ARtick, 1.0 ed.; National Physical Laboratory, UK National Standards Laboratory, 1999.

(21) Though not substantively different, the oxide thicknesses calculated for the 1min O2 plasma exposure time do appear systematically lower by roughly 0.5Å. This suggests that the 1min exposure period is just on the edge of the transition period between the short-time exponentially decreasing growth regime and the long-time steady-state regime observed for the exposures times examined in this study. In turn, this suggests an exponential time decay constant for the initial oxide growth rate in the range of a few seconds.

(22) NIST, XPS Database, Web ed.; National Institute of Standards and Technology: Gaitherburg, MD, 2004.

(23) All peak positions for Pt(4f) doublet peaks are quoted in terms of the 4f-7/2 peak position. The doublet separation between the 4f-7/2 and 4f-5/2 peaks was taken to be constant at 3.35 for all Pt chemical states.

(24) Atomic sensitivity factors of 0.78 and 4.4 for oxygen and platinum respectively were used for these calculations. These values were obtained from literature and the Kratos XPS instrument database.

(25) PtO and platinum hydroxides are practically indistinguishable by XPS for y<4 because of very similar peak positions.

(26) This value was calculated using the same techniques and attenuation lengths as were used for calculating the total oxide thickness. The attenuation length was assumed to be identical in both oxide components.

(27) The calculation of the composition based on the peak areas from the data fitting accounted for the stratified oxide structure by adjusting for the added attenuation of the PtO2 sub-layer.

(28) Jung, G.-Y.; Li, Z.; Wu, W.; Tong, W. M.; Chen, Y.; Wang, S. Y.; Williams, R. S. *in preparation* **2004**.

(29) Wasserman, S. R.; Tao, Y. T.; Whitesides, G. M. *Langmuir* **1989**, *5*, 1074-1087.

(30) Wasserman, S. R.; Whitesides, G. M.; Tidswell, I. M.; Ocko, B. M.; Pershan, P. S.; Axe, J. D. *Journal of the American Chemical Society* **1989**, *111*, 5852-5861.

(31) Ulman, A. *Introduction to Ultrathin Organic Films*; Academic Press: San Diego, CA, 1991.

(32) Due to large uncertainty in the electron attenuation length in the Pt-oxide overlayer (15%) and factors such as the further incorporation of Pt into the oxide layer above the 7.1Å level, the error on this density approximation is taken to be in the range of 25%.

(33) The horizontal/surface scan size of the AFM microscope was set to zero. However, tip drift was not corrected for and some motion of the tip along the surface during the IV data collection is thus very likely.

(34) The IV curves were averaged from a minimum of 10 individually recorded IV traces, taken successively at the same location at a rate of 1Hz/cycle.

Chapter 5: Template-stripping from Releasing-layers

5.0 *Introduction*

The template-stripping techniques examined in Chapter 2 employed ultra-flat silicon-oxide surfaces as templates for generating ultra-flat noble metal surfaces. As demonstrated by Chapters 3 and 4, and discussed further in Chapter 7, there are a number of nanoscience research and device applications for which the large-area ultra-flat Pt and Au surfaces can be advantageously employed. However, the range of ultra-flat material surfaces that can be produced using templating silicon-oxide or mica, is limited to noble metals with low adhesion to these surfaces. Furthermore, the various template-stripping techniques presented to date do not allow for the generation of patterned TS features.

The demonstration in Chapter 3, of SAMs on ultra-flat surfaces producing highly uniform surface properties, motivated the concept of modifying the ultra-flat silicon-oxide surfaces with a SAM *releasing-layer* to generate new templating surfaces with different properties — in particular, low adhesion to PVD materials more reactive than noble metals. Templating surfaces engineered to allow the template-stripping of non-metallic films, could then be employed to create patterned metal TS features surrounded by an insulating matrix. Such patterned TS features could have greater utility, particularly for device applications, than the large-area TS surfaces demonstrated in Chapter 2.

Based on the low reactivity of fluorinated-carbon (such as Teflon®), it was hypothesized that a uniform, fluorine-terminated, self-assembled monolayer of fluoroalkylsilane molecules could generate the desired, low-adhesive, surface properties. Section 5.1 explores a variety of self-assembly techniques and conditions for different length mono- and tri-chlorosilane fluoroalkylsilane molecules on ultra-flat silicon-oxide surfaces. The SAMs are characterized using ellipsometry, water contact angle and AFM, elucidating the deposition conditions which generate the most uniform SAMs. Furthermore, as a test of the adhesiveness of the fluoroalkylsilane SAM surfaces, the evaporation of aluminium films onto the SAMs is also examined. Whereas the evaporation of aluminium onto silicon-oxide surfaces results in Al films which are strongly adhered to the silicon-oxide, the Al films are demonstrated to template-strip easily from the most uniform fluoroalkylsilane SAM surfaces generated by vapour-phase deposition. This result confirms that the fluoroalkylsilane SAMs act as a *releasing-layer*, allowing the template-stripping of more reactive PVD materials from the ultra-flat surfaces.

With the original intent of comparing to the data presented in Chapter 2, Pt and Au surfaces produced by template-stripping from the fluoroalkylsilane SAMs were selected for examination in Section 5.2. However, the water contact angle and XPS data presented reveals that the evaporation of Pt onto the fluorocarbon releasing-layer SAMs at room-temperature destroys the monolayers. This is shown to contrast the results with gold, where the room temperature evaporation of Au is shown to only disturb, but not destroy, the monolayer. Cooling the fluoroalkylsilane coated silicon-oxide to liquid nitrogen temperatures during the evaporation is also shown to prevent the breakdown of the releasing-layer. These combined results reveal that the Pt atoms can catalyze the breakdown of the fluoroalkylsilane molecules. These data reveal a limitation of using releasing-layer SAMs in the template-stripping process.

Section 5.3 presents the development of a technique for producing micron-scale patterned features of TS features. The technique combines the releasing-layer methodology of Section 5.1, with conventional shadow-masking technology, to generate patterned template-stripped (pTS) Pt features surrounded by both Au and insulating alumina/silica matrices. AFM characterization demonstrates the surface smoothness of the pTS Pt features to correspond well to the large-area TS Pt surfaces studied in Chapter 2.

5.1 *Fluoroalkylsilane SAMs on Silicon-oxide*

5.1.1 Self-assembly of Fluoroalkylsilane Releasing-layers

Chlorosilanes[1-4] were chosen as the reactive self-assembly headgroup over other silane-based alternatives (for example methoxysilanes[5, 6]) based on easy commercial availability. Procedures for solution-based self-assembly were examined first, due to the simplicity and cost-effectiveness of the methods, compared with vapour phase procedures. Because of potential for the polymerization of chlorosilanes in solution,[7, 8] mono-chlorosilane molecules were selected over tri-chlorosilanes for the initial, solution-phase deposition experiments; this avoided the possibility of polymer aggregates of molecules forming and binding to the surface, disrupting the desired ultra-flatness of the surfaces. For the vapour-phase deposition techniques examined second, tri-chlorosilane molecules were also investigated.

When selecting the range of fluoroalkylsilane molecules to examine as SAM releasing-layer (RL) candidates, it was expected that, as the chain length increased, the packing of the monolayer would improve (similar to what is observed for the alkanethiol monolayers in Chapter 3), leading to a more fluorine terminated RL surface.[6] To confirm this trend, three different chain lengths of mono-chlorosilane molecules were selected for exploration, with the aim of roughly evaluating the influence of these two competing factors. The four fluoroalkylsilane molecules studied herein are shown in Figure 5-1, labelled with the acronyms designated to each molecule; the acronyms for the molecules are adopted from literature,[6] and are based on the number of fluorine atoms in the molecule.

In order for silane-based self-assembly to take place, hydroxyl termination of the silicon-oxide surface is required. To prepare the silicon-oxide (templating) substrate for self-assembly, the silicon wafers were immersed in freshly mixed hot piranha (3:1 v/v concentrated H_2SO_4 and 30% H_2O_2) for 15 minutes. This treatment is known to produce hydroxyl terminated silicon-oxide surface, with a density of ~5-6 hydroxyl groups/nm^2.[9]

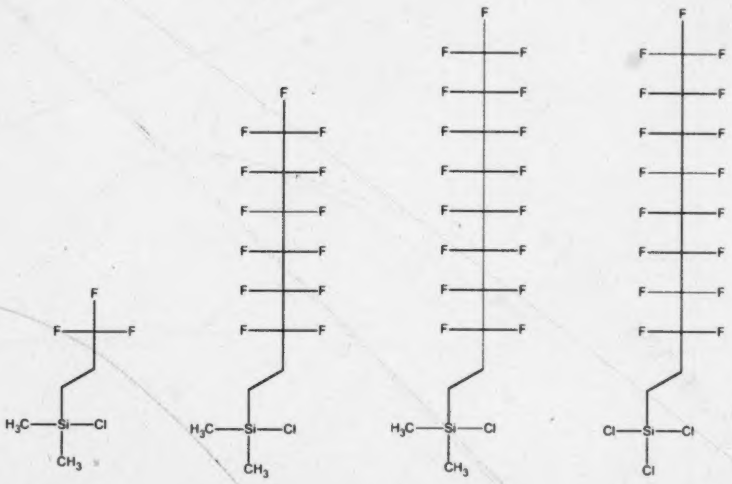

3F **13F** **17F** **17F-T**

Figure 5-1 The range of fluoroalkylsilane molecules self-assembled onto silicon oxide (templating) substrates and explored as possible releasing-layers for template-stripping.

Three anhydrous organic solvents (hexanes, toluene and chloroform) were initially selected for exploration based on previous literature studies of chlorosilane self-assembly.[1-4, 10] Self-assembly solutions were prepared for each of the three mono-chlorosilane molecules in Figure 5-1 at a concentration of ~10 mM in each of the three organic solvents and the substrates were incubated therein for a period of 24 hours before being removed, rinsed and immediately characterized. As the feature of most interest for these monolayers was the terminal surface, water contact angle measurements were employed as the main characterization tool for the first round of experiments.

The water contact angle measurements were performed using a VCA 100 video contact angle system (AST Products Inc., Billerica, MA). Water drops were lowered onto the surface using a syringe dispenser and expanded to a few millimeters in diameter. Once fully expanded, a digital photograph was captured, from which the contact angle between the edge of the water droplet and the surface were calculated using AST software.

Table 5-1 summarises the water contact angle results from these initial experiments; included at the bottom of the table are the detailed experimental procedures followed for the preparation and handling of the samples. Based on the expected water contact angle for completely fluorinated surfaces (~115°-120°), and the known hydrophilicity of clean silicon-oxide (water contact angle≤20°-25°), two important observations can be made from these data. First, reasonable coverage of the substrate by fluorine terminated monolayers only occurred for the fluoroalkylsilane molecules in hexanes. Though previous studies have found hydrogenated-alkylsilanes do self-assemble in toluene and chlorophorm,[4, 10] there appears to be a solvent mediated interaction between the fluoroalkylsilane molecules in these solvents that prevents equivalent behaviour. Secondly, the highest contact angle achieved by the solution based growth after 24hrs was considerably lower than the ~115°-120° expected for a completely fluorinated surface. Using the simple Cassie 2-phase model for water contact angle[11], the highest observed water contact of ~103° can be roughly equated to a defect density of ~15-20%.

Molecule	Hexanes	Toluene	Chlorophorm
3F	73.5°±0.6°	60.1°±1.7°	57.0°±1.7°
13F	97.8°±0.7°	66.8°±1.0°	60.5°±1.5°
17F	103.0°±0.5°	54.5°±0.7°	62.3°±2.3°

Experimental Procedures

- All silicon substrates were cleaned with fresh (hot) piranha for 15 minutes. After removal from the piranha, substrates were rinsed with DI water and dried under a stream of nitrogen.
- The substrates were then immersed immediately in into freshly prepared 10mM solutions of the listed molecule in the listed solvents.
- Substrates were left immersed for 24hrs before being removed, rinsed with the respective neat solvent, followed by rinses with ethanol and DI water, and then dried under a stream of nitrogen. Water contact angle measurements were taken with 1 hour of the substrates removal from the self-assembly solutions.

Table 5-1 Water contact angle from hydroxyl-terminated silicon oxide substrates immersed in a variety self-assembly solutions for 24hours. The reported errors are the standard deviation of at least 4 measurements at different locations on the samples.

A second round of experiments on solution-based self-assembly was conducted, focused particularly on hexanes as the solvent and incorporating a heat treatment technique, demonstrated previously by Geer *et al.*[3]. This technique was explored to examine whether annealing the SAMs could result in the formation of more uniform fluoroalkylsilane SAMs. Incubation times were reduced to 1 hour for the initial incubation in the 10 mM self-assembly solutions, and the substrates were either characterized immediately, or heated to 120°C for four minutes. Re-immersion for a further 30 minutes in the self-assembly solution examined, to determine if heat treatment would anneal the SAMs, exposing pinholes/defects that could be filled by further self-assembly. After the re-immersions, samples were either characterized immediately, or exposed to a second four minute, 120°C minute heat treatment, prior to characterization. All samples were characterized with both water contact angle and ellipsometry.

Ellipsometry was performed on the SAMs using a variable-angle Gaertner ellipsometer (Gaertner Scientific Corporation, Skokie, Il), operating at three wavelengths (543.5nm, 632.8nm and 832.2 nm) and a typical incident angle of 70°. The complex refractive indexes of the substrates at these wavelengths were determined from readings on bare, fresh substrates, immediately prior to examining SAMs on similar substrates. The thicknesses of the SAMs were calculated using a three-phase model (air-monolayer-substrate) in the Gaertner software; a minimum of five different locations on each sample were examined.

The data from the characterization of the SAMs generated in the second series of solution-phase experiments are provided in Table 5-2; the detailed experimental procedures followed for sample preparation and handling are again provided at the bottom of the table. Comparing the contact angle data in Table 5-1 to that in Table 5-2 demonstrates that the results are nearly identical for all the various hexanes based self-assembly conditions examined. These data show the heat treatments, re-immersion steps and long (24hr) incubation periods having, at most, a minor influence. The ellipsometry thicknesses listed in Table 5-2 also suggest the surface coverage is less than complete, as the observed thicknesses are mostly smaller than the lengths of the three mono-chlorosilane molecules: ~4 Å (3F); ~10 Å (13F); and ~13 Å (17F). These data demonstrate that none of the solution-based self-assembly conditions explored generated the desired, highly uniform, fluorine-terminated surface.

Molecule	**Hexanes Proc A**	**Hexanes Proc B**	**Hexanes Proc C**	**Hexanes Proc D**	**Ambient Vapour Phase Deposition**
3F	**75.4°** ±1.7° (3.7±1.0Å)	**72.2°** ±0.1° (4.0±1.2Å)	**76.8°** ±0.9° (2.5±1.1Å)	**75.8°** ±0.4° (3.0±1.8Å)	**89.7°** ±0.4° (4.6±1.6Å)
13F	**87.9°** ±0.4° (3.6±1.5Å)	**88.5°** ±0.4° (3.5±1.0Å)	**96.2°** ±0.5° (3.6±1.7Å)	**95.7°** ±0.8° (3.4±1.3Å)	**111.2°** ±1.1° (4.6±1.6Å)
17F	**101.5°** ±0.6° (6.2±1.9Å)	**103.1°** ±0.5° (5.6±2.0Å)	**99.8°** ±0.4° (5.9±2.2Å)	**98.7°** ±0.6° (4.5±2.4Å)	**114.1°** ±0.9° (8.2±2.0Å)

Experimental Procedures

- All silicon substrates were cleaned with fresh (hot) piranha for 15 minutes, followed by rinsing with DI water and drying under a stream of nitrogen.

Hexanes Procedures

- All substrates were immersed immediately after piranha cleaning in into 1wt% solutions of the listed molecule in hexanes for 60 minutes.[†]

Proc A: After 60 minutes substrates were rinsed in order with hexanes, ethanol and DI water and characterized as is.

Proc B: After 60 minutes substrates were rinsed with hexanes and then placed on a hot plate at 120°C for 4 minutes. After removal from the hot plate, the substrates were rinsed with ethanol and DI water and characterized as is.

Proc C: After 60 minutes substrates were rinsed with hexanes and then placed on a hot plate at 120°C for 4 minutes. After removal from the hot plate, the substrates were re-immersed in the self-assembly solution for a further 30 minutes before being removed and rinsed in order with hexanes, ethanol and DI water and characterized as is.

Proc D: After 60 minutes substrates were rinsed with hexanes and then placed on a hot plate at 120°C for 4 minutes. After removal from the hot plate, the substrates were re-immersed in the self-assembly solution for a further 30 minutes before being removed and rinsed with hexanes, followed by re-heating on the hot plate at 120°C for a further 4 minutes. Substrates were then rinsed with ethanol and DI water and characterized as is.

Vapour Phase Deposition Procedure

- Substrates loaded immediately after piranha cleaning into the specialty deposition chamber containing ~200μL of the neat molecular liquid. The chamber was heated to 150°C for 120 minutes and immediately upon removal from the chamber, the substrates were sonicated in hexanes and the rinsed in order with hexanes, ethanol and DI water and characterized as is.

Table 5-2 Water contact angle and ellipsometric thicknesses of fluorinated alkane chains on piranha cleaned silicon oxide substrates deposited by a variety of self-assembly procedures. The reported errors are the standard deviation of at least 4 measurements at different locations on the samples.

As a result, the vapour-phase deposition of the SAMs was explored next. Hozumi *et al.*[6] previously demonstrated a straightforward ambient-condition, vapour-phase deposition process. The technique involves placing a fresh substrate

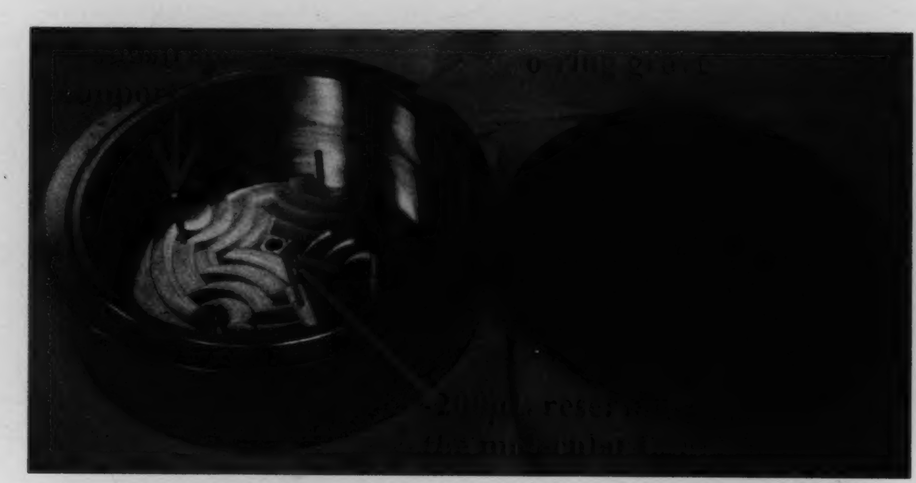

Figure 5-2 Specially fabricated, gold coated chamber for the ambient-condition vapour-phase deposition of chlorosilane-based molecules.

into a sealed chamber with a small volume of the molecular liquid, and then heating the chamber to vaporise the molecules. Freshly piranha cleaned silicon-oxide substrates were loaded into the sealed deposition chamber and ~200μL of the selected molecular liquid was loaded into the reservoir at the bottom of the chamber. After sealing in ambient conditions, the whole chamber was heated to 150°C for 120 minutes, vaporising the molecular liquid and allowing the molecules to assemble on the silicon-oxide surface from vapour phase. After cooling for ~15 minutes, the substrates were removed from the chamber and sonicated in hexanes for ~5 minutes to remove physisorbed molecules. Following this step, they were rinsed, dried and immediately characterized with water contact angle and ellipsometry measurements.

For this procedure a specially fabricated deposition chamber was required. One of the byproducts of the chlorosilane self-assembly processes is hydrochloric acid which—especially in the vapour phase — can be highly corrosive to many materials, including most metals. A metal deposition chamber is highly desirable to facilitate good uniform heating of the chamber and avoid 'cold spots' where molecular condensates can form. As such, the chamber shown in Figure 5-2 was designed and fabricated out of aluminium and then commercially plated with gold to provide the necessary resistance to hot HCl. (NOTE: These experiments should ***always*** be conducted in a fumehood in case of leaks from the deposition chamber. Vapour phase fluoroalkylsilane molecules and hot HCl can be extremely hazardous, and physical contact or inhalation must be avoided.)

The results of the water contact angle and ellipsometry measurements made for the vapour phase deposited monolayers are provided in the right column of Table 5-2, for easy comparison to the previous data; the experimental procedures followed for the vapour phase depositions are also included at the bottom of the table. Immediately apparent are the substantially higher water contact angle values for the vapour deposited SAMs than were achieved with solution-phase deposition. The anticipated trend of higher uniformity with increasing length of the fluoroalkylsilane chain is also demonstrated clearly by these data, with the ~114° water contact angle observed on the F17 film being close to that expected for a completely fluorinated surface (~115°-120°). Additionally, the ellipsometry thicknesses demonstrate increases in the thickness of the SAMs relative to the solution-phase monolayers, indicative of more complete surface coverage.

Samples of F3, F13 and F17, prepared using the vapour-phase deposition procedure detailed at the bottom of Table 5-2, were also examined using tapping-mode atomic force microscopy (TM-AFM). The TM-AFM imaging was carried out on a Digital Instruments Dimension 3000 microscope. Figure 5-3 shows representative $(1\mu m)^2$ TM-AFM images of the three different releasing-layers. The TM-AFM characterization supports the results of the contact angle and ellipsometry data, demonstrating that as the chain length increases from F3 to F17 the quality of the coverage and uniformity of the monolayer also increases. Figure 5-3 (c) shows the top of the F17 monolayer on the silicon-oxide surface to be homogenous and smooth, with an RMS roughness nearly equivalent to that of the underlying silicon-oxide surface. Summarized in Table 5-3 are the AFM measured RMS roughness values over $(1\mu m)^2$ of the three monolayers. For comparison, the underlying silicon-oxide surface of the prime polished wafers used for these experiments has a measured roughness value of ~0.7Å over $(1\mu m)^2$ (Chapter 2, Section 2.2.1). Based on these results, the F17 monolayer, deposited using the ambient-condition vapour-phase deposition process appeared to be the

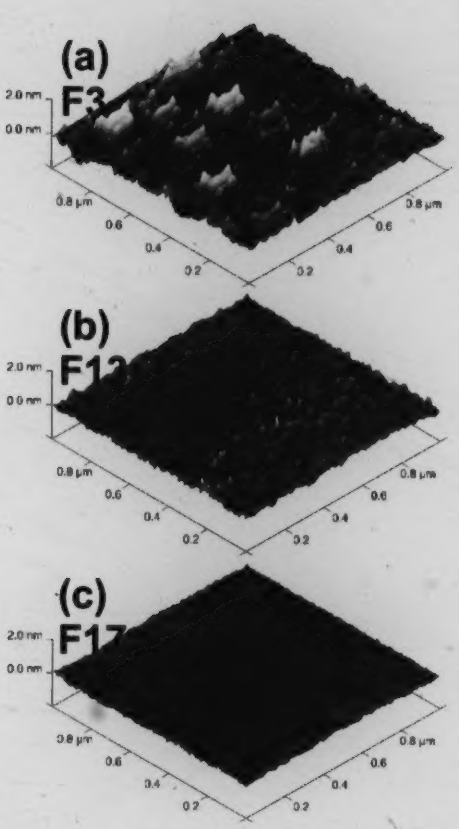

Figure 5-3$(1\mu m)^2$ AFM images of vapour phase deposited (a) F3, (b) F13 and (c) F17 monolayers on a silicon oxide wafer. The respective RMS roughness values for these surfaces can be found in Table 5-3.

Vapour Phase Deposited Releasing Layer	RL on Silicon Oxide AFM Roughness over $(1\mu m)^2$
F3	~2.0Å
F13	~1.1Å
F17	~0.7Å

Table 5-3 RMS roughness values over $(1\mu m)^2$, measured by tapping mode AFM, for the mono-chlorosilane releasing-layer SAMs on silicon-oxide shown in Figure 5-3.

best candidate for use as a template-stripping releasing-layer among the mono-chlorosilane molecules examined.

Attempts were also made to form uniform monolayers of the same length tri-chlorosilane molecule (F17-T; see Figure 5-1) using the various solution-phase and ambient condition-vapour phase deposition techniques. However, both AFM and ellipsometry revealed significant molecular aggregation and multi-layer formation, creating surfaces which substantial roughness on the nanoscale. These techniques were thus discounted for use with the tri-chlorosilane molecules.

In collaboration with Gun-young Jung (HP Labs), one different self-assembly technique for a tri-chlorosilane molecule (F17-T) was also examined. The self-assembly process was carried out by vapour phase deposition in low vacuum conditions, and alternated the deposition of the F17-T molecule with intermittent exposure to low pressures of water vapour. Freshly piranha cleaned samples of silicon-oxide were loaded into a home-built, low vacuum chamber and pumped down to a based pressure of ≤1 mTorr. Once the base pressure was reached, samples were exposed to an 80°C vapour of the F17-T, at a static pressure of 300 mTorr, for 15 minutes, and then the chamber was purged back to ≤1 mTorr. The samples were then exposed to deionized water vapour, at a static pressure of 800 mTorr for 5 minutes, followed by re-purging to ≤10 mTorr. Two more 15 minute exposures to the F17-T vapour, separated by one more 5 minute exposure to water vapour, were conducted, with the chamber being purged between each step.

After removal from the vacuum deposition chamber, the monolayers were rinsed in neat hexanes, and subject to immediate characterization using the water contact angle, ellipsometry and TM-AFM. These vacuum deposited F17-T releasing-layers demonstrated a water contact angle of ~118°, an ellipsometric thickness of 9.5 Å and an RMS surface roughness over $(1\mu m)^2$ of ~0.9 Å. These data indicate good monolayer coverage, excellent uniformity in the fluorine termination of the F17-T SAMs and roughness values approximately equivalent to the underlying ultra-flat silicon-oxide surface. Additionally, these data suggest F17-T SAMs are even better candidates for use as a template-stripping releasing-layer than the F17 ambient-condition vapour-phase SAMs. Attempts to template-strip evaporated aluminium films from both the F17 and F17-T SAMs, documented in the following subsection, confirm this suggestion.

5.1.2 Template-stripping Aluminium from Releasing-Layers

For the template-stripping experiments, freshly prepared vapour-phase deposited SAMs of F17 and F17-T were prepared and the substrates were immediately loaded into the metal evaporation chamber. The chamber was then pumped down to a based pressure of $\leq 1 \times 10^{-6}$ torr (~30-45 minutes) before the evaporation was begun. The aluminium evaporations (carried out by electron-beam evaporation) were started at 0.1 Å/sec and held at that rate for the first 50 Å. The rate was increased to 0.5 Å/sec for another 100 Å, before finally being raised to between 1.0-2.0 Å/sec until the final film thickness of 100 Å was reached. The slow initial evaporation rate was chosen in an attempt to minimize the heating and metal penetration into the releasing-layer. After the evaporation step, substrates were allowed to cool for ~20 minutes and then removed from the evaporation chamber.

The adhesion of the evaporated Al films to the SAM coated silicon-oxide substrates was initially tested using an adhesive tape-test.[12] Immediately after removal from the evaporation chamber, the Al films evaporated onto F17-T monolayers were easily lifted-off of the substrate using the adhesive tape, indicating very low adhesion between the film and the substrate. By comparison, Al films evaporated onto freshly piranha cleaned silicon-oxide adhere strongly to the surface and cannot be lifted off. This result demonstrates that highly uniform, fluorine-terminated surfaces can be used for the template-stripping of aluminium films.

The Al films evaporated onto F17 monolayers, conversely, adhered strongly to the substrate and could not be lifted-off. The differences in the water contact angles observed on the two releasing-layer SAMs (~119° for the F17-T; and ~114° for F17) is indicative of a difference in the defect density in the two monolayers. The inability to lift-off the aluminium film from the F17 SAM indicates that sufficient defects exist for the evaporated aluminium to for strong adherent contact with the underlying silicon-oxide. As AFM imaging indicated a uniform surface for both SAMs, contact angle measurements appear the most reliable measure for determining the uniformity of the surface termination for the releasing-layers.

TS Al surfaces were produced from Al films deposited onto the F17-T SAM releasing-layers, using a sample preparation similar to that described in Chapter 2 (subsection 2.1.1), with the heat-cured epoxy being replaced with a UV-curable epoxy, in order to avoid any heat-treatment of the samples. AFM of the TS Al surfaces immediately after stripping demonstrated roughness values of ~3Å RMS over $(1\mu m)^2$. While these roughness values are higher than those observed in Chapter 2 for the TS Pt and TS Au, the TS Al films are still are substantially smoother than the surface Al films deposited using most conventional PVD processes such as evaporation. The detailed investigation of the properties of the TS Al surfaces, including the process of surface which occurs immediately after stripping, was left outside the scope of the present research.

5.2 Template-stripping Pt and Au from Releasing-layers

To understand the influence of the releasing-layer SAMs on generated TS surfaces, releasing-layer template-stripped (RL-TS) Pt and RL-TS Au surfaces were produced by template-stripping metal films evaporated onto the fluoroalkylsilane monolayers. It was originally intended that the characterization of these RL-TS surfaces be directly comparable to the data presented in Chapter 2 for TS Pt and TS Au surfaces prepared from bare silicon-oxide templating surfaces. However, as is demonstrated below, it was revealed that an unanticipated reaction between the evaporated Pt and the fluoroalkylsilane molecules takes place.

Immediately after the releasing-layer SAMs were prepared, using the vapour-phase deposition procedures described in the previous section, the substrates were loaded into the metal evaporation chamber. The chamber was pumped down to a base pressure of $\leq 1\times10^{-6}$ torr (~30-45 minutes) before the evaporation was begun. Metal evaporations, carried out by electron-beam evaporation, were started at 0.1Å/sec and held at that rate for the first 50 Å. The rate was increased to 0.5 Å/sec for another 100 Å, before finally being raised to between 1.0-2.0 Å/sec until the final film thickness of 100 Å was reached. The slow initial evaporation rate was chosen in an attempt to minimize the heating and metal penetration into the releasing layer. After the evaporation step, substrates were allowed to cool for ~20 minutes and then removed from the evaporation chamber. Samples were prepared for template-stripping using an organic adhesive technique similar to the procedure described in Chapter 2 (subsection 2.1.1), with a UV curable epoxy used in place of the heat-cured to avoid heat treating the samples.

After template-stripping, water contact angle measurements were performed on the templating substrates in order to explore the impact of the metal evaporation and lift-off on the releasing-layer SAMs. Table 5-4 lists water contact angles recorded from the fluoroalkylsilane SAM coated templating surfaces, immediately after the stripping of both Pt and Au films from the surface. Recalling from the previous section that the releasing-layer SAMs demonstrated water contact angles ≤114°, the data in Table 5-4 demonstrate that evaporation and lift-off of both metals results in a disruption of the fluorine-termination of the surfaces. In the case of the Pt templating surface, in fact, the surface appears to have no residual fluorine termination, and demonstrates a water contact angle in good agreement with expectations for a completely clean silicon-oxide surface. As the silane-based SAMs are known to covalently bond to the silicon-oxide surface, the apparent disappearance of the fluoroalkylsilane molecules was unexpected. In the case of the Au templating surface, the contact angle data indicated that, while disruption of the SAMs was evident, a substantial quantity of the fluoroalkylsilane molecules was still present on the surface.

Evaporated Metal	Contact Angle of Template after Stripping
Pt	29.2° ± 0.3°
Au	86.6° ± 0.2°
Cold Pt[†]	96.3° ± 1.2°

[†] Templating substrate was cooled to 77K during the evaporation of the Pt.

Table 5-4 Water contact angle measured from the fluoroalkylsilane coated silicon-oxide templating surfaces, after the template-stripping of various metals from the surfaces.

It is hypothesized that the hot Pt atoms landing on the fluoroalkylsilane monolayers could be breaking down of the releasing layer molecules either by chemical catalysis or heat transfer. To test this hypothesis, an F17 coated template was loaded into the evaporation chamber and cooled to liquid nitrogen temperatures prior to the evaporation of the Pt film. It was conjectured that the lower temperate of the substrate would hinder any chemically catalyzed or heat based breakdown of the fluoroalkylsilane molecules. As shown in Table 5-4, after the 'cold-Pt' was template-stripped, the templating surface demonstrated a water contact angle similar to that of the Au template. The cold-Pt still disrupted, but did not entirely remove, the fluoroalkylsilane SAM from the silicon-oxide surface.

To confirm the above hypothesis, X-ray photoelectron spectroscopy (XPS) was used to examined both the RL-TS Pt and RL-TS cold-Pt metal surfaces, along with the templates from which they were stripped. The AR-XPS was carried out

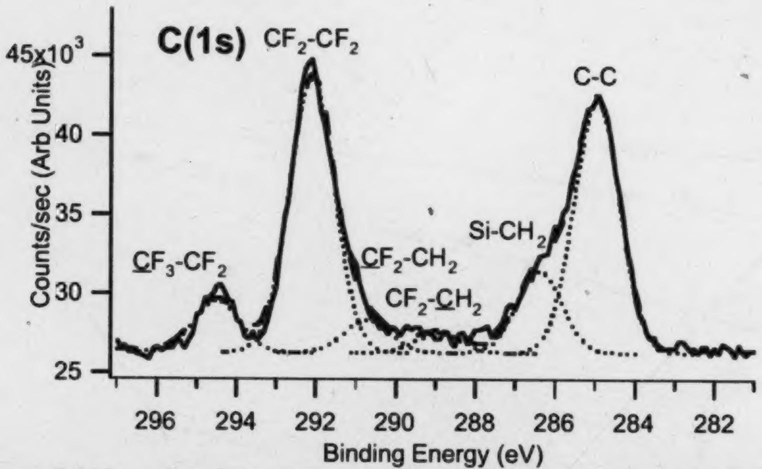

Figure 5-4 X-ray photoelectron spectrum of the C(1s) peak region for a fluoroalkylsilane SAM on silicon-oxide. The dotted and dashed lines are the fit to the experimental data. The 6 observed chemical species of carbon are listed above their respective peak positions.

on an AXIS 165 from Kratos, at the *Alberta Center for Surface Engineering and Science* (ACSES) with the assistance of Dimitre Karpuzov. Samples were freshly stripped in ambient conditions immediately before loading into the AR-XPS vacuum chamber, with exposure times kept to a minimum, in the range of a few minutes.

Shown in Figure 5-4 is the XP spectra for the C(1s) range for an undisrupted fluoroalkylsilane releasing-layer on a silicon-oxide surface. Data fitting reveals the presence of 5 peaks related to the F17 molecule (from left to right: $\underline{C}F_3$-$CF_2 \approx 294.5$ eV; $\underline{C}F_2$-$\underline{C}F_2 \approx 292.2$ eV; $\underline{C}F_2$-$CH_2 \approx 290.8$ eV; CF_2-$\underline{C}H_2 \approx 289.0$ eV; and Si-$\underline{C}H_2 \approx 286.6$ eV) with relative intensity ratios roughly as expected for the concentrations of the various carbon environments in the molecule, and one peak ($\underline{C}$-$\underline{C} \approx 284.9$ eV) due to adventitious carbon. This spectrum was used as the benchmark against which to evaluate other samples. Figure 5-5 compares this same spectrum to spectra obtained from RL-coated templating surfaces after the removal of Pt evaporated on identical monolayers at both room-temperature and 77K (cold-Pt). Also included in Figure 5-5 is a similar ranged spectra from the room-temperature evaporated RL-TS Pt surface, templated-stripping from the corresponding templating surface.

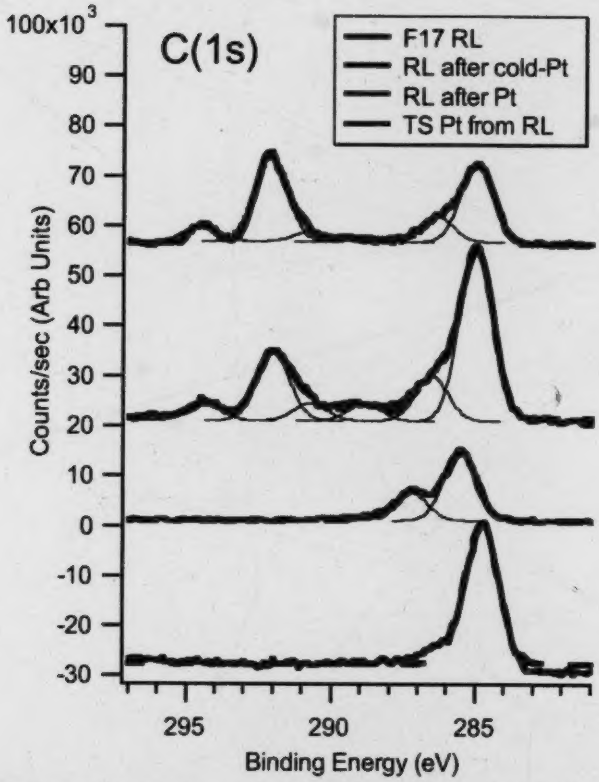

Figure 5-5 X-ray photoelectron spectra of the C(1s) peak region for: a releasing-layer on silicon-oxide; a releasing-layer after Pt was evaporated while the substrate was cooled to 77K, and then template-stripped; a releasing-layer after Pt was evaporated at room temperature and then template-stripped; and the corresponding room-temp evaporated RL-TS Pt surface template-stripped off of the RL. The dotted and dashed lines are the fit to the experimental data.

Comparing the spectra in Figure 5-5 demonstrates that the fluorinated-carbon signals disappear entirely from the templating surface after the room-temperature Pt evaporation. Comparatively, these same signals remain relatively intact on the cold-Pt, with the only major change being the increase in the adventitious carbon signal. At the same time, the intensities of the Si-C signal from all three RL-coated surfaces are roughly the same, indicating that the bottom portion of the fluoroalkylsilane molecules, containing the covalent Si-C bond of the molecule, is still present on the templating surface even after the room temperature Pt evaporation.

These data verify the hypothesis that the fluoroalkylsilane molecules are broken down by the Pt atoms landing on the room-temperature releasing-layer SAM. Furthermore, these results indicated that the breakdown of the molecules occurs above the Si-C bond at the bottom of the F17 molecule, though still removing all of the fluorinated carbons from the surface. The catalytic role of Pt atoms in breaking the C-H bonds of methane molecules, leading to longer chain hydrocarbon formation, has been documented in literature.[13-17] Based on the XPS data and the previous literature, it is proposed that the hot Pt atoms are catalyzing the breakdown of the molecules at bottom, CH_2-CH_2 portion of the fluoroalkylsilanes (see Figure 5-1).

The bottom spectrum shown in Figure 5-5 is of the room-temperature evaporated RL-TS Pt surface. Observable in the figure is the lack of any fluorinated carbon signals — only adventitious carbon appears present on the ultra-flat Pt surface. To further verify this result, Figure 5-6 displays the F(1s) signal window for the same four samples as examined in Figure 5-5. In Figure 5-6 both the room-temperature RL-TS Pt film and room-temperature Pt template demonstrate only trace amounts of fluorine compared with the original releasing-layer (and the cold-Pt template, which is very close to the original releasing-layer). This suggests that the ultra-flat Pt film is, in fact, not covered by the missing portions of the fluoroalkylsilane molecules. If the catalytic breakdown of the fluoroalkylsilane molecules occurs during the initial stages of the Pt evaporation, it is likely that the fluorinated components of the molecules are released into the high-vacuum evaporation chamber, and thus removed from the surface entirely.

XPS spectra were also recorded for RL-coated templating surfaces after the stripping of evaporated Au films from the template. As expected from the contact angle data, the XP spectra demonstrated revealed the same behaviour as observed for cold-Pt template. In addition, XPS of the RL-TS Au surface revealed no fluorinated carbon present, and only trace amounts of fluorine.

The data presented in this section reveal that, while the use of releasing-layers for template-stripping does enable the production of new TS surfaces (such as the

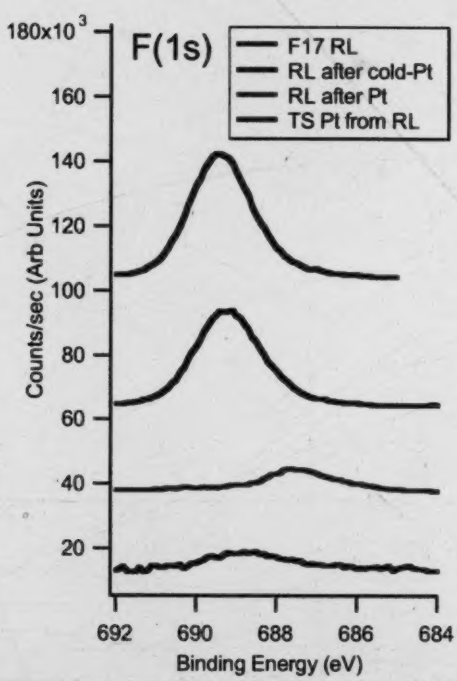

Figure 5-6 X-ray photoelectron spectra of the F(1s) peak region for: a releasing-layer on silicon-oxide; a releasing-layer after Pt was evaporated while the substrate was cooled to 77K, and then template-stripped; a releasing-layer after Pt was evaporated at room temperature and then template-stripped; and the corresponding room-temp evaporated RL-TS Pt surface template-stripped off of the RL. The dotted and dashed lines are the fit to the experimental data.

TS Al demonstrated in Section 5.1), careful examination is necessary to look for reaction between the evaporated materials and the releasing-layers. The potential for contamination of the TS surface with residue from the releasing-layer molecules is possible and should be guarded against. For the Pt case, it appears as if the residues of the broken-down fluoroalkylsilane molecules are not present on the TS Pt surface. However, the procedure for producing patterned template-stripped (pTS) Pt features demonstrated in the next section avoids the possibility entirely by depositing the releasing layers after the patterned Pt metal is deposited on the bare silicon-oxide surface.

5.3 Patterned Template-Stripping

Based on the focus on Pt in previous chapters and the advantages of Pt discussed in Chapter 1, it was deemed desirable to produce pTS Pt features. For use in electronic applications in particular, pTS Pt features surrounded by an insulating matrix were considered most desirable. Because of the breakdown of the fluoroalkylsilane releasing-layer molecules observed in the previous section, a process was developed whereby the patterned Pt features were first deposited on a bare silicon-oxide templating surface (identical to those employed in Chapter 2). The deposition of the releasing-layer on the areas of the silicon-oxide template not covered by the metallic features was then carried out. Finally, a material matrix could be deposited across the entire substrate surface, covering both the pTS Pt features and the releasing-layer. The concept was for the matrix to adhere strongly to the Pt, but not the releasing-layer. As a result, the matrix could then be used to lift the pTS Pt features off of the silicon-oxide surface, leaving the features embedded in an insulating matrix.

A variety of conventional lithographic techniques exist for patterning PVD metal thin films. However, the majority of these techniques require good film adhesion to the substrate, in order to prevent the lift-off of the patterned metal features during the removal of the chemical resists used in the lithography process. The low adhesion required to allow deposited metal films to be template-stripped prevents many of these lithographic techniques from being employed. The alternative pursued for this research was to use physical shadow-masks to fabricate the patterned metal features for template-stripping. The physical removal of the shadow-mask tangentially to the substrate surface leaves patterned metal features on an uncontaminated templating silicon-oxide surface.

Immediate after piranha cleaning, ultra-flat Si wafers (4" <100> prime, P-type; Boron doped; 1-20 Ω·cm; Silicon Valley Microelectronics, CA) were loaded into the metal evaporation chamber. Physical shadow masks with micron scale features were placed on the surface of the wafers and held in place with a home-built clamping system, designed to ensure uniform contact of the shadow-mask to the wafer surface. The chamber was pumped down to a base pressure of $\leq 1 \times 10^{-6}$

torr (~30-45 minutes) before the evaporation was begun. Pt evaporation, carried out by electron-beam evaporation, was started at 0.1 Å/sec and held at that rate for the first 50 Å. The rate was increased to 0.5 Å/sec for another 100 Å, before finally being raised to between 1.0-2.0 Å/sec until the final film thickness of 100 Å was reached. After removal from the evaporation chamber, the shadow-mask was removed from the wafer surface, leaving patterned Pt features on the surface.

The silicon-oxide substrates with patterned Pt features were then immediately loaded into the vapour-phase deposition chamber for the fluoroalkylsilane SAM, and the deposition of the releasing-layer was carried out as described in Section 5.1. Ellipsometry, water contact angle and RAIRS characterization of fresh, blanket Pt surfaces, deposited using the same process as the patterned TS features, demonstrated that only minor amounts of physically adsorbed fluoroalkylsilane molecules were present on any of the surfaces after the vapour-phase deposition procedure. This was an essential result; a well-formed releasing layer on the surface of the Pt features could prevent adhesion between Pt and the deposited material matrix.

Another issue of potential concern was that the vapour-phase deposition procedure could lead to fluoroalkylsilane molecules being drawn between the surfaces of the Pt features and the silicon-oxide template. Inspection of the patterned Pt features by optical microscopy and AFM did not reveal any signs of delamination of the micro-scale patterned metal features, suggesting that such contamination of the pTS Pt surfaces with fluoroalkylsilane molecules was not occurring. Spectroscopic examination of the pTS Pt features after stripping (later in this section) confirms this supposition.

From the previous section, Au was known to have low adhesion to the releasing layer, and also adheres strongly to clean Pt. Gold was thus selected as the material matrix for surrounding the pTS Pt features for the first experiment. Once the substrates with the shadow-mask patterned Pt film had undergone the fluoroalkylsilane vapour-phase deposition process, the substrates were loaded back into the metal evaporation chamber, and a 100nm film of Au was evaporated onto the whole substrate at a rate of 1.0Å/sec. After removal from the electron-

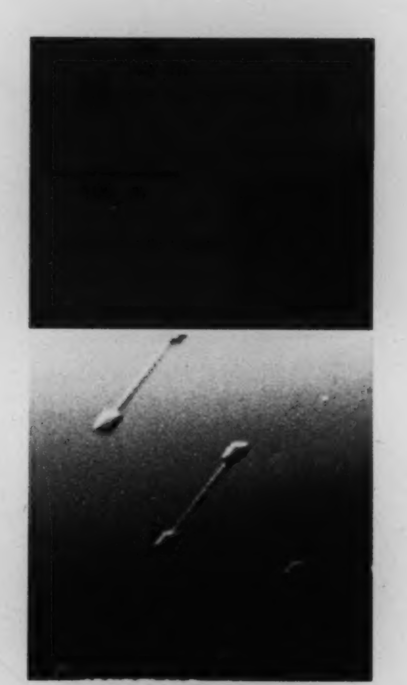

Figure 5-7 Optical micrographs TS Pt patterns in a surrounding Au matrix.

beam evaporation chamber, glass backing pieces were attached using UV curable epoxy and template-stripping was attempted.

Figure 5-7 shows optical micrographs of the successfully template-stripped, micro-scale patterned Pt in the surrounding Au matrix. The micro-scale pattern of the Pt films from the shadow mask is shown to be quite successfully retained in the pTS surface. Figure 5-8 shows several perspective views of a $(15\mu m)^2$ TM-AFM image of a micro-scale TS Pt wire in the Au matrix. Topographical variations at the boundary between the Pt wire and the surrounding Au matrix are visible in the image, however are less than 10 nm in height over several microns and are relatively smooth along the local surface. Contact mode AFM imaging at the centre of the Pt wires demonstrates RMS roughness values of ~1.5 Å over $(1\mu m)^2$; this roughness is in reasonable agreement with that expected for TS Pt films that have undergone no annealing (see Chapter 2).

To confirm that no fluoroalkylsilane contamination was present on the TS Pt surface, scanning XPS and scanning TOF-SIMS (time-of-flight-scattered-ion-

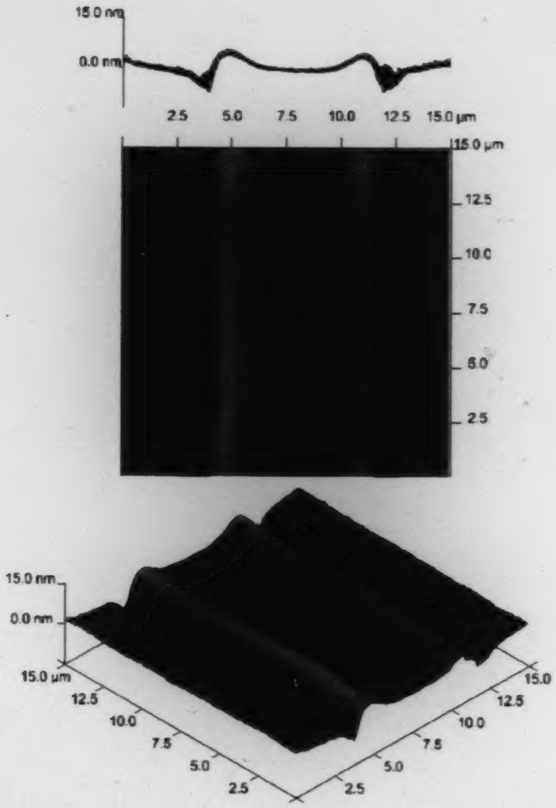

Figure 5-8 Tapping mode AFM images of patterned template-stripped Pt micron-scale wires in a surrounding Au matrix.

mass-spectroscopy) were both employed to image the pTS surface for fluorine atoms. Neither technique revealed the presence of significant amounts of fluorine atoms on the Pt or the surrounding Au. Shown in Figure 5-9 are TOF-SIMS images of the Pt, Au and F atoms on the pTS surface (equivalent scanning-XPS images were also acquired – TOF-SIMS images are shown due to their higher resolution). Comparing Figure 5-9 (a) and Figure 5-9 (b) demonstrates clearly the sharp distinction between the Pt pattern and the surrounding Au matrix. Figure 5-9 (c) shows only a background noise signal for the F atoms on the surface — the visible contrast between the Pt and Au regions is caused by the different background noise levels of the two surfaces. This is consistent with the XPS results of the previous subsection which demonstrated that Au template-stripped

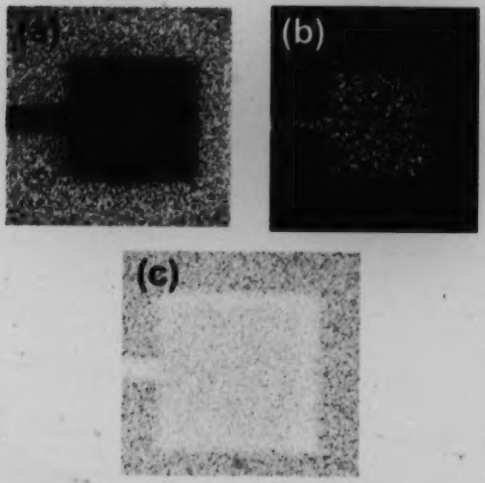

Figure 5-9 Scanning time-of-flight-scattered-ion-mass-spectroscopy (TOF-SIMS) images of the template-stripped Pt patterns in the surrounding Au matrix. The images respectively show the location of: (a) Au atoms; (b) Pt atoms); and (c) fluorine atoms.

from the fluoroalkylsilane releasing-layers had no fluorine present on the surface. These results confirmed that the micron sized pTS Pt features were indeed free of contamination by the fluoroalkylsilane molecules. As such, the surfaces of the patterned TS Pt features are expected to exhibit the same properties as the TS Pt surfaces characterized in Chapter 2.

To the best knowledge of the author, these pTS Pt features represent the first demonstration of surfaces with patterned, ultra-flat template-stripped features. However, the conductivity of the surrounding Au matrix prevents the use of the pTS Pt features for a variety of electronic applications, where electrical isolation of the individual features is required. The ideal insulating matrix would be silicon-oxide, as it is the present standard in electronic devices, and is thus well understood. However, noting that Pt films evaporated on silicon-oxide easily template-strip, the adhesion between silicon-oxide and these metals is clearly low; thus the adhesion of an evaporated silicon-oxide matrix to the pTS Pt features was expected to be equally poor. Using higher energy PVD techniques, such as sputtering, could produce reasonable adhesion. However, attempts to use silicon-oxide sputtering revealed that the high energy of the technique results in the silicon-oxide penetrating through the releasing-layer, into contact with the underlying silicon-oxide substrate, and forms strong adhesion to the surface. As a result, the silicon-oxide matrix cannot be template-stripped from the surface.

After several experimental iterations, an alternative path to an insulating matrix was established. First, the samples were reloaded into the e-beam evaporation chamber and a blanket ultra-thin (~25Å) film of Al was deposited at 0.1 Å/sec over the whole substrate surface after both the patterned Pt features and the fluoroalkylsilane releasing-layer SAM were deposited. While Al does have good adhesion Pt, Section 5.1 demonstrated the adhesion of the aluminium films to the releasing-layer is sufficiently low to allow template-stripping. Furthermore, upon exposure to ambient conditions, the aluminium oxides rapidly, consuming ~15-20 Å of Al and converting it to insulating alumina.[18] In the devised process, the Al film is first oxidized on the surface facing away from the templating substrate. This occurs immediately after exposure to ambient conditions after removal from the metal deposition chamber. At this point, the samples were left in ambient conditions for ≤1 hour to allow this stage of aluminium oxidation to be fully completed.

To provide a more rigid insulating support for the pTS Pt features, the samples were then loaded into a sputtering chamber and 200 nm of silicon-oxide was sputtered over the whole substrate. While silicon-oxide sputtered directly onto the releasing-layer was observed penetrate the SAM and bind to the underlying silicon-oxide surface, the ultra-thin aluminium/alumina overcoat proved sufficient to cap the releasing-layer and prevent the penetration of the silicon-oxide. After removal from the sputtering chamber, pieces of silicon wafer (~1cm^2) were adhered to the top of the final film using the same heat-cured epoxy procedure described in Chapter 2 (subsection 2.1.1). After the silicon backing pieces were attached, mechanical stripping was easily accomplished using tweezers or razor blades, exposing the bottom of the aluminium film. At this stage, the reverse side of the aluminium film is exposed to ambient conditions, allowing a second oxidization stage. Between the two oxidation stages, the majority of the ~25 Å Al film was expected to be converted to alumina. The complete electrical isolation of neighbouring pTS Pt features, laterally separated by ≥100 μm, and connected only by the insulating matrix, was confirmed for a voltage range of ±20 V using a micro-contact probe station.

TM-AFM images of a micron sized TS Pt wire surrounded by alumina are shown in Figure 5-10. The RMS roughness over $(1\mu m)^2$ measured in the middle of the 8 μm wire is ~1.1 Å (representative of several wires examined), demonstrating excellent agreement with the blanket TS Pt studied in Chapter 2. At the boundary between the Pt wire and the surrounding Al_2O_3 matrix a ~4 nm deep trench is visible in Figure 5-10 (c) spread over ~1 μm, similar to the one observed for the pTS Pt in the Au matrix (see Figure 5-8). As the originally evaporated Pt patterns have poor adhesion to the silicon-oxide surface (resulting in the capacity for template-stripping), this trench may be the result of the Pt atoms not wetting the surface and balling at the edge of the Pt patterns. When the subsequent backing layer is tangentially evaporated onto the film the balled edge would shadow the underlying region, resulting in the observed trench. This behaviour would be consistent for both the Au and alumina/silica backing layers.

Despite this edge trench, Figure 5-10 (c) clearly demonstrates that the Pt surface is still exceptionally smooth, demonstrating that the ultra-flatness of the Pt surface is preserved and no large topographic variations are observed. The vertical spikes observed at the boundary between the Pt wire and the surrounding alumina surface in the larger scans — Figure 5-10 (a) and (b) — are shown by smaller area scans such as Figure 5-10 (c) to be artefacts of the scan size and rate. It is reasonable to assume that, at the trench, the pTS Pt surface will exhibit a higher number of atomic steps, as well as step bunching, than was observed on the blanket TS Pt surface in Chapter 2, due to the surface slope. However, the slope of the pTS Pt as it enters the trench (~4nm/1μm) is still substantially less than that observed for the as-deposited Pt surfaces (~3nm/0.050μm), and thus a far less pronounced effect of the topography on the packing of monolayers in this region is still expected.

The other observable feature in Figure 5-10 (a) and (b) is a second trench-like (though less continuous) line of defects running parallel to the first, but ~2.0-

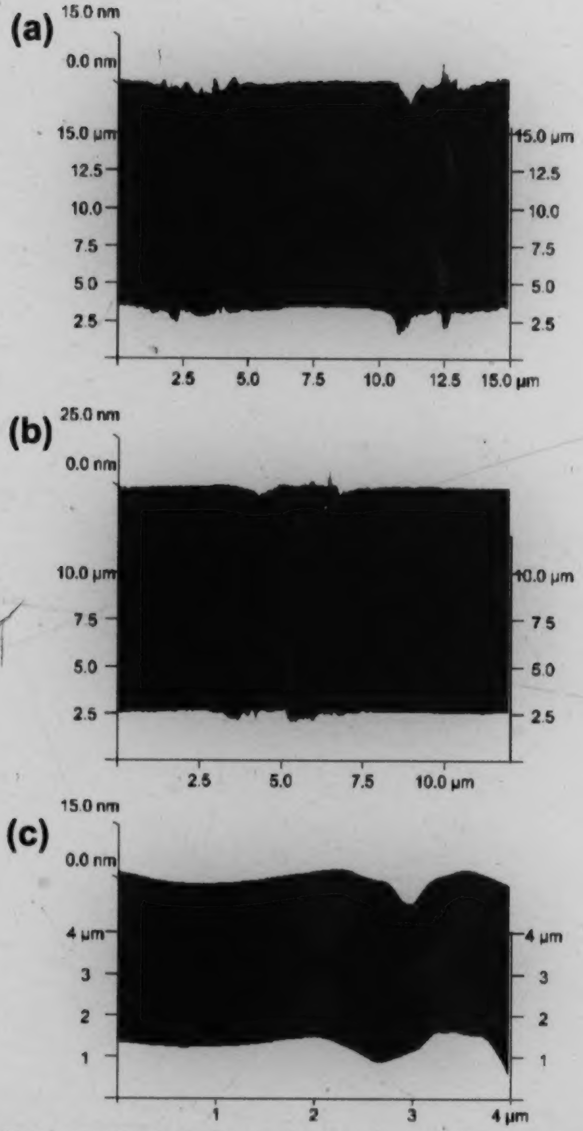

Figure 5-10 Tapping mode atomic force microscopy images of a patterned template-stripped Pt micron-scale wire with a surrounding alumina surface matrix. The images are: (a) a $(25\mu m)^2$ image of the full width of the 8um wide pTS Pt wire; (b) a $(12\mu m)^2$ image of the boundary between the ultra-flat TS Pt (left) and the surrounding alumina (right); and (c) a $(4\mu m)^2$ image of the boundary between the ultra-flat TS Pt (left) and the surrounding alumina (right).

2.5µm further into the surrounding alumina matrix. This second trench was not observed in Figure 5-8 for the pTS Pt in an Au matrix. Careful consideration led to the conclusion that this second trench is likely due to mechanical strain during the template stripping procedure. The adhesion of the Al to the fluoroalkylsilane releasing-layer — while still low enough to allow stripping — is higher than that of the Pt to the silicon oxide surface, probably due to a small number of remaining defects in the SAM releasing-layer. When mechanical stripping begins, it is probable that the pTS Pt lifts off easier than the surrounding alumina matrix and creates a strain at the boundary between the two regions. This alumina could be sufficient to cause the observed crack or trench in the alumina/silica matrix.

Contact mode AFM (CM-AFM) was employed to provide a second examination of the pTS Pt surface, and examine in particular the second row of defects. Shown in Figure 5-11 are the topography and friction images of a different 8 μm wire. The AFM topography scan in Figure 5-11 (a) shows more clearly than the TM-AFM images that the second row of defects is actually a non-linear crack running along side the linear trench at the pTS Pt-alumina boundary. The crack is accompanied by pits ~2 nm deep and ~100 nm in diameter on the far side of the crack from the pTS Pt wire; the friction image in Figure 5-11 (b) highlights the pits more clearly. This friction image also demonstrates that the region of alumina next the pTS Pt is relatively smooth (as expected from the earlier demonstration of TS Al in subsection 5.1.2), and only becomes significantly rougher near the crack and potmarks. The friction image also further emphasizes the smoothness of the Pt wire surface. While this imaging does not provide conclusive evidence that the crack is caused by mechanical strain in the template-stripping process, this seems the most plausible explanation.

Both the TM- and CM-AFM demonstrate that this crack and the associated roughness occurs ≥1 μm into the alumina, and away from the pTS Pt edge. Accordingly, as these defects are in the surrounding insulating matrix and small enough in scale that they do not reach the pTS Pt surface, they are not expected to significantly impact on the behaviour of devices formed on top of the pTS Pt features. Both AFM characterizations also demonstrate that, even with the small trench at the edge of the wires, the pTS Pt wires are coplanar with the surrounding matrix. Planarized devices have significant advantages in the fabrication of

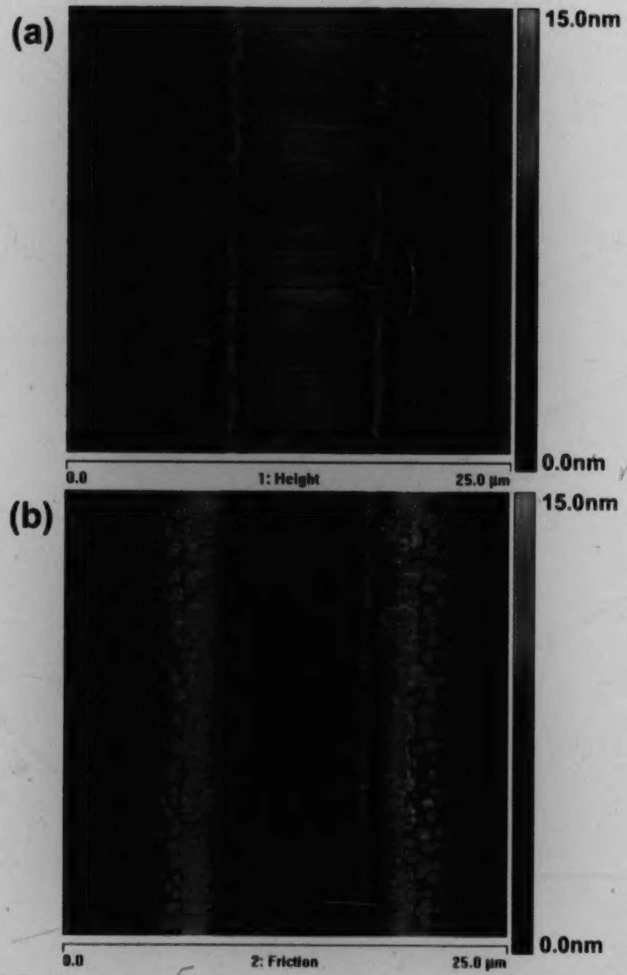

Figure 5-11 Contact mode atomic force microscopy (a) topography and (b) friction images of a patterned template-stripped Pt micron-scale wire with a surrounding alumina surface matrix.

nanoscale electrical devices as they avoid issues of large steps edges causing non-uniformity in the device behaviour.

References

(1) Wasserman, S. R.; Whitesides, G. M.; Tidswell, I. M.; Ocko, B. M.; Pershan, P. S.; Axe, J. D. *Journal of the American Chemical Society* **1989**, *111*, 5852-5861.

(2) Wasserman, S. R.; Tao, Y. T.; Whitesides, G. M. *Langmuir* **1989**, *5*, 1074-1087.

(3) Geer, R. E.; Stenger, D. A.; Chen, M. S.; Calvert, J. M.; Shashidhar, R. *Langmuir* **1994**, *10*, 1171-1176.

(4) Banga, R.; Yarwood, J. *Langmuir* **1995**, *11*, 4393-4399.

(5) Durfor, C. N.; Turner, D. C.; Georger, J. H.; Peek, B. M.; Stenger, D. A. *Langmuir* **1994**, *10*, 148-152.

(6) Hozumi, A.; Ushiyama, K.; Sugimura, H.; Takai, O. *Langmuir* **1999**, *15*, 7600-7604.

(7) Bunker, B. C.; Carpick, R. W.; Assink, R. A.; Thomas, M. L.; Hankins, M. G.; Voigt, J. A.; Sipola, D.; de Boer, M. P.; Gulley, G. L. *Langmuir* **2000**, *16*, 7742.

(8) Pellerite, M. J.; Wood, E. J.; Jones, V. W. *Journal of Physical Chemistry B* **2002**, *106*, 4746.

(9) Ulman, A. *Introduction to Ultrathin Organic Films*; Academic Press: San Diego, CA, 1991.

(10) Dulcey, C. S.; Georger, J. H.; Krauthamer, V.; Stenger, D. A.; Fare, T. L.; Calvert, J. M. *Science* **1991**, *252*, 551-554.

(11) Tsukruk, V. V.; Luzinow, I.; Julthongpiput, D. *Langmuir* **1999**, *15*, 3029-3032.

(12) As described by ASTM D3359-02 Standard Test Methods for Measuring Adhesion by Tape Test.

(13) Irikura, K. K.; Beauchamp, J. L. *Journal of the American Physical Society* **1991**, *113*, 2769-2770.

(14) Belgued, M.; Pareja, P.; Amariglio, A.; Amariglio, H. *Nature* **1991**, *352*, 789-790.

(15) Irikura, K. K.; Beauchamp, J. L. *Journal of Physical Chemistry* **1991**, *95*, 8344-8351.

(16) Belgued, M.; Amariglio, A.; Pareja, P.; Amariglio, H. *Journal of Catalysis* **1996**, *159*, 441-448.

(17) Belgued, M.; Amariglio, A.; Pareja, P.; Amariglio, H. *Journal of Catalysis* **1996**.

(18) Estimates of the consumption of aluminium into alumina, in the ambient conditions of the laboratory in which the experiments were conducted, were provided by personal correspondence with Manish Sharma (HP Labs).

Chapter 6: Ultra-flat Carbon Surfaces

6.0 Introduction

Due to a number of advantageous properties, carbon materials have been commonly employed in electroanalysis, electrocatalysis and electrosynthesis.[1-3] In recent years, attention has been drawn to the fabrication of low-cost, disposable, carbon film electrodes for mass-scale use as electrochemical sensors,[4-7] and in molecular electronics.[8-13]

Relatively thick carbon films are commonly prepared by printing from commercial carbon ink.[5, 14-16] These types of films often yield widely varying electrochemical reactivity due to binding polymers and other adhesion promoters present in the variety of carbon inks used.[7] Several methods have been reported for the fabrication of carbon thin-films (≤400 nm), including chemical vapour deposition (CVD) of carbon containing gases,[17, 18] sputtering,[19-22] electron-beam (e-beam) evaporation[23, 24] and the pyrolysis of polymeric thin films.[25-29] In general, these thin films are highly pure carbon, contain some graphitic microstructure, are easily mass-produced and yield electrochemical reactivity comparable to glassy carbon (GC). Similarly to the conventionally prepared metal films discussed in Chapters 1 and examined in Chapter 2, however, many of the conventionally prepared carbon films demonstrate significant surface roughness. Such surface roughness can be a significant factor in device applications such as electrochemical sensing and molecular electronics.

As evaporated carbon films demonstrate low adhesion to silicon-oxide surfaces, the production of TS carbon surface using the techniques presented in Chapter 2 was originally considered. However, trial experiments revealed that the electron-beam (e-beam) evaporation of carbon onto ultra-flat silicon wafers with the native oxide removed, generated well-adhered carbon films. Furthermore, characterization of the films revealed that the carbon surfaces retained the ultra-flatness of the underlying silicon. The direct interfacing of the ultra-flat carbon surfaces with silicon is of great advantage for sensing and electronics applications, and thus attention was focused on characterization of these *e-beam deposited carbon films* (ECFs).

In Section 6.1, the fabrication of the high purity carbon films using e-beam evaporation is presented. As recent literature[27] has demonstrated that the pyrolysis of carbon films at temperatures ≥1000°C in oxygen free, hydrogen-containing atmosphere improves electrochemical performance, ECFs are examined both immediately after e-beam deposition and after undergoing a post-deposition pyrolysis process.

The physical characterization of the ECFs, both non-pyrolyzed and pyrolyzed, is presented in Section 6.2. AFM reveals that, after an initial film seeding stage, the nanoscale surface roughness of the non-pyrolyzed ECF surfaces increases gradually with carbon film thickness, while still remaining exceptionally smooth up to a carbon thickness of 200 nm. Furthermore, the non-pyrolyzed ECFs are shown to have an amorphous carbon structure using Raman spectroscopy. Examination of the pyrolysed ECFs with Raman spectroscopy reveals the formation of graphitic structure inside the ECFs, which is correlated with an increase in the nanoscale roughness of the surfaces observed by AFM.

Data on the electrochemical reactivity of the ECFs are also succinctly presented in Section 6.2, and compared to GC and other types of carbon thin films. The data demonstrate that the ECFs have excellent electrochemical properties relative to conventionally employed carbon surfaces. These data were collected by the McDermott Group (Chemistry Department, UofA) in a collaborative research effort.

Section 6.3 lastly demonstrates the patterning of e-beam evaporated carbon features using conventional electron-beam lithography. For the first time, to the best knowledge of the author, amorphous carbon features on silicon of only 50 nm are demonstrated. The straightforward incorporation of nanoscale patterning into the ECF fabrication scheme reveals the potential utility of the e-beam carbon process for nanoscale device applications.

6.1 Fabrication of Ultra-flat Carbon Films on Si

Highly doped, <100> oriented, prime silicon wafers (N-type, Arsenic doped; resistivity ≤40 Ω·μm; Silicon Valley Microelectronics) were diced into 1.5 × 1.5 cm sized substrates. The substrates were dipped in piranha solution (3:1 (v/v) conc. H_2SO_4/30% H_2O_2), for 15 minutes to remove any organic surface contaminants. The native thermal oxide layer was then stripped from silicon the wafers by immersion in 49% HF for exactly 1 minute. Following a thorough rinse with deionised water and drying with nitrogen gas, the samples were loaded directly into the evaporation vacuum chamber.

The vacuum chamber evacuated to a pressure of $\sim 1\times10^{-6}$ torr before evaporations and did not rise above 5×10^{-6} torr during the deposition. A high purity polycrystalline graphite source was located 17 in. from the sample holder. Evaporation rates were monitored with a quartz crystal microbalance. The beam current was adjusted to attain a deposition rate of 1 Å/sec prior to opening the shutter between the sample and the source and occasionally fluctuated between the values of 0.5-2.5 Å/sec throughout all evaporations. After evaporation, the samples were allowed to cool in vacuum for upwards of 1 hour before the chamber was vented to nitrogen.

After removal from the chamber non-pyrolyzed samples were characterized immediately with no further processing. For pyrolyzed films, samples were placed in a tube furnace and the atmosphere was flushed by forming gas (95% N_2 + 5% H_2). The gas flow was maintained at 100 sccm while the temperature was increased at the rate of 2°C/minute up to 1000°C, held at 1000°C for 1.5 hours and then cooled to room temperature. The forming gas was kept flowing until the samples cooled to room temperature.[27]

Evaporated carbon films are known to have poor adhesion to many clean surfaces.[24] For example, poor adhesion was observed to the internal glass and stainless steel in the evaporation chamber. Commonly, secondary layers of materials such as titanium are deposited to promote adhesion of the carbon films to the underlying substrate.[21] The adhesion of the ECFs was tested by the tape test describe in ASTM D3359-02 Standard Test Methods for Measuring Adhesion by Tape Test. This test consists of pressing an adhesive tape onto the surface of a film and then pulling the tape away; poorly adhered films will peel away from the substrate with the tape, whereas well-adhered films will be undisrupted. The ECFs prepared as described above demonstrated strong adhesion between the carbon and the oxide-free silicon.

This strong adhesion is attributed to the formation of a thin silicon-carbide (SiC) layer at the interface between the film and the silicon substrate. The formation of this layer upon electron-beam evaporation of carbon directly onto an oxide-free silicon surface has been previously observed and studied by X-ray photoelectron spectroscopy (XPS).[30] Note that, immediately prior to loading, the silicon substrates were immersed in hydrofluoric acid, stripping away the native silicon-oxide layer, and generating a hydrogen-terminated Si surface. Carbon is thus evaporated onto an oxide free silicon, surface allowing direct interaction with hydrogen-terminated silicon. The flux of carbon atoms likely desorbs the surface hydrogen to form a SiC layer. Based on the data previously presented in literature,[30] the thickness of the SiC is anticipated to be on the order of one nanometer.

The SiC layer responsible for the observed adhesion was also expected to provide good electrical contact between the ECFs and the underlying conductive silicon, based on the observed electrical properties of silicon carbides.[31] The sheet resistance for both freshly HF cleaned silicon substrates and all ECFs were measured using the 4-probe technique. Independent of carbon thickness (or even the presence of carbon), the sheet resistance was measured to be $0.04\ \Omega/\square$, equating to a resistivity of $20\times10^{-4}\ \Omega\cdot\text{cm}$ for the silicon substrate thickness of 500 μm. This value is in excellent agreement with the supplier specifications for the resistivity of the doped silicon substrates, indicating that the flow of electrical current through the ECF samples is dominated by paths through the silicon. These data demonstrated that good electrical contact between the ECFs and the underlying silicon was indeed being established.

The quartz crystal used to monitor the rate of deposition was also used to determine the final thicknesses of the deposited carbon films. For several non-pyrolyzed samples, AFM was used to confirm that the quartz crystal values were accurate. The AFM measurements were carried out using both Multimode and Dimension 3000 microscopes from Digital Instruments (Santa Barbra, CA). In all cases, AFM images were collected in contact mode with scan rates of 1-5 Hz using commercial Si_3N_4 cantilevers (k = 0.6 nN/nm; ThermoMicroscope). Non-pyrolyzed samples were examined immediately after removing the samples from the evaporation chamber, and pyrolyzed samples were examined after removal from the furnace. For thickness measurement, images were collected at the boundary between the film and the region blocked by the clip used to hold the substrate in place.

The thicknesses reported by the crystal agreed with AFM measured thickness to within 5%. The thicknesses quoted throughout this chapter are those measured by the quartz crystal monitor. AFM was also used to measure the thickness of several pyrolyzed samples. These thicknesses were compared against the AFM thickness values of non-pyrolyzed samples prepared in the same evaporation run; pyrolysis generated no observable change in the thickness. This is notable because pyrolysis of photoresist films under similar conditions results in large reduction of mass,[27] indicating the loss of material during the pyrolysis process.

6.2 Properties of Ultra-flat Carbon Surfaces

6.2.1 Physical Characterization

Non-pyrolyzed ECFs, over a range of carbon thicknesses, were examined using AFM to determine how increasing deposition thickness influences nanoscale surface morphology of the surfaces. The AFM measurements were carried out on both Multimode and Dimension 3000 microscopes from Digital Instruments (Santa Barbra, CA). AFM images were collected in contact mode with scan rates between 1 Hz and 5 Hz, using commercial Si_3N_4 cantilevers (ThermoMicroscope). Non-pyrolyzed samples were examined immediately after removing the samples from the evaporation chamber, and pyrolyzed samples were examined after removal from the furnace. At least 5 measurements from randomly selected points across each sample were averaged to obtain the RMS roughness values provided below. At least one other sample of each thickness was also examined to ensure the observed behaviours were reproducible.

Shown in Figure 6-1(a) are the AFM determined root-mean-square (RMS) roughness values determined from image sizes of $(100\text{nm})^2$ and $(1\mu\text{m})^2$. The RMS values of all the films 7 nm and thicker are between 0.7 Å and 1.1 Å. These values are very close to the 0.6 Å RMS roughness measured over both length scales for the underlying silicon <100> surface. The slightly higher roughness of the 2 nm films, particularly at the larger scan size, is likely due to initial SiC island formation on the surface, prior to complete coverage.

Figure 6-1(b) compares the roughness of post-deposition-pyrolyzed to non-pyrolyzed ECFs of 7 nm and 200 nm thickness. From the results, pyrolysis of the films results in a considerable increase in roughness at both length scales. This increase in roughness is correlated with the Raman results (presented below) demonstrating increased graphitization with pyrolysis; the formation of independently oriented graphitic domains in the films can be expected to disrupt the originally flat surface. Despite the increased roughness, however, the actual values of between 3 Å and 6 Å still represent an exceedingly flat surface. The RMS values for the pyrolyzed ECFs are similar to those measured at PPF

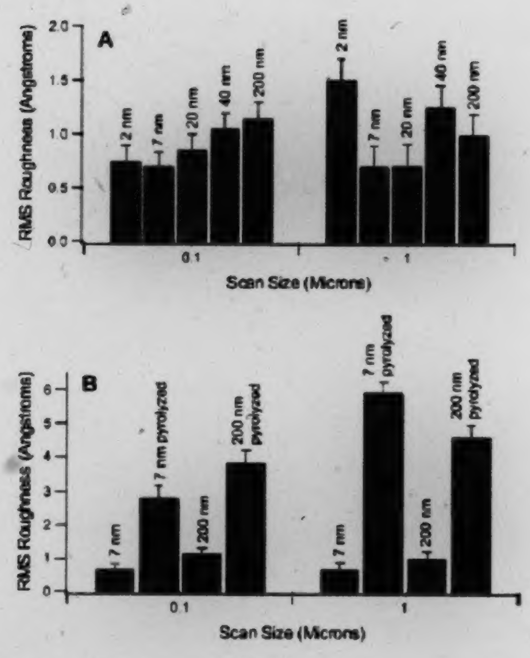

Figure 6-1 Bar graphs of SFM measured RMS roughness as a function of image size. **(A)** Results from a variety of films thickness for non-pyrolyzed films. **(B)** Results for 7 and 200 nm films before and after pyrolysis.

surfaces, which are pyrolyzed under similar conditions.[28] Several images were also collected on samples at length scales up to and exceeding dimensions of (10μm)^2. The roughness measured in these images was similar to that of the (1μm)^2 scans, demonstrating the electrode flatness extends over a long-range and is not a local effect.

To better illustrate the topography of the ECF surfaces, Figure 6-2 presents contact-mode AFM images for 7 nm and 200 nm thick ECFs, with image sizes of both (100nm)^2 and (1μm)^2. Note that the black-to-white vertical scale on these images is only 5 nm. The left column displays images of non-pyrolyzed samples {(a), (b), (e) and (g)} whereas the right column displays the respective images for the post-deposition-pyrolyzed samples {(b), (d), (f) and (h)}.

The non-pyrolyzed films exhibit an extremely flat and featureless topography over both length scales presented. Pyrolysis of the films results in a more textured surface, as reflected by the RMS values in Figure 6-1(b). Comparing the

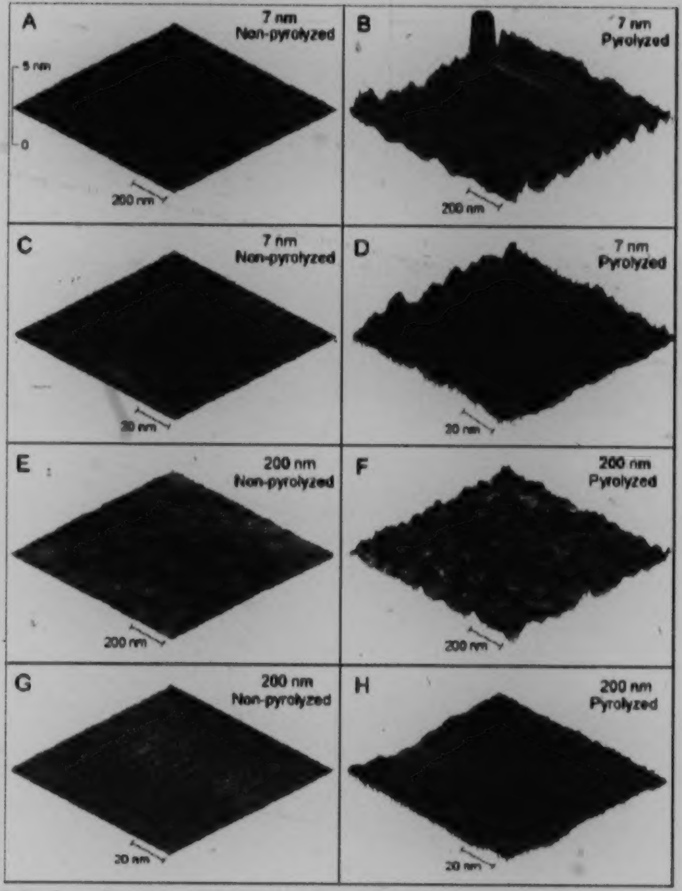

Figure 6-2 Surface plot presentation of contact mode AFM imaged of ECFs. The z-scale bar in A applies to all images. **(A)** 1 × 1 μm^2 image of a non-pyrolyzed 7 nm film. **(B)** 1 × 1 μm^2 image of a pyrolyzed 7 nm film. **(C)** 100 × 100 nm^2 image of non-pyrolyzed 7 nm film. **(D)** 100 × 100 nm^2 image of a pyrolyzed 7 nm film. **(E)** 1 × 1 μm^2 image of a non-pyrolyzed 200 nm film. **(F)** 1 × 1 μm^2 image of a pyrolyzed 200 nm film. **(G)** 100 × 100 nm^2 image of a non-pyrolyzed 200 nm film. **(H)** 100 × 100 nm^2 image of a pyrolyzed 200 nm film.

(1μm)^2 images of non-pyrolyzed ECFs to the pyrolyzed {7nm: (a) and (b), 200nm: (e) and (f)}, features with lateral dimensions in the hundreds of nanometers and heights of 1-2 nm are observed to develop due to pyrolysis. In the higher resolution (100nm)^2 images {7 nm: (c) and (d), 200 nm: (g) and (h)}, vertical variations of <1 nm occur smoothly over a smallest lateral length scale of tens of nanometers.

Raman spectroscopy was employed to probe the microstructure of the ECFs. The Raman spectroscopy was conducted on ECF samples prepared by the author, as described in Section 6.1, and sent to Aletha M. Nowak and Richard L. McCreery at Ohio State University. Spectra were collected with a line-focused f/2 Raman spectrometer (Chromex) and a back-thinned CCD (Andor), described previously.[32] A 514.5 nm Argon ion laser (Coherent) with a power of 50 mW at the sample was used. The laser was incident on the sample at 45° and collection at 0° with respect to the surface normal. The focal line was approximately 5 mm x 50 μm and was generated by a Powell lens (Lasiris, P-5°, Lasiris, Inc., Quebec). Integration time was 30 seconds for the 200 nm ECF films and 120 seconds for the 7 nm ECF films. Spectra are displayed as an average of 10 integrations. Spikes in CCD integrations were removing by comparing successive spectra and rejecting intensities that exceeded those in previous spectra by more than 200 CCD digitizer units.

Representative results in the 1000 to 2000 cm^{-1} region are shown in Figure 6-3. Figure 6-3 (a) contains Raman spectra for 7 nm ECFs before and after pyrolysis at 1000°C for 1 hour. In both spectra, the intense band at ~1000 cm^{-1} is due to the Si substrate. A number of bands characteristic of Si are observed below 1000 cm^{-1} due to the large penetration depth of the Ar^{+} laser (~25 nm) relative to the carbon film thickness. The spectrum of the 7 nm non-pyrolyzed EDF shows a broad feature cantered at ~1500 cm^{-1} that is diagnostic of amorphous carbon. This Raman spectrum is qualitatively similar to those in previous reports of carbon films deposited at room temperature by e-beam evaporation[33] and sputtering.[21] Following pyrolysis, distinct bands appear that are characteristic of a graphitic structure. The band at 1605 cm^{-1} is assigned as the G band commonly observed in graphitic material. The position of this band in Figure 6-3 (a) is blue shifted from the position of this band in graphite (~1582 cm^{-1}) as has been observed for carbon films with extremely small microcrystallite size.[34] Also observed is the D band at 1354 cm^{-1} that is diagnostic of disorder in carbon materials.[35] Thin carbon films formed by pyrolysis of photoresist layers also exhibit G and D bands for pyrolysis

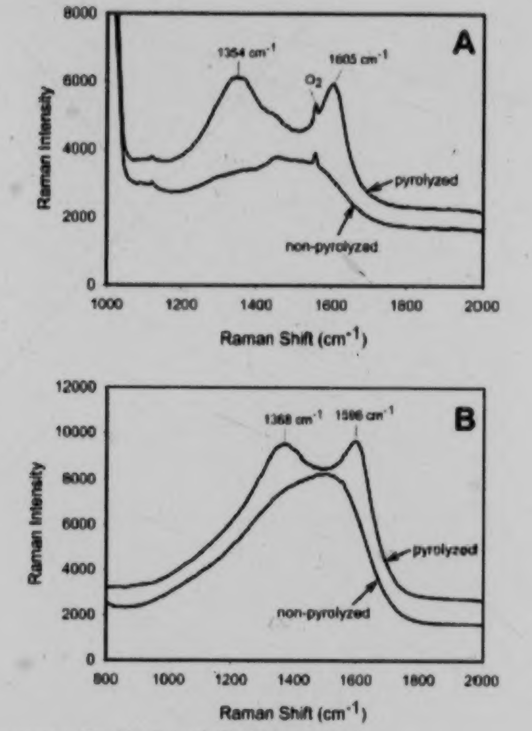

Figure 6-3 Raman spectra for **(A)** 7- and **(B)** 200-nm ECF.

temperatures over 600°C. The poor resolution of the G and D bands in Figure 6-3 (a) and the D/G intensity ratio of ~1 also imply that, although pyrolysis results in some graphitization, the carbon layer comprising the pyrolyzed 7 nm ECFs is still a highly disordered material.

Raman spectra for 200 nm ECFs are shown in Figure 6-3 (b). In this case, the thickness of film is sufficient to shield Raman scattering from the Si substrate. Qualitatively, the results for the 200 nm films are identical to those for the 7 nm films. That is, the non-pyrolyzed ECFs exhibit an amorphous structure. Pyrolysis of the films at 1000°C induces limited graphitization and results in a film with a disordered, poly-graphitic structure.

6.2.2 Electrochemical Characterization

The electrochemical examination of ECFs prepared by the author, as described in Section 6.1, was carried out by Abbas A. Rostami and Mark T.

McDermott, in the McDermott Research Group (Dept of Chemistry, UofA). The redox species examined were chosen to probe the various structural and chemical aspects that have been shown to be important at carbon electrodes.[2, 36] For the complete electrochemical characterization of the ECFs, readers are directed to a recent publication by Blackstock *et al.*[37] This subsection summaries relevant results of the collaborative electrochemical investigation of the ECFs.

Prior to electrochemical experiments, all samples were sonicated in a mixture of 50:50 (v/v) 2- propanol/acetonitrile with an equal volume of activated carbon for 10 min. The electrodes were then sonicated in deionised water (Nanopure, 18 MΩ) for 10 min. Electrochemical measurements were performed using a computer-controlled bipotentiostat (model AFCBP1; Pine Instruments). A three-electrode cell was used with Ag/AgCl/KCl (sat) as reference electrode and a Pt wire as a counter electrode. The surface area of working electrode was defined by an elastometric O-ring and electrochemically determined to be 0.35 ±0.01 cm^2.

ECFs were immersed in 10 μM 2,6-AQDS (1M $HClO_4$) and voltammograms were collected after the adsorbed layer had reached equilibrium with the contacting solution (~10 minutes). In all cases, near ideal voltammetric waves characteristic of an adsorbed redox species are observed. Overall, all ECFs examined yielded voltammetry for both solution bound and adsorbed species that was qualitatively similar to that observed at GC. The results from 2,6-AQDS adsorption experiments are summarized in Table 6-1; at the bottom of the table, results for glassy carbon (GC) substrates are provided for comparison. Whereas non-pyrolyzed ECFs demonstrate 2,6-AQDS adsorption of only 28-30 $pmol/cm^2$, pyrolysis leads to the adsorption of >100 $pmol/cm^2$ on the ECF surface. The theoretical saturation coverage for 2,6-AQDS adsorbing with rings parallel to a flat surface is 132 $pmol/cm^2$.[38] These data indicate that pyrolysis leads to an increase in adsorption sites, which is again attributed to the partial graphitization of the ECF.

The electrode capacitance values (C^o) reported in Table 6-1 were obtained from cyclic voltammograms in 1 M KCl at a variety of scan rates (0.1 to 5 V/s). In all cases, background current in cyclic voltammograms and measured C^o values at ECFs are lower than GC. This is predominantly due to the significantly smoother surface of the ECFs. The capacitance at the 200 nm films is very similar to that of a smooth Hg surface (~20 μF/cm^2), evidencing the ultra-flatness of the ECFs demonstrated by AFM in the previous subsection.

Surface	$\Gamma_{2,6\text{-AQDS}}$ (pmol/cm^2) (1 M $HClO_4$)	C^o (μF/cm^2) (1 M KCl)	k^o (cm/s)[a] $Fe(CN)_6^{3-/4-}$ (1 M KCl)
7 nm	28	17 ± 3 (N = 3)	2.7×10^{-3} (15%)[b]
7 nm (py)	105	14 ± 2 (N = 4)	1.4×10^{-2} (25%)
200 nm	30	21 ± 8 (N = 3)	5.7×10^{-3} (17%)
200 nm (py)	123	25 ± 1 (N = 4)	2.9×10^{-2} (14%)
Polished GC	172[c]	41[c]	8×10^{-3} (25%)[c]

a. All k° values were determined from ΔE_p values corrected for iR_u error and from 5-15 different scan rates per sample.

b. Values in parenthesis are the relative standard deviation of the mean for 2-4 different films.

c. From reference [39]

d. This work

Table 6-1 Summarized electrochemical characterization of for ECFs. Complete characterization can be found in Blackstock *et al.*[37]

The electron transfer (ET) rates for $Fe(CN)_6^{3-/4-}$ were also measured for 7 nm and 200 nm, non-pyrolyzed and pyrolyzed ECFs, and the results are again summarized in Table 6-1. Poor reproducibility of ET rates (k°) is observed on the non-pyrolyzed ECFs, as evidenced by their large relative standard deviations (RSD). Pyrolyzed ECFs exhibit RSD values as good, or better than, polished GC in most cases. The magnitude of k° for $Fe(CN)_6^{3-/4-}$ at the non-pyrolyzed films is comparable to that observed at GC. Pyrolysis of the films increases the ET rates for both ECF film thickness by a factor of ~5. This enhancement in ET reactivity is again attributed to the graphitization induced by pyrolysis. $Fe(CN)_6^{3-/4-}$ ET rates for a number of different types of carbon thin films are presented in Table 6-2, enabling a direct comparison of the surfaces. This table shows that the pyrolyzed 200 nm ECFs yield among the highest rates measured at thin carbon film electrodes.

Type of Film	k^o for $Fe(CN)_6^{3-/4-}$ (cm/s)	Reference
e-beam deposited on glass (28 nm)	$1.2 \times 10^{-3,a}$ (1 M KNO_3)^b	23
Pyrolyzed on Macor	$3.8 - 15.4 \times 10^{-3}$ (1 M KCl)	25
Sputtered	$2.4 - 4.2 \times 10^{-2}$ (0.5 M H_2SO_4)	21
CVD of natural gas on quartz	1.6×10^{-3} (0.1 M KNO_3)	17
CVD of ethane on GC	5×10^{-3} (1 M KCl)	18
Pyrolyzed negative photoresist	$1.8 \times 10^{-2,a}$ (1M KNO_3)	29
PPF	1.2×10^{-2} (1 M KCl)	28
Pyrolyzed 200 nm ECF	2.9×10^{-2} (1M KCl)	This work

a. Calculated from reported ΔE_p values.
b. Electrolyte solution used.

Table 6-2 Comparison of $Fe(CN)_6^{3-/4-}$ ET kinetics at various carbon film electrodes.

6.2.3 Discussion

Several techniques have been reported in the literature for preparing thin carbon films. Examples of these include thermal decomposition of gaseous precursors[17], e-beam evaporation[23, 24, 30, 33, 34], vacuum sputtering[21, 22] and pyrolysis of thin films of polymers[25, 27-29]. While films prepared by a number of procedures have been examined as electrodes, the electrochemical performance of films deposited by e-beam evaporation has not been thoroughly studied. The application of e-beam deposited carbon films for use as optically transparent electrodes was reported a number of years ago.[23, 24] These films, deposited on glass or quartz, had two significant shortcomings as electrodes; poor adhesion to the substrate and high electrode resistance. The electrode fabrication technique presented here overcomes these difficulties. Specifically, the use of highly doped silicon, without an oxide layer, as the substrate overcomes the previous challenges with both film adhesion and poor film conductivity. The strong interaction between the carbon and oxide free Si form an interfacial SiC layer[30] that both increases adhesion and promotes good electrical contact between the conductive substrate and the carbon film.

The SFM studies of the ECF surfaces demonstrated exceptional flatness, with RMS roughness values around 1 Å for the non-pyrolyzed films, which is comparable to the flatness of the underlying silicon. Although the composition of extremely flat non-pyrolyzed surfaces is amorphous carbon, they exhibit reasonable electrochemical reactivity. Two previous studies on e-beam carbon films deposited at room temperature have reported higher roughness values of 0.8nm [33] and >1nm,[34] though both studies used silicon with a surface oxide layer. As stated previously, carbon films demonstrate poor adhesion to glass and other silicon-oxide surfaces. A low carbon-substrate interaction leads to a high surface mobility for carbon atoms on the silicon-oxide substrate, allowing the atoms of the carbon film seed-layers to cluster into islands. The low roughness of the ECFs is attributed to the strong adhesion of the carbon to the oxide free Si<100> substrate. The strong adhesion results in substantially lower surface mobility, and thus in more uniform carbon seed-layers . Once the carbon seed-layers are established, the strong carbon-carbon interaction severely limits further mobility of carbon atoms, leading to roughness values growing only marginally with increasing evaporation thickness, as shown in Figure 6-1(a). Pyrolysis of ECFs at 1000°C induces limited graphitization and increases the RMS roughness to 0.4-0.6 nm. Although rougher than non-pyrolyzed ECFs, these films are still extremely flat, and comparable to the conventionally employed pyrolyzed photoresist films (PPF), recently reported to have an RMS roughness of <1nm.[27, 28]

6.3 Nanoscale Patterning of ECFs

Having respectively presented the fabrication and characterization of large-area, ultra-flat ECFs in Sections 6.1 and 6.2, this section turns to the nanoscale patterning of ECFs. The patterning demonstrated herein was accomplished using standard electron-beam lithography (EBL) techniques and the Raith electron-beam pattern writer in the University of Alberta's Nanofabrication Facility (UofA Nanofab).

The substrates employed for this process were prime polished, $(1\text{cm})^2$ Si <100> wafers with a native thermal oxide layer (P-type; Boron doped; 1-20 Ω·cm; Silicon Valley Microelectronics, CA). The EBL resist deposition, writing of the nanoscale pattern using the Raith EBL pattern writer and post-writing development of the EBL resist were all conducted by Mirwais Akatary at the UofA Nanofab, prior to the substrates being delivered to the author.

Prior to use, the substrates were treated to a 1-2 sec O_2 plasma (100 mTorr and 100W), in order to remove any residual resist and/or organic contamination from the bottom of the nanoscale patterns opened in the resist. Once out of the O_2 plasma chamber, the substrates were dipped in a 5% hydrofluoric acid (HF) solution for ~5 sec in order to remove the native silicon-oxide at the bottom of the opened nanoscale patterns in the resist. Immediately after removal from the HF solution, the substrates were rinsed copiously in de-ionized water, removing any remaining HF and preventing over-etching of the oxide. Exposure of the substrates for longer than these prescribed periods to either the O_2 plasma or the HF resulted in over-etching of the resist layer or native silicon-oxide, respectively, which degraded the quality of the final patterned features obtained.

When the substrates were rinsed with de-ionized water and dried under a stream of nitrogen, they were loaded to the high vacuum e-beam evaporator system and pumped down. The exposure time to ambient conditions between drying and loading into the evaporation chamber was kept below 30 minutes. The evaporation chamber was pumped down to a base pressure of $\leq 10^{-6}$ torr and did not rise above 5×10^{-6} torr during the deposition. The evaporations were conducted as described Section 6.1, with an average deposition rate of 1 Å/sec.

The carbon film thickness used for all the patterned samples demonstrated in this section was ~500Å. After evaporation, the samples were allowed to cool in vacuum for upwards of 1 hour before the chamber was vented to nitrogen.

After removal from the vacuum chamber, the substrates were placed directly in acetone and sonicated for upwards of 30 minutes to remove the resist and excess carbon. Inspection under an optical microscope every 5 minutes revealed the resist lifting-off, leaving behind only the patterned carbon features that were deposited directly onto the HF cleaned silicon surface. Once all the resist appeared lifted-off under the optical microscope, the samples were transferred to a scanning electron microscope (SEM) for a more detailed inspection of the remaining carbon pattern

Shown in Figure 6-4 is an array of e-beam evaporated carbon nanowires fabricated using this process; the wires are ~50 nm in diameter and with a centre-to-centre pitch of ~200 nm. Lithographic patterning of micron-sized features using conventional photolithography was also conducted with equal success, demonstrating the ease with which the carbon e-beam evaporation fabrication technique can be adapted to conventional lithographic techniques to provide patterns of any desired size scale and design.

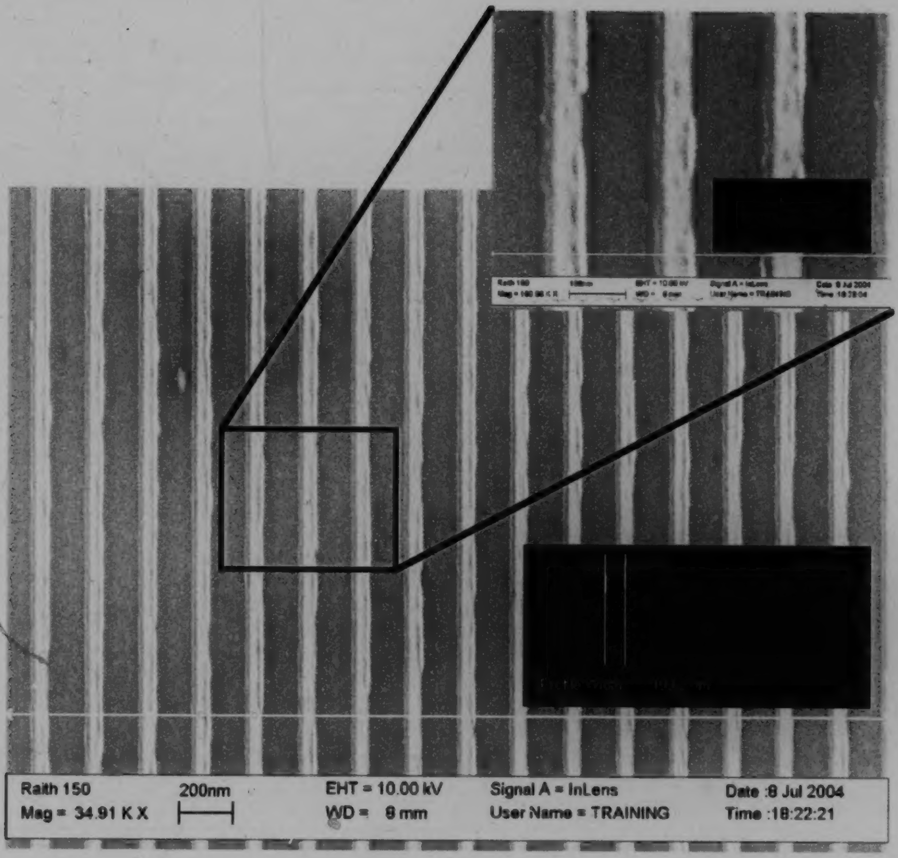

Figure 6-4 An array of nanoscale carbon wires, ~50nm in width with a pitch of ~200nm, fabricated using conventional EBL techniques and the e-beam evaporation technique presented in this chapter.

References

(1) Kinoshita, K. *Carbon: Electrochemical and Physicochemical Properties*; Wiley: New York, 1988.

(2) McCreery, R. L. In *Electroanalytical Chemistry*; Bard, A. J., Ed.; Marcel Dekker: New York, 1991; Vol. 17, pp 221-374.

(3) McCreery, R. L. In *Interfacial Electrochemistry*; Wiekowski, A., Ed.; Dekker: New York, 1999, pp Chapter 35.

(4) Alvarez-Icaza, M.; Bilitewski, U. *Analytical Chemistry* **1993**, *65*, 525A.

(5) Hart, J. P.; Wring, S. A. *Electroanalysis* **1994**, *6*, 617-624.

(6) Lindner, E.; Buck, R. P. *Analytical Chemistry* **2000**, *72*, 336A-345A.

(7) Wang, J.; Tian, B. M.; Nascimento, V. B.; Angnes, L. *Electrochimica Acta* **1998**, *43*, 3459-3465.

(8) Ranganathan, S.; Steidel, I.; Anariba, F.; McCreery, R. L. *Nano Letters* **2001**, *1*, 491-494.

(9) Solak, A. O.; Ranganathan, S.; Itoh, T.; McCreery, R. L. *Electrochemical and Solid State Letters* **2002**, *5*, E43-E46.

(10) Anariba, F.; McCreery, R. L. *Journal of Physical Chemistry B* **2002**, *106*, 10355-10362.

(11) Solak, A. O.; Eichorst, L. R.; Clark, W. J.; McCreery, R. L. *Analytical Chemistry* **2003**, *75*, 296-305.

(12) McCreery, R. L.; Dieringer, J.; Solak, A. O.; Snyder, B.; Nowak, A. M.; McGovern, W. R.; DuVall, S. *Journal of the American Chemical Society* **2003**, *125*, 10748-10758.

(13) Nowak, A. M.; McCreery, R. L. *Analytical Chemistry* **2004**, *76*, 1089-1097.

(14) Wang, J.; Pamidi, P. V. A.; Park, D. S. *Analytical Chemistry* **1996**, *68*, 2705-2708.

(15) Wang, J.; Pedrero, M.; Pamidi, P. V. A.; Cai, X. H. *Electroanalysis* **1995**, *7*, 1032-1034.

(16) Wang, J.; Pedrero, M.; Sakslund, H.; Hammerich, O.; Pingarron, J. *Analyst* **1996**, *121*, 345-350.

(17) Blaedel, W. J.; Mabbot, G. A. *Anal. Chem.* **1978**, *50*, 933-936.

(18) Eriksson, A.; Norekrans, A.-S.; Carlsson, J.-O. *J. Electroanal. Chem.* **1992**, *324*, 291-305.

(19) Sreenvas, G.; Ang, S. S.; Fritsch, I.; Brown, W. D.; Gerhardt, G., A.; Woodward, D. J. *Anal. Chem.* **1996**, *68*, 1858-1864.

(20) Fiaccabrino, G. C.; Tang, X.-M.; Skinner, N.; de Rooij, N. F.; Koudelka-Hep, M. *Sens. Act. B* **1996**, *35-36*, 247-254.

(21) Schlesinger, R.; Bruns, M.; Ache, H. J. *Journal of the Electrochemical Society* **1997**, *144*, 6-15.

(22) You, T. Y.; Niwa, O.; Tomita, M.; Ichino, T.; Hirono, S. *Journal of the Electrochemical Society* **2002**, *149*, E479-E484.

(23) DeAngelis, T. P.; Hurst, R. W.; Yacyncych, A. M.; Mark, H. B.; Heineman, W. R.; Mattson, J. S. *Analytical Chemistry* **1977**, *49*, 1395-1398.

(24) Mattson, J. S.; Smith, C. A. *Analytical Chemistry* **1975**, *47*, 1122-1125.
(25) McFadden, C. F.; Russell, L. L.; Melaragno, P. R.; Davis, J. A. *Anal. Chem.* **1992**, *64*, 1521-1527.
(26) Niwa, O.; Tabel, H. *Anal. Chem.* **1994**, *66*, 285-289.
(27) Ranganathan, S.; McCreery, R.; Majji, S. M.; Madou, M. *Journal of the Electrochemical Society* **2000**, *147*, 277-282.
(28) Ranganathan, S.; McCreery, R. L. *Analytical Chemistry* **2001**, *73*, 893-900.
(29) Singh, A.; Jayaram, J.; Madou, M.; Akbar, S. *Journal of the Electrochemical Society* **2002**, *149*, E78-E83.
(30) Luthin, J.; Linsmeier, C. *Physica Scripta* **2001**, *T91*, 134-137.
(31) Pensl, G.; Choyke, W. J. *Physica B* **1993**, *185*, 264-283.
(32) Ramsey, J.; Ranganathan, S.; McCreery, R. L.; Zhao, J. *App. Spec.* **2001**, *55*, 767-773.
(33) Schelz, S.; Richmond, T.; Kania, P.; Oelhafen, P.; Guntherodt, H. J. *Surface Science* **1996**, *359*, 227-236.
(34) Besold, J.; Thielsch, R.; Matz, N.; Frenzel, C.; Born, R.; Mobius, A. *Thin Solid Films* **1997**, *293*, 96-102.
(35) Wang, Y.; Alsmeyer, D. C.; McCreery, R. L. *Chem. Mater.* **1990**, *2*, 557-563.
(36) McCreery, R. L.; Cline, K. K.; McDermott, C. A.; McDermott, M. T. *Colloid Surf. A* **1994**, *93*, 211-219.
(37) Blackstock, J. J.; Rostami, A. A.; Nowak, A. M.; McCreery, R. L.; Freeman, M. R.; McDermott, M. T. *Analytical Chemistry* **2004**, *76*, 2544-2552.
(38) Soriaga, M. P.; Hubbard, A. T. *J. Am. Chem. Soc.* **1982**, *104*, 3937.
(39) Kiema, G. K.; Aktay, M.; McDermott, M. T. *Journal of Electroanalytical Chemistry* **2003**, *540*, 7-15.

Chapter 7: Conclusions

The research presented in this thesis concentrated on developing our scientific understanding of both the fabrication of ultra-flat thin-film material surfaces and the nanoscale properties of select ultra-flat thin-film surfaces. In the experimental chapters of the thesis (Chapters 2 through 6), ultra-flat metal, metal-oxide and organic thin-film surfaces of promise for nanoscience research and device applications were demonstrated and characterized. Specifically, the nanoscale physical and chemical properties of novel ultra-flat Pt, Pt-oxide and organic thin-film surfaces were determined, providing a foundation for the future utilization of these surfaces in research and device applications.

Throughout the experimental chapters of this thesis, a variety of potential applications for these thin-film surfaces were discussed or presented. For example, the research presented in Chapters 3 and 4 demonstrates two applications of the ultra-flat TS metal surfaces studied in Chapter 2. The final section of thesis (below) summarises the utility of the studied surfaces for a variety of ongoing and future applications. Directions for future research into the thin-film surface fabrication techniques and specific ultra-flat thin-film surfaces are also incorporated into the discussion.

7.0 Future Research and Applications

The research presented in Chapter 2 provided advancements in both the template-stripping methodology and our scientific understanding of the nano- and atomic-scale structure TS noble metal surfaces. The characterization of the TS metal surfaces — particularly of TS Pt — elucidated the ability of the surfaces to maintain the ultra-flat characteristic of the templating-silicon oxide, demonstrated the chemical purity of freshly stripped TS surfaces, and revealed the evolution of the nano- and atomic-scale structure of TS Pt surfaces with pre-stripping annealing. Furthermore, the range of techniques presented enables TS noble metal surfaces to be prepared for use in any environment where the metals themselves are stable.

With this detailed understanding of the surface properties and fabrication processes, a range of nanoscience research applications for the ultra-flat TS metal surfaces can be considered. As discussed in the Introduction to Chapter 2, TS metal surfaces were originally prepared by Hegner *et al.*[1-3] for use in the STM imaging of chemical species adsorbed on metal surfaces. Such imaging of adsorbates on TS surfaces can now be better facilitated by the *in-situ* template-stripping procedure (subsection 2.1.3); not only does the procedure allow the utilization of high resolution UHV-STM, but it also allows the exposure of the clean TS surfaces to the adsorbing chemical species to be done with great control in a UHV environment, avoiding unwanted adsorbing contaminants.

As stated above, Chapters 3 and 4 represent two further applications of the TS metal surfaces examined in Chapter 2. In Chapter 3, the TS metal surfaces are employed to explore the correlated influence of metal substrate surface roughness and intrinsic metal malleability on alkanethiol SAM packing structure. On the less malleable Pt substrates, surface roughness was shown to substantially disrupt the packing structure of alkanethiol SAMs. The observed disruption to alkanethiol SAM packing on softer Au substrates was less significant, though still evident. The research also incorporated the first detailed examination of the packing structure of alkanethiol SAMs on Pt surfaces, revealing the densely-packed alkane chains to be tilted, on average, at ~12° to the ultra-flat Pt surface normal, and a $\sqrt{3} \times \sqrt{3}$ overlayer relation of the alkanethiol molecules to the Pt atoms of the underlying <111> oriented ultra-flat surfaces.

The understanding, from Chapter 3, that SAMs on the TS metal substrates demonstrate greatly enhanced uniformity, highlights the potential utility of SAMs on ultra-flat TS surfaces in applications such as SAM-based biosensors[4-6] and molecular electronic junctions.[7-10] In these applications, highly uniform and defect free monolayers ensure greater reproducibility of device behaviour. As discussed in Chapter 1, the use of platinum is also advantageous, as it allows the direct integration of such devices with silicon electronics. Based on the presentation of the results in Chapters 2 and 3 to the scientific community, several efforts have begun to incorporate SAMs on TS surfaces into research programs in molecular electronics. Through personal correspondence and collaborations, the author is aware of such efforts at: Hewlett-Packard Laboratories; University of Minnesota; National Institute of Standards and Technology; and Sandia National Laboratories. Furthermore, a fabrication scheme for producing arrays of nanoscale molecular electronic devices using SAMs on the large-area TS Pt and TS Au surfaces has also been developed by the author, and presented at several scientific conferences.[11-13] Such nanoscale molecular electronic devices have been the focus of a collaborative molecular electronic research project between the author and the Tour Research Group at Rice University.[14]

The conductive SPM examination of the plasma produced, ultra-thin Pt-oxide layers in Chapter 4 was also enabled by the TS Pt surfaces from Chapter 2. The study of the physical and chemical properties of the oxide in Chapter 4 revealed the stratified structure of the Pt-oxide ultra-thin film, comprising two distinct platinum-oxygen compounds. The cAFM and STM examination of the ultra-thin oxide demonstrated both the semi-conducting electrical characteristics of the oxide and nanoscale lateral inhomogeneities in the oxide structure.

While the observed lateral nanoscale inhomogeneities indicate further research may be necessary into the lateral nanostructure of the Pt-oxide ultra-thin layers, the semi-conducting properties of the oxide suggest a potential application of the ultra-thin-oxide as an active component in nanoelectronic devices. The selective self-assembly of isocyanides on the Pt-oxide surfaces[15] also indicates that the Pt-oxide surfaces could be good candidate electrodes for SAM based molecular electronic devices. In fact, the ultra-thin, plasma-produced Pt-oxide layers are presently incorporated into Langmuir-Blodgett-based molecular electronic devices being researched at Hewlett-Packard Laboratories.[16-19] For all such nanoelectronics applications, as well as for potential chemical- and photo-sensing applications,[20, 21] the ultra-flatness provided by starting with TS Pt thin-film surfaces will be advantageous for ensuring reproducible device behaviour.

Beyond integration with the template-stripping techniques of Chapter 2 to produce ultra-flat Pt-oxide surfaces, the plasma-treatment of the Pt surfaces explored in Chapter 4 has potential value as a nanofabrication technique.

Evaluation of the Pt-oxide formation kinetics in Chapter 4 revealed that the O_2 plasma-treatment results in a rapid initial formation of Pt-oxide, followed by a long-time steady-state equilibrium between the processes of continuous surface etching and oxide formation. The plasma-treatment of prefabricated Pt nanostructures and nanowires, produced using techniques such as nano-imprint lithography,[16, 17] nanowire pattern transfer[22] or templated electrochemical growth,[23] could be used to transform the metallic nanostructures into core-shell metal-oxide structures. Core-shell nanowires fabricated with this process could be used for creating nanoelectronic oxide junctions via the crossing of nanowires. Alternately, functionalizing the oxide surfaces of such nanowires with molecules prior to the crossing of the nanowires would allow for the formation of nanoscale molecular electronics junctions.

The expansion of the templating-stripping methodology to incorporate releasing-layers in Chapter 5 created the opportunity for a new range of TS material surfaces, such as the demonstrated TS Al surfaces, to be explored. Limitations of the releasing-layer process were revealed with the demonstration that the evaporation of Pt onto the fluoroalkylsilanes SAMs results in the breakdown of the molecules. However, the process for generating patterned template-stripped (pTS) Pt features in an insulating alumina/silica matrix, demonstrated at the end of Chapter 5, provides opportunities for electronic device applications incorporating patterned ultra-flat TS surfaces. The pTS Pt fabrication process is presently being employed at Hewlett-Packard Laboratories to produce pTS Pt electrodes for use in molecular electronic devices.

Further expansion of the template-stripping methodology, beyond the scope of this research, has also been considered. For example, the incorporation of patterned structures on the templating silicon-oxide surfaces, aimed at generating three-dimensional structures on the TS surfaces, in presently being investigated. Devices ranging from high precision micro-scale diffraction gratings with low surface roughness, to nano-pillars or nano-pyramids for other optical or sensing applications, could potentially be fabricated using such templates.

A large range of previously unstudied TS material surfaces are also being considered for future study. As discussed in Chapter 3, palladium is similar to platinum in its compatibility with silicon electronics, making well characterized TS Pd surfaces equally appealing for electronics applications. Furthermore, the detailed characterization of alkanethiol SAMs on Pd could provide further understanding of the correlation between metal malleability and the influence of surface roughness on alkanethiol SAM structure elucidated in Chapter 3. In addition, the detailed characterization of TS Al surfaces demonstrated in Chapter 5 (enabled by the releasing-layer template-stripping technique), and oxidation of the TS Al surfaces both in ambient conditions and with O_2 plasma-treatment, could provide another ultra-flat metal-oxide surface for potential use in electronic devices.

As discussed briefly in Chapter 6, electron-beam evaporated carbon films demonstrate low adhesion to silicon-oxide surfaces, and as such, can be used to generate ultra-flat TS carbon surfaces. The detailed examination of the TS carbon surfaces, however, was left outside the scope of this research, after it was revealed that ultra-flat carbon films could be formed directly on bare, ultra-flat silicon surfaces by e-beam evaporation. In Chapter 6, the nanoscale surface smoothness of the non-pyrolyzed, amorphous carbon films was observed to be comparable to that of the TS Pt surfaces examined in Chapter 2. Pyrolysis of the films was demonstrated to induce graphitization, resulting in a poly-graphic structure to the pyrolyzed films. Associated with this new graphitic structure, was both an increase in surface roughness and electrochemical reactivity; the observed increase in electrochemical reactivity could be important for the use of ECFs in electrochemical sensing applications.[24-27]

One application of the ultra-flat e-beam deposited carbon films (ECFs), as with the TS metal surfaces discussed above, is in SPM studies of adsorbed materials on carbon surfaces. For example, pyrolytic carbon is commonly used as an artificial heart valve material,[28] however, the roughness of the material prohibits SPM studies of adsorbed proteins that may lend insight into biocompatibility issues. Although highly ordered pyrolytic graphite (HOPG) has been used as a substrate for protein adsorption studies,[29] the microstructure of HOPG is not a good model for pyrolytic carbon.

Recently, McCreery *et al.* have also demonstrated the use of carbon surfaces as electrodes in novel molecular electronic devices.[30-33] The nanoscale roughness of the ECFs demonstrated in Chapter 6, even after pyrolysis, is lower than that observed on conventionally employed PPF carbon films for their molecular electronic experiments.[34, 35] Furthermore, the patterned carbon nanowires shown at the end of Chapter 6 could potentially be used to fabricate carbon-based molecular electronic devices in a cross-bar architecture, with device densities of ~2.5 Gbits/cm^2. The application of the ECFs from Chapter 6 as electrodes in such devices is being explored by the McDermott Research Group at the University of Alberta.

References

(1) Hegner, M.; Wagner, P.; Semenza, G. *Surface Science* **1993**, *291*, 39-46.

(2) Wagner, P.; Hegner, M.; Guntherodt, H. J.; Smemnza, G. *Langmuir* **1995**, *11*, 3867-3875.

(3) Wagner, P.; Zaugg, F.; Kernen, P.; Hegner, M.; Semenza, G. *Journal of Vaccum Science & Technology B* **1996**.

(4) Wink, T.; van Zuilen, S. J.; Bult, A.; van Bennekom, W. P. *Analyst* **1997**, *122*, 43R-50R.

(5) Cornell, B. A.; Braach-Maksvytis, V. L. B.; King, L. G.; Osman, P. D. J.; Raguse, B.; Wieczorek, L.; Pace, R. J. *Nature* **1997**, *387*, 580-583.

(6) Gooding, J. J.; Hibbert, D. B. *Trends in Analystical Chemistry (TrAC)* **1999**, *18*, 525-533.

(7) Chen, J.; Reed, M. A.; Rawlett, A. M.; Tour, J. M. *Science* **1999**, *286*, 1550-1552.

(8) Wold, D. J.; Frisbie, C. D. *Journal of the American Chemical Society* **2001**, *123*, 5549-5556.

(9) Beebe, J. M.; Engelkes, V. B.; Miller, L. L.; Frisbie, C. D. *Journal of the American Chemical Society* **2002**, *124*, 11268-11269.

(10) Loo, Y.-L.; Lang, D. V.; Rogers, J. A.; Hsu, J. W. P. *Nano Letters* **2003**, *3*, 913-917.

(11) Blackstock, J. J.; Green, J. B. D.; Roseman, M.; Freeman, M. R., Segovia, Spain 2004.

(12) Blackstock, J. J.; Freeman, M. R., Banff, Alberta, Canada 2004.

(13) Blackstock, J. J.; Freeman, M. R., Edmonton, Alberta, Canada 2004.

(14) Blackstock, J. J.; University of Alberta: Report: Experiments on Molecular Monolayer of DK-I-118 on Si, 2004, pp 1-29.

(15) Hickman, J. J.; Laibinis, P. E.; Auerbach, D. I.; Zou, C.; Gardner, T. J.; Whitesides, G. M.; Wrighton, M. S. *Langmuir* **1992**, *8*, 357-359.

(16) Chen, Y.; Jung, G.-Y.; Ohlberg, D. A. A.; Li, X.; Stewart, D. R.; Jeppesen, J. O.; Nielsen, K. A.; Stoddart, J. F.; Williams, R. S. *Nanotechnology* **2003**, *14*, 462-468.

(17) Chen, Y.; Ohlberg, D. A. A.; Li, X. M.; Stewart, D. R.; Williams, R. S.; Jeppesen, J. O.; Nielsen, K. A.; Stoddart, J. F.; Olynick, D. L.; Anderson, E. *Applied Physics Letters* **2003**, *82*, 1610-1612.

(18) Stewart, D. R.; Ohlberg, D. A. A.; Beck, P. A.; Chen, Y.; Williams, R. S.; Jeppesen, J. O.; Nielsen, K. A.; Stoddart, J. F. *Nano Letters* **2004**, *4*, 133-136.

(19) Lau, C. N.; Stewart, D. R.; Williams, R. S.; Bockrath, M. W. *Nano Letters* **2004**, *4*, 569-572.

(20) Neff, H.; Henkel, S.; Hartmannsgruber, E.; Steinbeiss, E.; Michalke, W.; Steenbeck, K.; Schmidt, H. G. *Journal of Applied Physics* **1996**, *79*, 7672-7675.

(21) Street, S. C.; Xu, C.; Goodman, D. W. *Annual Review of Physical Chemistry* **1997**, *48*, 43-68.

(22) Melosh, N. A.; Boukai, A.; Diana, F.; Gerardot, B.; Badolato, A.; Petroff, P. M.; Heath, H. R. *Science* **2003**, *300*, 112-115.

(23) Al-Mawlawi, D.; Liu, C. Z.; Moskovits, M. *Journal of Materials Research* **1994**, *9*, 1014-1018.

(24) Alvarez-Icaza, M.; Bilitewski, U. *Analytical Chemistry* **1993**, *65*, 525A.

(25) Hart, J. P.; Wring, S. A. *Electroanalysis* **1994**, *6*, 617-624.

(26) Lindner, E.; Buck, R. P. *Analytical Chemistry* **2000**, *72*, 336A-345A.

(27) Wang, J.; Tian, B. M.; Nascimento, V. B.; Angnes, L. *Electrochimica Acta* **1998**, *43*, 3459-3465.

(28) Feng, L.; Andrade, J. D. *Biomaterials* **1994**, *15*, 323 - 333.

(29) Ta, T. C.; Sykes, M. T.; McDermott, M. T. *Langmuir* **1998**, *14*, 2435-2443.

(30) Ranganathan, S.; Steidel, I.; Anariba, F.; McCreery, R. L. *Nano Letters* **2001**, *1*, 491-494.

(31) Solak, A. O.; Ranganathan, S.; Itoh, T.; McCreery, R. L. *Electrochemical and Solid State Letters* **2002**, *5*, E43-E46.

(32) Anariba, F.; McCreery, R. L. *Journal of Physical Chemistry B* **2002**, *106*, 10355-10362.

(33) Solak, A. O.; Eichorst, L. R.; Clark, W. J.; McCreery, R. L. *Analytical Chemistry* **2003**, *75*, 296-305.

(34) Ranganathan, S.; McCreery, R.; Majji, S. M.; Madou, M. *Journal of the Electrochemical Society* **2000**, *147*, 277-282.

(35) Ranganathan, S.; McCreery, R. L. *Analytical Chemistry* **2001**, *73*, 893-900.